UNIVERSITEIT VAN PRETORIA
UNIVERSITY OF PRETORIA
YUNIBESITHI YA PRETORIA

Fakulteit Ingenieurswese, Bou-omgewing & IT
Faculty of Engineering, Built Environment & IT

Department of Materials Science and Metallurgical Engineering

Module code: NIN 890

PERFORMANCE AND HYDRODYNAMIC CHARACTERISATION OF LABORATORY BATCH FLOTATION CELLS

by

Mfesane Tshazi

Supervisors: Prof. N. Naudé & Prof. L.S. Leal Filho

March 2024

Dissertation submitted in partial fulfilment of the requirements for the degree Master of Engineering in Metallurgical Engineering.

UNIVERSITEIT VAN PRETORIA
UNIVERSITY OF PRETORIA
YUNIBESITHI YA PRETORIA

Denkleiers • Leading Minds • Dikgopolo tša Dihlalefi

Abstract

The purpose of this study was to compare the Denver and Leeds laboratory flotation cells by evaluating their performance in the flotation of quartz of four sizes (−25 µm, +25–45 µm, +45–75 µm, and +75–106 µm). This study was conducted at the Materials Science and Metallurgical Engineering laboratory of the University of Pretoria.

The impeller diameters of the Denver and Leeds cells were measured to be 0.07 m and 0.074 m, respectively. The impeller speeds of the cells were calibrated for identical flotation performance (assessed using quartz recoveries without interfering with the cell design), with the Denver cell set at 1200 rpm and the Leeds cell at 1400 rpm. The reagent regime was kept constant, using 25 g/t Flotigam EDA ether amine as a collector, no frother, and NaOH to modify the pH to 9.5. The air flow rate was kept constant at 2 L/min in each of the 3.5 L cells. Flotation kinetics tests were conducted at the optimal rotation speeds, and the results were similar. Both cells achieved similar quartz recoveries of over 70 % for the three +25 µm fractions, but only 15 % for the −25 µm fraction. An additional collector was required to improve the recovery of the −25 µm fraction significantly. These findings demonstrated the effect of particle size on flotation recovery, and the finer particles requiring more reagent due to their larger surface areas.

The performance of these cells was further evaluated using dimensionless numbers and with a chemical tracer. The use of dimensionless numbers, such as Power and Reynolds numbers, allowed for a detailed analysis of the cells' hydrodynamics. Additionally, a chemical tracer (NaOH), was used to assess the mixing efficiency of the impellers.

The Denver flotation cell exhibited superior performance compared to the Leeds cell. It managed to achieve higher recovery rates while consuming less power. This can be attributed to the effective design of its impeller and stator, which enabled it to overcome the resistance posed by the slurry, allowing it to operate at optimal levels that surpassed the capabilities of the Leeds cells.

The performance of the Leeds cell was found to be inferior to that of the Denver cell, and this is attributed to several factors. One of the main reasons is the slightly larger bubble size of 3.5 mm in the Leeds cell, compared to the Denver cell's average of 2.5 mm. Therefore, the surface area available for particle attachment was still low for the Leeds cell, even at higher impeller speeds. Additionally, the power numbers for the Leeds cell were higher, averaging at 1.03 between 1000

and 1500 rpm in the presence of solids, while the Denver cell averaged 0.77 under the same conditions. This indicates that the Leeds cell requires more power to create the necessary flow. All this leads to deterioration in particle collection efficiency and an overall reduction in performance.

Keywords: quartz, flotation, Denver cell, Leeds cell, particle size, flotation kinetics, impeller speed, recovery, hydrodynamics

Plagiarism declaration

Full names	Mfesane Phaphama Tshazi
Student number	25358911
Topic of work	Master's degree thesis – Performance and hydrodynamic characterisation of laboratory batch flotation cells.

Declaration

1. I understand what plagiarism is and am aware of the University's policy in this regard.
2. I declare that this thesis is my own original work. Where other people's work has been used (either from a printed source, internet or any other source), this has been properly acknowledged and referenced in accordance with the requirements as stated in the University's plagiarism prevention policy.
3. I have not used another student's past written work to hand in as my own.
4. I have not allowed and will not allow anyone to copy my work with the intention of passing it off as his or her own work.

Signature: 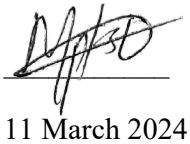

11 March 2024

Acknowledgements

I would like to thank and appreciate God, without Whom this work would not have been possible He has been my Rock, Support, and Source throughout. All glory is His.

I am grateful to my supervisors, Prof. Natasia Naudé and Prof. Laurindo de Salles Leal Filho, for their support and guidance throughout my studies. Their wisdom, guidance, and patience have been invaluable to me as to overcome challenges, difficulties, and delays. Thank you for the constructive criticism and feedback, which enabled me to continue striving for excellence.

My sincerest gratitude goes to Anglo American, for the financial aid in my studies and to Mr. Johan van Rooyen, for guidance and technical support.

I am truly grateful to the Department of Materials Science and Metallurgical Engineering, for the use of the facilities. Furthermore, I extend my heartfelt thanks to all the staff and colleagues in the department for their invaluable contributions. Every great or small effort was noticed and greatly appreciated.

A special thank you to Prof. Kathryn C. Sole for her technical and English language editing of this dissertation.

A special thanks to my whole family, especially my wife Verna Tshazi and our wonderful children Zechariah and Tirzah. Their love, patience, and support have carried me through. They have been a pillar of strength to me.

Finally, thank you to everyone who contributed to the success of this project.

Table of Contents

List of Figures

List of Tables

Nomenclature

Symbols

A	cell cross-sectional area (m^2).
a, i, β, α, ∂, f, h, y	exponents
c	distance between the impeller centre and the bottom of the tank (m)
C_D	drag coefficient
D	impeller diameter (m)
D_b	Sauter mean bubble size (m)
d_b	bubble diameter (m)
d_p	particle diameter (m)
E_c , E_a , *and* E_p	efficiency of particle–bubble collision, of adhesion, of preservation of the particle–bubble aggregate, respectively
g_a	acceleration due to gravity (m/s^2)
J_g	superficial gas velocity (m/s)
k	flotation rate constant (s^{-1});
k_c	collection zone flotation rate constant
K_g	parameter related to the impeller's ability to suspend solids under aerated conditions (s/m);
K_{sl}	parameter related to the impeller's ability to suspend particles in the absence of air (dimensionless)
L	litre
[M], [L], and [T]	symbols representing mass, length, and time
N	impeller rotational speed (s^{-1})
N_{Eu}	Euler number
N_{Fr}	Froude number
N_G	air flux number
N_{js}	impeller critical rotation (s^{-1})
N_P	Power number
N_Q	pumping or flow number
N_{Re}	Reynolds number
N_{We}	Weber number
P_c	capillary pressure (kPa);
P_f	parameter that represents the floatability of an ore
P	power drawn by impeller (W)
Q_{CIRC}	total circulating fluid flow rate (m^3/s).
Q_d	flow rate discharged by the impeller (m^3/s).

Q_g	air flow rate feeding cell (m^3/s)
R	cumulative recovery at time t (%)
R_f	froth recovery factor.
R_{max}	maximum recovery, which is approximately asymptotic as $t \to \infty$ (%)
S	geometric factor related to impeller shape and position in the tank
S_b	bubble surface area flux (m^2/m^2s)
t	flotation time (s)
T	tank diameter (m)
t_{circ} and t_{mix}	mean circulation time (s)
U	radial fluid velocity (m/s)
U_s	terminal settling velocity (m/s)
V	voltage of the signal output (V)
V_{eff}	effective volume (volume of slurry − volume of air) (m^3)
V_f	fluid volume slurry or water) filling the flotation tank (m^3)
W	impeller blade width (m)
X	percentage mass proportion of solids to liquid, (dimensionless)
Z	height of the slurry level in the cell (m)

Greek symbols

Δp	pressure difference promoted by movement of impeller blades (Pa)
ε	mean energy dissipation (W/kg)
ε_g	fractional volume occupied by air in the flotation tank
$[\eta]$	intrinsic viscosity
ϑ	equilibrium contact angle (°)
φ	volume fraction of the dispersed solid
φ_m	maximum packing fraction
p	local pressure (kPa)
ρ_l and ρ_s	specific gravity of the liquid and solid (kg/m^3) respectively
τ_{shear}	shear stress (N/m^2)
μ (μ_l and μ_0)	slurry dynamic viscosity at a given temperature (Pa s).
v, (v_w and v_l)	kinematic viscosities of pure water and a liquid (m^2/s) respectively
$\gamma_{l/g}$	surface tension of the flotation solution (N/m).
γ_{sg}, $\gamma_{sl,}$ and γ_{lg}	solid–gas, solid–liquid, and liquid–gas interfacial tensions (N/m) respectively

Chapter 1: Introduction

1.1 Background

Batch flotation tests have made considerable contributions to industrial process development and troubleshooting (Newcombe *et al*., 2012; Ross, 2019). Findings from these tests, coupled with appropriate scale-up factors, are used by engineers to design flotation equipment and construct process flowsheets.

One major limitation of batch testing is that correlations between data gathered during these experiments and those obtained from actual plant operations have historically been poor (Newcombe *et al*., 2012). This discrepancy can be largely attributed to differences in equipment configurations between laboratory setups and full-scale plants, such as impeller design, as well as operational parameters. Despite these issues, research continues to investigate ways in which batch test results may more accurately predict real-life outcomes, while accounting for factors such as particle size distributions or reagent concentrations (Chen & Peng 2015; Newcombe *et al*., 2012). Therefore, correlations between laboratory-scale experiments and plant-scale implementations can become more reliable, thereby providing greater confidence when scaling up new processes or troubleshooting existing processes within an industrial setting.

It is important to remark that mining chemical suppliers usually develop new collectors, frothers, and modifying agents by conducting extensive laboratory campaigns: new reagents that are approved at batch scale are more easily accepted for use in industrial circuits. This fact indicates that chemical variables exert less influence on discrepancies between flotation performance in the laboratory compared with industry, whereas hydrodynamics play a major role.

The development of froth flotation has been greatly aided by use of batch mechanical cells in laboratory settings. Knowledge and understanding of a cell's hydrodynamics can provide insight into how impeller design affects process performance, as well as determine which conditions are best suited for a particular cell. Therefore, comparing the performances of different laboratory cells under equal reagent dosages and operating conditions (e.g. water quality, pH, gas holdup, and flotation time) may provide insight into cell behaviour at larger scales. This dissertation is an attempt to contribute towards understanding the reasons why two

impellers of different designs (Denver and Leeds) exhibit different performances in the cationic flotation of quartz in a basic medium.

1.2 Froth flotation

The froth flotation technique, established in 1906, has revolutionised the metallurgical industry over the past 120 years. This process was introduced to treat fine minerals that are below the particle size limit of gravitation beneficiation processes (Fuerstenau, 1962). The froth flotation process was initially developed for the beneficiation of the sulfide minerals (Fuerstenau *et al*., 2007; Wills and Finch, 2015). Froth flotation is an important metallurgical operation that allows for the separation of valuable minerals from gangue species by making use of physical and chemical surface properties. Research and modifications have enabled its applicable to other mineral types, ranging from simple materials (coal) to low-grade complex ores (Wills and Finch, 2015). Additionally, non-metallurgical applications, such as water treatment processes, have also benefitted from flotation techniques (Kyzas and Matis, 2018).

The process is affected by the characteristics of the flotation machine used. These machines are divided into two categories: mechanical and pneumatic flotation cells (Fuerstenau *et al*., 2007; Kelly and Spottiswood, 1982). Mechanical flotation cell designs, which have been in use since inception of this technology, are still widely accepted throughout the mineral processing industry. The primary difference between these two types of machines is the manner in which air is employed: mechanical flotation cells include an impeller that is responsible for both bulk fluid flow and turbulent fluid motion of the air and slurry; pneumatic flotation cells do not have an impeller but rely on an air sparge to suspend and circulate the slurry, as well as collect hydrophobic minerals to the froth zone. Pneumatic cell technology was introduced in the 1960s, with later sub-division into column-type and high-intensity models (Fuerstenau *et al*., 2007). Pneumatic models are generally employed for more specific applications than traditional mechanical designs can offer, due to unique properties that allow them to be better tailored to the needs of a particular application (Kelly and Spottiswood, 1982).

Many of the crucial fundamental parameters of froth flotation are determined from laboratory tests conducted using laboratory flotation machines. Laboratory flotation tests provide quick snapshots of performance that can be expected at a pilot scale, and further at the industrial scale,

based on a small sample (approximately 2 kg of ore) (Runge and Wills, 2015). Bench-scale experiments and ongoing research are used to collect useful data that help to better understand the many factors that influence a froth flotation process. Testing in a laboratory therefore forms an integral part of designing froth flotation processes and improving operational performance and efficiency.

1.3 Flotation as a beneficiation process

The flotation process relies on prior unit operations, such as comminution, to achieve adequate liberation of valuable minerals from gangue and obtain an appropriate size range, which is used to control the particle size distribution of the material that feeds the flotation process. The concentrated valuable minerals from flotation are subjected to downstream extraction steps, such as dewatering (thickening, filtering, drying), followed by pyrometallurgical and/or hydrometallurgical processing. The effectiveness of the flotation step heavily depends on three main factors: chemistry, hydrodynamics, and operational conditions.

Chemistry plays a significant role in froth flotation because flotation reagents adsorb onto the air–solution and mineral–solution interfaces, and thereby modify the surface properties of particles and bubbles. Hydrodynamics must also be considered when designing a successful flotation system. This comprises air and slurry flows, particle suspension, bubble dispersion, and energy dissipation or turbulence intensity, which can affect particle behaviour, depending on particle size distributions within the flotation cell. Operational variables, such as mineralogy, particle size, and pulp density, must be optimised to ensure maximum recoveries.

Froth flotation has been described by Wills and Finch (2015) as an adaptable process because it can be applied to a wide range of minerals. Although most minerals are hydrophilic (Kelly and Spottiswood, 1989), this process is a predominant method for mineral concentration. The minerals desired to be floated need to be rendered hydrophobic for concentration purposes. This process generally relies on the use of chemicals to ensure selective separation between the gangue and valuable minerals. Numerous mineral industries report overall flotation recoveries of approximately 80%–90% (Hassanzadeh *et al*., 2021).

1.4 Concentration techniques

Selection of an appropriate technique for concentration of an ore to achieve adequate mineral separation depends on several factors. These include, among others, ore properties, such as size, liberation, shape, specific gravity, and colour (Vianna *et al*., 2003). Additionally, electrical properties, magnetism, radioactivity, surface composition, and texture should be taken into consideration. Considering all these criteria, it is possible to maximise recovery of the target mineral(s).

Figure 1 shows the application range of froth flotation compared with other concentration techniques. Froth flotation can be applied to particle diameters from 1 µm to 700 µm: the preferred range is between 10 and 150 µm (Lima *et al*., 2018). Actual optimal ranges vary based on mineral composition (Trahar, 1981).

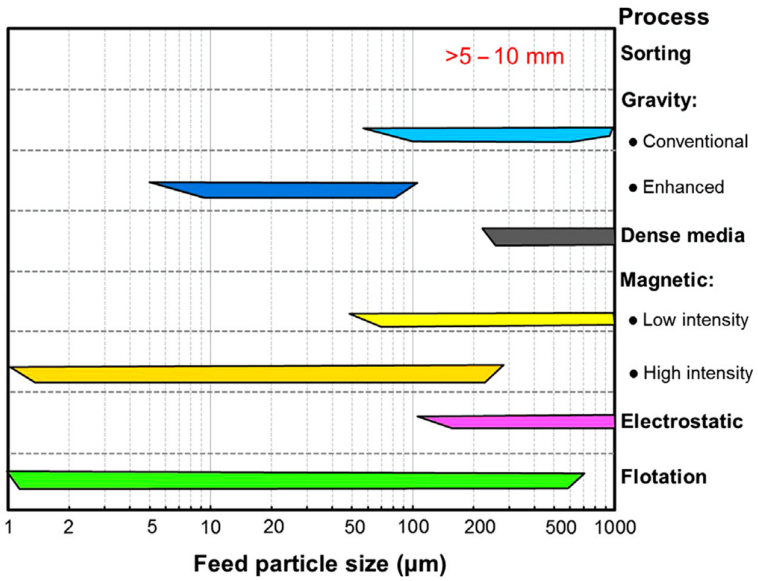

Figure 1: Effective range of application of selected mineral separation techniques as a function of feed particle size (from Wills and Finch, 2015).

1.5 Batch flotation process

Figure 2 illustrates a flotation process. The process involves cells filled with slurry (solids and water), which is mixed and suspended by an impeller. In a typical mechanical laboratory cell,

the (hollow) impeller shaft pipe acts as a channel to transport air into the cell. As air reaches the rotating impeller, it is sheared into small bubbles. Appropriate reagent(s) suites (collector, frother, depressant, modifier) are added to the pulp. Frother is a reagent that promotes the creation of bubbles to support the motion of the impeller.

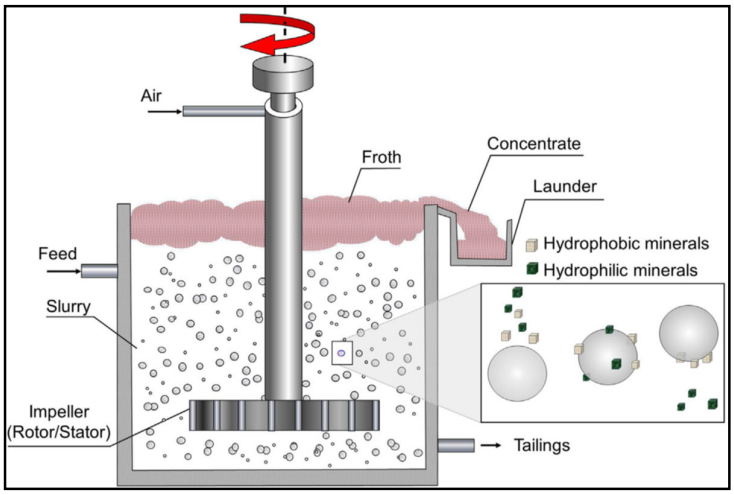

Figure 2: Illustration of the flotation process (from Wills and Finch, 2015).

The air bubbles collide with particles in the pulp and become attached to the hydrophobic mineral particles; other minerals tend to remain in the pulp. Stable aggregates of a bubble and hydrophobic mineral move upwards into the froth layer due to buoyancy forces, where they are removed into the concentrate tray. The concentrates are generally removed at regular intervals to evaluate the process kinetics. Hydrophilic minerals remaining in the pulp are removed as tailings.

Minerals can be selectively separated by direct or indirect flotation: direct flotation is the process of recovering the valuable minerals to the concentrate; indirect flotation rejects the valuable minerals to the tailing stream. However, gangue minerals can be deported to the concentrate as a consequence of the undesired phenomena of entrainment and entrapment.

1.6 Flotation mechanisms

Fuerstenau *et al*. (2007) stated that the total recovery obtainable in the froth flotation process is attributed to two main mechanisms, i.e., true flotation and entrainment. Wang *et al.* (2015) and Wills and Finch (2015) indicated a third mechanism of entrapment that is perhaps less dominant.

True flotation is governed by three mechanisms involving the mineral particle and air bubble: collision, attachment, and detachment. A brief description of true flotation is that a hydrophobic particle needs to collide with an air bubble, the two entities become attached, and then this unit must remain stable as it moves through the cell and into the froth zone until it is discharged via the cell lip. This is a chemically activated process (Wills and Finch, 2015). In general, true flotation accounts for most particles concentrated by froth flotation due to the selectivity enhancement process (Wills and Finch, 2015). True flotation only accounts for the recovery of valuable minerals.

Entrainment results from water-suspended minerals deporting to the concentrate launder (Wang, 2016). The entrainment mechanism is non-selective because the particles are not attached to an air bubble. This mechanism can concentrate both valuable and gangue mineral particles. Wang *et al.* (2015) and Zheng *et al*. (2006) noted that recovery by entrainment generally favours particle sizes below 50 µm.

The entrapment mechanism is associated with a non-draining froth phase, particularly for coarse minerals (Zheng *et al*., 2006). Mineral particles become trapped between air bubbles. This mechanism primarily affects coarse particles (> 106 µm) more than fine particles (Zheng *et al*., 2006). Valuable and gangue minerals can be concentrated by entrapment, similar to the entrainment mechanism.

All three mechanisms will likely simultaneously proceed during a flotation process. In addition to true flotation, recovery of valuable minerals by the non-selective mechanisms (entrainment and entrapment) plays a critical and significant role in the overall recovery. Entrainment and entrapment of gangue (hydrophilic minerals) are undesirable, because these negatively affect recovery, grade, and froth stability (Wills and Finch, 2015). Although various research projects have focussed on understanding the entrainment mechanism (Wang *et al.*, 2015), the same cannot be said for the entrapment mechanism.

1.7 Hydrophobicity

Hydrophobicity, as described by Fuerstenau *et al*. (2007), refers to the polarity of the mineral surface. Hydrophobicity (natural or induced) relates to a non-wettable mineral surface: a hydrophilic mineral surface is wettable. The separation that is achieved by froth flotation relies on these differences. Hydrophobicity quantifies the degree to which a surface can repel water and is measured by and is proportional to the contact angle (Fuerstenau *et al*., 2007; Gupta and Yan, 2016; Wills and Finch, 2015). The contact angle is measured at the junction between the three phases: solid, gas, and liquid, as simplified in Figure 3. The contact angle ranges between 0° and 180°, these extremes representing superhydrophilic and superhydrophobic materials, respectively. The closer the contact angle is to the upper limit of this range, the greater is the bubble–particle stability (Nuraje *et al.*, 2013).

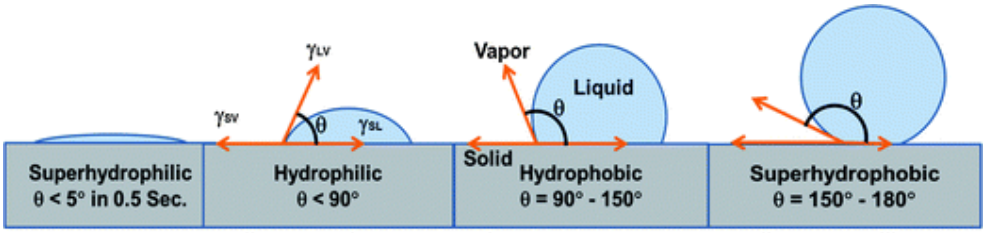

Figure 3: Illustration of contact angle at different degrees of hydrophobicity (from Nuraje *et al.*, 2013).

Interfacial tensions between the phases are best expressed by Young's equation, as given by Equation (1) (Drzymała and Swatek, 2007), where liquid (l), solid (s), and air saturated with vapour (g) are in equilibrium:

$$\gamma_{sg} = \gamma_{sl} + \gamma_{lg} \cos\vartheta, \quad (1)$$

where γ_{sg}, $\gamma_{sl,}$ and γ_{lg} are the solid-gas, solid-liquid, and liquid-gas interfacial tensions (mN/m or mJ/m^2), respectively, and ϑ is the equilibrium contact angle (°).

Drzymala and Lekki (1989) reported contact angles based on flotometric measurements for several materials. A list of representative materials is given in Appendix A. The measurements

showed that the contact angle of quartz was zero, which represents a typical hydrophilic mineral. Mineral surfaces can be modified using reagents to achieve a particular separation outcome (Wills and Finch, 2015).

1.8 Flotation system

Froth flotation is generally described as a complex process with many influencing factors and interdependent interactions, as shown in Figure 4. A change in a single variable typically has an impact on other variables. Arbiter and Harris (1962) noted that there could be as many as one hundred interdependent variables. These variables can be grouped into three component systems, as shown in Figure 4.

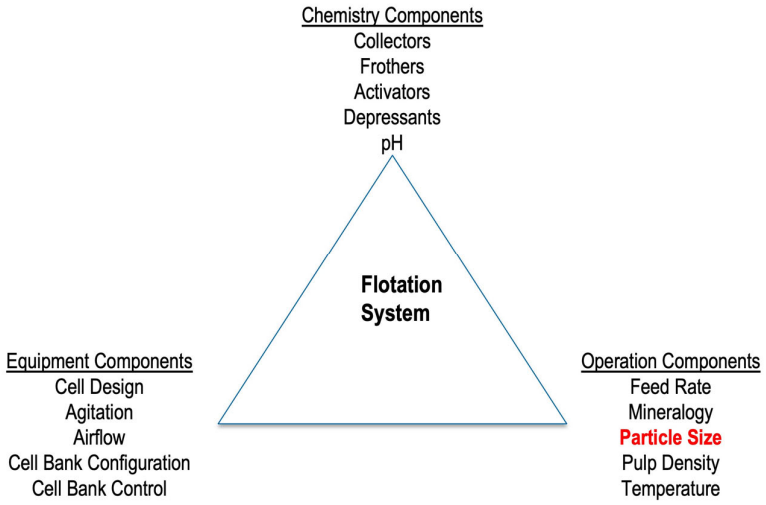

Figure 4: Various factors influencing a flotation system (Klimpel, 1984).

This study focused on particle size and agitation as the primary variables, while other variables were kept constant. The intention was to limit complexity and avoid bias during interpretation. Moreover, a non-conventional route was chosen, in that a single mineral, quartz, was used for the test work comparison.

1.9 Batch froth flotation equipment

Figure 5(a) illustrates a Denver D-12 laboratory flotation cell. This design is over 70 years old and is the most widely used cell for conducting laboratory test work, despite the current availability of more advanced laboratory cells (Amelunxen *et al.*, 2018). Industry standards have been established using the laboratory Denver flotation cell to standardise test conditions and ensure prevention of scale-up bias (Amelunxen *et al.*, 2018). Figure 5(b) illustrates a Leeds laboratory flotation cell. As introduced by Professor C. Dell of the University of Leeds, this cell design aimed to improve reproducibility of results and reduce operator-dependent factors (Liddell and Dunne, 1983). Flotation tests performed in laboratories usually depend on the operator because froth scraping is generally done manually. The scraping areas of the cells differ: the Denver cell has an impeller in the centre, which obstructs scraping, while the Leeds has no obstruction. The Leeds cell features a froth crowder-like shape at the rear, rendering the area behind the impeller inaccessible. The Leeds cell is designed as a complete unit and parts are not easily interchangeable, whereas the Denver cell allows for more flexibility because the cell size and impeller design can be easily changed.

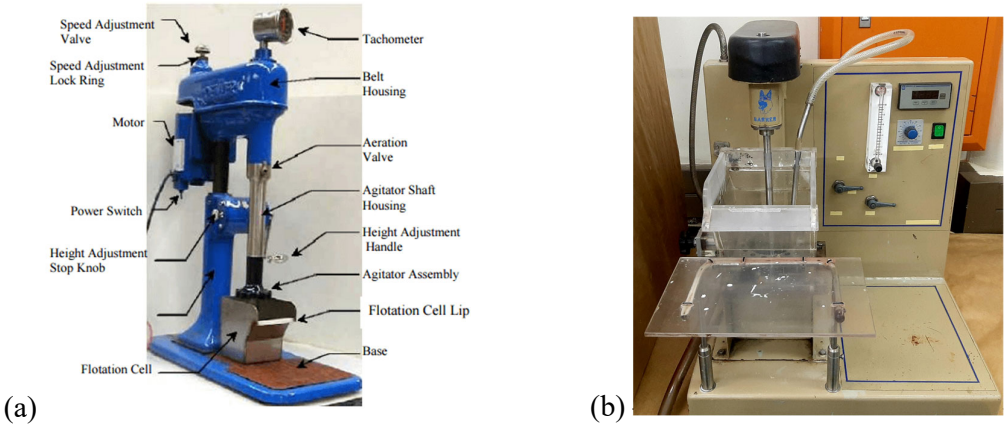

Figure 5: Photographs of (a) Denver (Yahorava *et al*., 2009) and (b) Leeds laboratory cells at the University of Pretoria.

One of the most significant differences between the two cells is their impeller design, as illustrated in Figure 6. The centrally positioned Denver impeller shaft (Figure 6(a)) also serves as a channel for transporting induced air. This design has four equally sized holes on the stator,

from which the sheared air is introduced into the cell in approximately equally sized bubbles. In the Leeds cell, the air inlet is not central, as shown in Figure 6(b), and air is introduced just above the impeller to be sheared. Consequently, some air is forced into the impeller and sheared into smaller equally sized bubbles and some air bypasses the impeller to enter the cell. As a result, the bubbles within the cell are of different sizes.

(a) 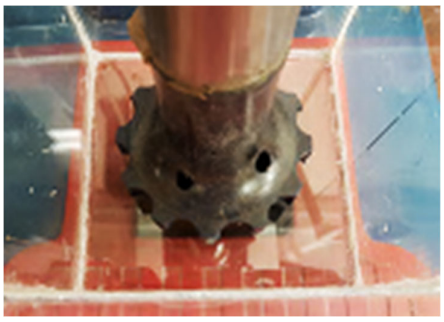 (b) 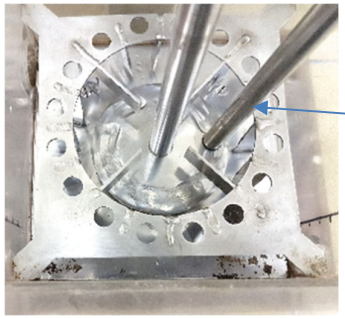

Figure 6: (a) Denver and (b) Leeds impeller designs.

1.10 Scope of the study

The role of laboratory batch flotation cells in the flotation process is crucial, as they aid in its development and characterisation. These cells are essential tools for understanding the behaviour of different minerals and their response to various flotation conditions. In industry, there are various laboratory cells available, and it is important to determine whether their performance is comparable.

In this study, the performance of two laboratory mechanical cells (the Denver and Leeds) was evaluated through kinetic testing using quartz as a single mineral. This deliberate choice of a single mineral ensured that any observed variations in flotation performance could be attributed to the differences in impeller design, which significantly affects the hydrodynamics and flotation behaviour of both coarse and fine particles.

The testing conditions were carefully optimised and refined by calibrating the impeller's rotational speeds. This was done to ensure that the cells were operating at the same level of performance. With the optimised conditions in place, the focus shifted to comparing the effect of particle size and assessing the hydrodynamic conditions of these cells.

The test conditions were carefully controlled, with constant variables such as chemical dosage, operational parameters, and system conditions. These variables were kept at a consistent level throughout the testing process, with 25 g/t of Flotigam EDA ether amine collector in a basic medium at pH 9.5, 2 L/min gas flow rate, and 17 mass% solids concentration.

The findings from this investigation will contribute to the understanding and the identification of the most efficient settings and conditions for these cells and similar cells.

1.11 Aim and objectives

The objective of this comparative testwork was to evaluate the performance of two 3.5 L laboratory flotation cells (Denver and Leeds cells at the University of Pretoria) under identical experimental conditions. This study aims to identify the superior cell and the key parameters that are most influential in its performance.

The first phase of the study entailed examining the effect of particle size, with a particular emphasis on optimising the flotation response of quartz. Tests were deliberately confined to a single mineral so that results could be more accurately compared. Tests using narrower size ranges were conducted at optimal conditions to obtain more detailed data concerning how changing particle size affected the respective overall performance of each cell.

The second phase of the study involved analysing hydrodynamic parameters, such as air flow rate and impeller speed, during operation to understand the contributions of these parameters with respect to achieving optimum performance. These results were used to explain the results obtained for varying particle sizes. This study will enhance understanding and operating of these cells, as well as to identify the most efficient cell type under laboratory conditions.

1.12 Hypothesis

The efficiency/recovery of minerals by flotation depends on the type of laboratory flotation cell used.

1.13 Thesis structure

This thesis has six chapters, excluding the reference list and appendices. The outline is as follows.

Chapter 1: Introduction introduces the topic and gives some history and a brief background of froth flotation, including the objectives of this thesis.

Chapter 2: Literature review reviews the literature on flotation and its principles are discussed with particular reference to particle size effects and hydrodynamic parameters.

Chapter 3: Methodology describes the methods and measures used for sample preparation, flotation kinetics tests, and hydrodynamic characterisation.

Chapter 4: Results and Discussion presents the results obtained from the various test programmes and provides an interpretation of the effect of particle size and hydrodynamic characterisation.

Chapter 5: Conclusion summarises the study findings and presents the outcomes.

Chapter 6: Recommendations describes future work that can build on the findings of this study.

Chapter 2: Literature review

2.1 Particle size

According to Trahar and Warren (1976), the typical flotation size range is 15 to 150 µm, while Jowett (1980) reported that the range was slightly narrower at 20 to 120 µm. In addition to the influencing factors listed in Figure 4, the effect of particle size on flotation recovery is highlighted in Figure 7, where the size ranges can be considered in three categories: fines, intermediate particles, and coarse particles. Optimum recoveries, typically approaching 100%, are generally obtained in the intermediate particle size range. Consequently, particles outside of a particular range will be compromised when floated, and achieving optimum recoveries is difficult. This can be attributed to poor collision and attachment efficiencies of fine particles and high detachment efficiencies of coarse particles (Nguyen, 2007). Narrow-size operations are ideal and should be applied whenever possible (Pease *et al*., 2006). Both fine and coarse materials can be optimally floated only if the kinetics associated with each size fraction are fully understood and controlled.

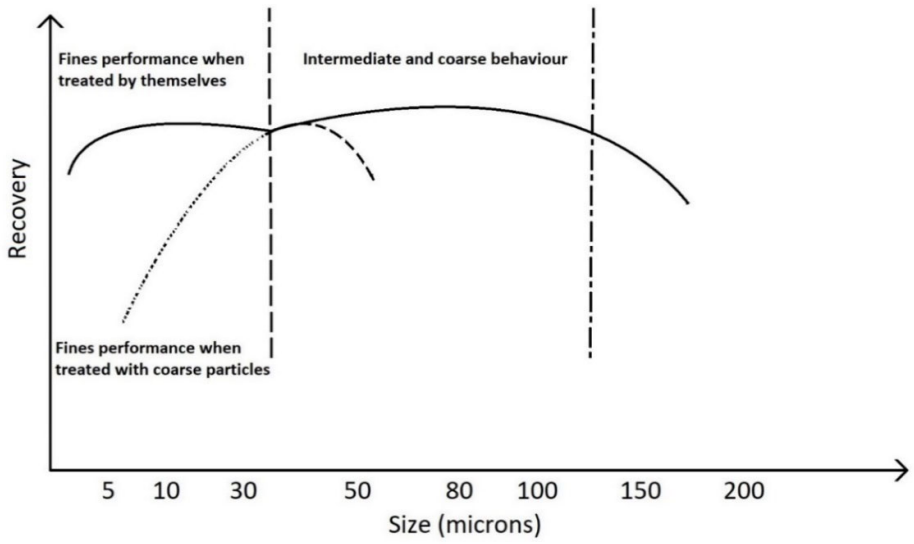

Figure 7: Effect of particle size on flotation recovery, as modified from Pease *et al*. (2010).

Fine particles suffer from poor collision efficiency, thus resulting in poor overall recovery (El-Rahiem, 2014; Nguyen, 2007). The main factors affecting collision efficiency are bubble size,

energy input, and pulp rheology. Nevertheless, recovery of this fraction can be fine-tuned by adjusting any of these factors. Furthermore, owing to the larger surface area of fine particles, higher reagent dosages are often required to render them hydrophobic (Pease *et al*., 2006). In contrast, coarse particle flotation is reduced by detachment of particles from bubbles (Wills and Finch, 2015). The main factors affecting detachment are hydrophobicity and energy input (or agitation). Coarse particle recovery can be optimised by focusing on these two parameters. It should be noted that fine and coarse particle recoveries often react in an opposing manner (Safari *et al*., 2016): for instance, increasing energy input will benefit fine particle recovery, but decrease coarse particle recovery because of increased particle-bubble detachment. Careful consideration should be used when optimising recovery of a certain size fraction to avoid unintentional detrimental effects.

2.1.1 Fine particle flotation

The particle size fraction below 20 µm is often regarded as fines, or even ultrafines (Hassanzadeh *et al*., 2021; Miettinen *et al*., 2010). This fraction has attracted much attention owing to its high degree of liberation, which is necessary for flotation. However, there are complications that make recovery of this fraction challenging, such as poor collision efficiency (Ross *et al*., 2019). According to Bulatovic *et al*. (1998), a typical operating plant experiences approximately 50% of its losses in the −20 µm range. With a decrease in particle size, the mass correspondingly decreases while the surface area increases (El-Rahiem, 2014); however, particle aggregation (colloquially known as ‘piggy-back’ flotation) can enhance recovery of this fraction (Rahman Ata & Jameson, 2012). Aggregates are formed when fine particles attach to larger particles. Aggregation can enhance flotation performance and recovery of fine particles.

Recovery by entrainment is largely dominant in the fines fractions, as evidenced by Pease *et al*. (2006). According to El-Rahiem (2014), this non-selective process reduces the concentrate grade due to concentration of both valuable and gangue minerals. Fine particles require extended flotation times for optimum recoveries. Chander (1978) summarised the behaviour of fine particles using the flow diagram shown in Figure 8. As the particle size reduces, two characteristics become increasingly common: an increase in specific surface area and a decrease

in mass. The decrease in mass lowers particle momentum and collision probability. These factors enhance entrainment and entrapment recovery. The large surface area of fine particles leads to higher reagent adsorption capacity, increased slimes content in the reaction vessel, and a higher probability of oxidation because more surface is exposed for reactions with external agents, such as oxygen or other chemicals present in the environment. The above combination of factors leads to reduced recovery (Chander, 1978; Pease *et al*., 2006).

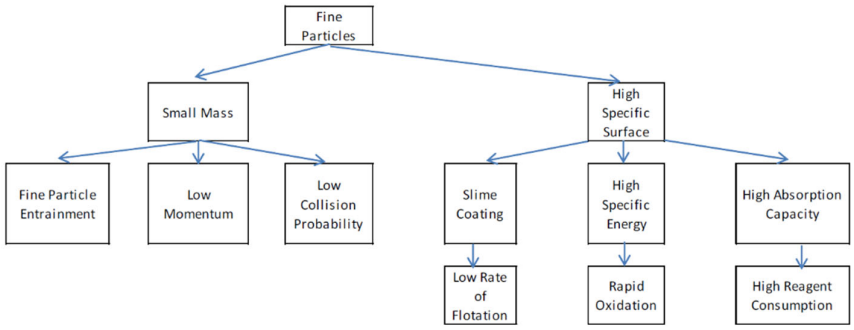

Figure 8: Flotation characteristics of fine particles (from Chander, 1978).

2.1.2 Coarse particles

Coarse particles are typically regarded as larger than 150 µm, with the exception of minerals like coal, which can be floated up to 500 µm (Bu *et al*., 2016). This particle size lies outside the typical flotation range of 20 to 150 µm (Hassanzadeh et al., 2021; Norori-McCormac *et al*., 2017; Shergold, 1984). These particles are likely to be composite in mineral composition and therefore may only have been liberated to a limited degree, which results in poor recovery (Pease *et al*., 2006). Coarse particles generally have high probability of colliding with an air bubble to form a bubble–particle aggregate; however, such aggregates are more prone to detachment, which increases with the increase in particle size (Tao, 2005). Adhesive forces between the particle and bubble weaken (Tao, 2005) as the aggregate ascends to the froth phase due to the considerable particle mass and occurrence of detachment; mineral recovery of coarse particles is consequently poor. However, according to Rahman *et al*. (2012), coarse particles can be more effectively recovered when fine particles are present. Fine particles play a role in

stabilising the froth and inhibiting bubble coalescence, which improves the recovery of coarse particles.

2.1.3 Effect of impeller

The hydrodynamic conditions within a flotation cell are essential for effective solid suspension, gas dispersion, reagent mixing, particle–bubble interaction, and water recovery in the froth. The size of the particles affects how well they suspend and disperse during fluid circulation and turbulence caused by rotating impellers (Deglon, 2005; Lima *et al*., 2009; Raghava Rao *et al*., 1988). The concept of critical impeller speed, introduced by Zwietering (1958), can be used to assess the status of a solid suspension. The critical impeller speed, also known as the just off-bottom suspension or 1-s criterion, is the minimum impeller speed at which all solids are suspended from the tank's bottom (Lima *et al*., 2009). To ensure optimal recovery of fines, an impeller speed that exceeds the minimum suspension speed (the so-called '1 s criterion') should be employed, while coarse particles are most effectively recovered at minimum suspension speed (Nguyen, 2007).

Deglon (2005) found that increasing impeller speed in a mechanical cell can lead to improved recovery, because high turbulence leads to increased particle–bubble collisions. However, high turbulence also increases the rate of particle–bubble detachment (Deglon, 2005; Rodrigues *et al*., 2001; Tao, 2005). Thus, when considering impeller speed increments for flotation processes, it is essential to take into consideration both positive and negative impacts on recovery.

2.2 Dimensionless characterisation

In froth flotation, the term hydrodynamics pertains to how fluid flows within the flotation system. This is primarily influenced by the performance of the impeller (Shabalala *et al.*, 2011; Souza Pinto *et al.,* 2018). In order to understand and analyse the hydrodynamics of flotation, it is common to use hydrodynamic parameters and dimensionless numbers (Souza Pinto *et al.,* 2018). These parameters and numbers take into consideration the complex interactions and

behaviours, which include mechanical characteristics, pulp properties, gas dispersion, solution chemistry, and cell design (Wang and Liu, 2021).

2.2.1 Hydrodynamics of flotation impellers

A mechanical flotation cell can be considered a turbomachine, much like a centrifugal pump or stirred chemical reactor. It operates under the action of a rotating impeller that continuously converts torque energy into fluid flow by two different mechanisms: bulk fluid flow (BFF) and turbulent fluid motion (TFM). Therefore, to characterize the hydrodynamics of an impeller, one must account for how it promotes flow as it rotates within a tank filled with water or slurry.

2.2.2 Bulk fluid flow and its influence on impeller performance

Bulk fluid flow (BFF) is responsible for slurry circulation within a tank and may be represented by streamlines that can be observed on addition of optical tracers. In a flotation cell, an impeller continually moves slurry from the bottom of the stirred tank to the upper section. The impeller can be considered as caseless (or partly open case) centrifugal pump, as depicted in Figure 9 (Lima *et al*., 2009).

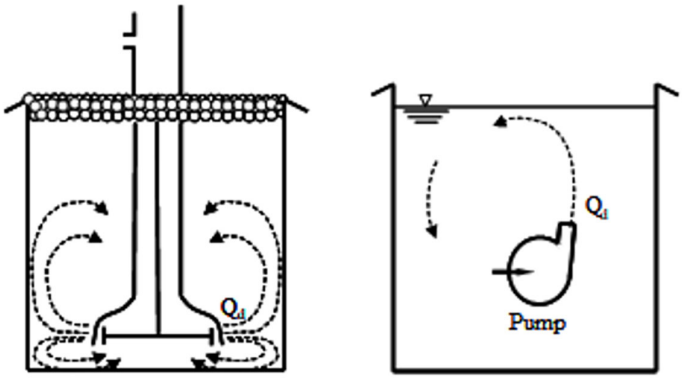

Figure 9: Slurry circulation in a flotation machine: analogy between an impeller and a pump (Lima *et al*., 2009).

The volumetric quantity of fluid discharged by an impeller per unit of time is known as the discharge flow rate (Q_d). This depends upon the radial fluid velocity (U) at the impeller discharge (Holmes *et al*., 1964). The impeller discharge flow rate (Q_d) may be used to describe either its ability to pump fluids or its ability to circulate fluids within a tank (Edwards and Baker, 1992; Oldshue *et al*., 1995). The fluid velocity (U) promoted by the movement of an impeller is a function of the flow regime (laminar or turbulent), rotational speed (N), and the impeller's design diameter (D) (Bertrand *et al*., 1980).

Figure 10 depicts the influence of impeller rotational speed (N) on the fluid flow rate (Q_d) generated by a Denver impeller operating in a laboratory mechanical flotation cell with tap water. The higher the value of N, the higher is the magnitude of Q_d, promoted by the impeller movement. In this case, the impeller acted as a centrifugal pump within the stirred flotation tank.

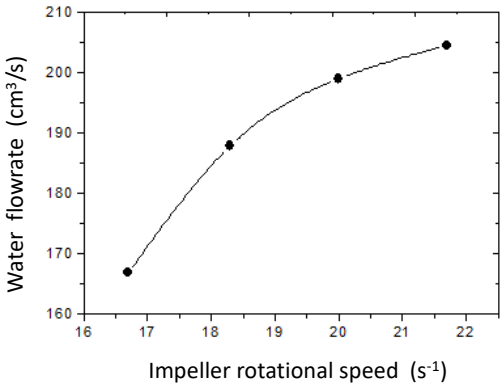

Figure 10: Discharge flow rate (Q_d) as a function of impeller rotational speed (N) operating with water in a Denver laboratory mechanical cell (from Lima, 2009).

The influence of impeller speed (N) on radial fluid velocity (U) measured at the discharge of a Denver impeller (D = 0.07 m) operating under gassed and non-gassed conditions is illustrated in Figure 11. Except at the lowest impeller speed (N = 15.8 s^{-1}), the radial fluid velocity (U) in the absence of air (non-gassed condition) was systematically higher than that in the presence of air (Lima *et al*., 2009). As with centrifugal pumps, the presence of air in the system jeopardises the impeller's ability to transfer momentum to the stirred fluid (water).

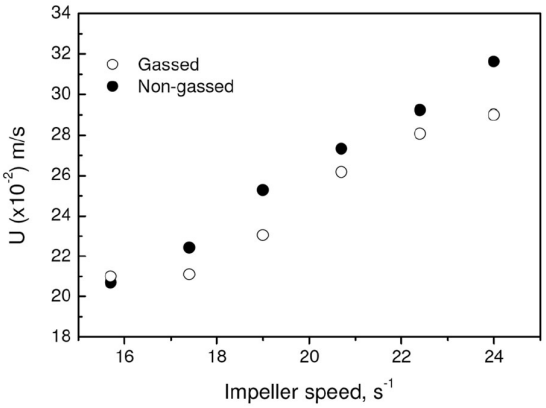

Figure 11: Radial velocity of water flow (*U*) produced by the action of a laboratory Denver impeller as a function of impeller speed (*N*) under gassed and non-gassed experimental conditions (Lima *et al*., 2009).

A mineral slurry is composed of water and solid particles, so when an impeller pumps a pulp from the bottom to the top of a stirred tank (as in a flotation cell), it lifts mineral particles. BFF plays a significant role in particle suspension. The mineral particles must be adequately suspended in the flotation tank to enable them to collide with bubbles and adhere to the bubbles before the assemblage is floated and reaches the froth layer.

Lima *et al*. (2009) conducted experiments in a Denver laboratory mechanical cell to investigate suspension of apatite particles ranging from 90 µm to 254 µm in diameter. The experiments were designed to determine the balance between radial fluid velocity (*U*) produced by impeller action, the terminal settling velocity (U_S) of the mineral particles, impeller rotational speed (*N*), and Zwietering's critical impeller rotational speed (N_Z), under which any particle rests on the bottom of the cell for approximately 1 s (the 1 s criterion). Therefore, the balance between U_S/U and N/N_Z (Figure 12) allows evaluation of whether particles of a specified size will have a tendency to rise within the tank and to what extent. In a flotation tank, coarser particles are most likely to be observed near the bottom, while finer particles are generally expected higher up in the tank (noting that entrainment also plays a role within this range) (Lima, 2009).

According to Figure 12, particle segregation on the bottom of the cell was observed at $N/N_Z < 0.60$ and $U_s/U > 0.08$; full particle suspension occurred at $0.60 \leq N/N_Z < 1$ and $0.06 < U_s/U < 0.10$; particle entrainment to the froth layer by dragging was evidenced at $N/N_Z \geq 1$ and $U_s/U \leq 0.03$. Lima *et al*. (2009) maintained that the fine particles (< 90 μm) were able to be suspended at typical ranges of N, whereas coarse particles (> 254 μm) could not be suspended. Nevertheless, coarse particles were suspended at higher rotational speeds (N > 1300 rpm), while the finest particles were entrained to the froth layer. These results clearly indicate that optimal conditions for suspension of coarse particles promote entrainment of fine particles (valuable minerals and gangue) to the froth. Therefore, selection of the best operational conditions for a particular type of impeller requires a compromise between optimal conditions for suspension of both fine and coarse particles.

Table 1 — Settling terminal velocity of apatite particles (U_s) and critical impeller speed (N_z) to achieve complete off-bottom suspension.

Particle mean diameter, μm	Settling terminal velocity at 20°C, (x10^{-2}), m/s		Critical impeller speed (N_z), s^{-1}	
	Experimental values	Theoretical values	Non-gassed conditions	Gassed conditions
90	0.87 ± 0.07	1.03	19.8	22.0
127	1.90 ± 0.17	1.78	23.5	27.2
180	2.69 ± 0.14	2.65	28.2	31.0
254	3.73 ± 0.12	3.93	32.8	36.0

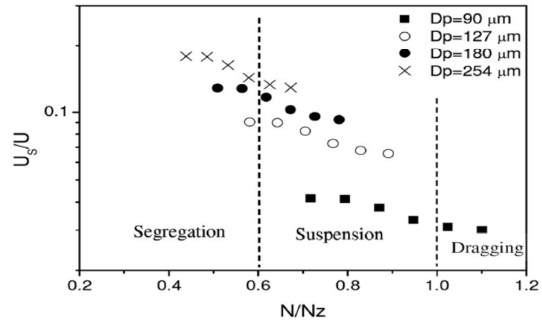

Figure 12: Ranges of U_S/U as a function of N/N_Z for segregation, suspension, and entrainment (dragging to the froth layer) of apatite particles in a Denver laboratory flotation cell (Lima *et al*., 2009).

As illustrated by the fluid streamlines depicted in Figure 9, BFF promotes continuous slurry recirculation within a flotation tank. According to Equation (2), the total circulating fluid flow

rate (Q_{CIRC}) within a stirred vessel is approximately three times greater than the flow rate discharged by the impeller (Q_d) because the latter can induce fluid movement far away from its origin (Edwards and Baker, 1992):

$$Q_{CIRC} \approx 3Q_d, \tag{2}$$

where Q_{CIRC} is the total circulating fluid flow rate (m^3/s), and Q_d is the flow rate discharged by the impeller (m^3/s).

In this regard, BFF generated by the movement of an impeller contributes to mixing in a flotation cell.

The extent of mixing that occurs within a mechanical flotation cell can be evaluated in terms of its mean circulation time (t_{circ}), also referred to as tank turnover time. As given by Equation (3), t_{circ} is the ratio between the effective volume of the flotation tank (slurry volume filling the tank minus the volume occupied by gas bubbles) and the flow rate discharged by the impeller (Q_d):

$$t_{circ} = \frac{V_{eff}}{Q_d}, \tag{3}$$

where t_{circ} is the mean recirculation time (s); V_{eff} is the effective volume (volume of slurry − volume of air) (m^3).

The shorter the mean circulation time (t_{circ}) exhibited by a cell, the greater is the ability of its impeller to promote mixing (Yanatos *et al*., 2008). A cell with a low circulation time implies that air and solids are well dispersed (Deglon *et al*., 2000; Nienow, 1997; Tatterson, 1991; Yianatos *et al*., 2008).

Calculation of the mean circulation time (t_{circ}) demands prior knowledge of the value of the slurry flow rate discharged by the impeller (Q_d). Its determination is not a straightforward task: technical brochures issued by flotation cell suppliers only provide typical values of water (not slurry) flow rates, whereas computational fluid dynamics techniques require information on boundary conditions that are not easily available in the literature. To simplify the problem,

Souza Pinto *et al*. (2018) used the residence time distribution (RTD) of a chemical tracer in an industrial Wemco flotation cell to determine the duration of time (mixing time, t_{mix}) during which the effective volume of the existing slurry in the flotation cell passed the impeller blades at least once, eventually reaching the normalised concentration of the chemical tracer in the entire slurry volume, $E(t)$, to reach its maximum value. Based on this rationale, the magnitude of Q_d can be determined by Equation (4). The principles of RTD are comprehensively reviewed by Fogler (1999).

$$Q_d = \frac{V_f\,(1-\varepsilon_g)}{t_{mix}}, \tag{4}$$

where t_{mix} is the mean circulation time (s); V_f is the fluid volume (slurry or water) filling the flotation tank (m^3); ε_g is the fractional volume occupied by air in the flotation tank.

Figure 13 displays curves obtained from RTD experiments conducted with LiCl as the chemical tracer in Wemco industrial flotation cells (models #190, #164, and #144) to separate carbonates (calcite, dolomite) from silicates (phlogopite, olivine, pyroxene) by reverse cationic flotation of the silicates. Considering the RTD curve for the Wemco cell model #144 operating at 175 rpm (N = 2.9 s^{-1}), the maximum value of the normalised concentration of the chemical tracer $E(t)$ = 0.36 was attained after 1 min residence time (t_{mix}= 1 min). Results and the rationale maintained by Yianatos *et al*. (2008) and Cheng *et al*. (2012) considered the peak of the RTD curve as an indicator of the circulation time (t_{circ}). Therefore, it is reasonable to consider that $t_{circ} \approx t_{mix}$= 1 min. Figure 13 shows that for the different RTD curves for a Wemco cell model #190 with three different impeller speeds (130 rpm, 140 rpm, 154 rpm), the magnitude of t_{mix} decreased from 2.6 min to 1.5 min as N increased from 2.2 s^{-1} (130 rpm) to 2.6 min^{-1} (175 rpm).

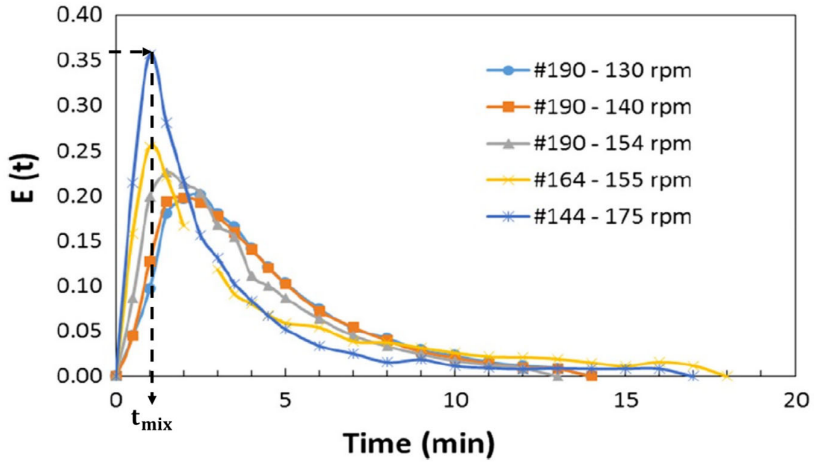

Figure 13: Residence rime distribution curves obtained for Wemco flotation cells (#190, #164 and #144) operating at an industrial scale (from Souza Pinto *et al*., 2018).

The ability of impellers to promote BFF in stirred tanks (mechanical flotation cells) can be represented by a dimensionless number called the pumping number or flow number (N_Q). The flow number is a significant parameter for determining cell suspension properties (Arbiter *et al*., 1976). As shown in Equation (5), N_Q is the ratio between fluid flow rate (Q_d) discharged by the impeller and the reference product ND^3:

$$N_Q = \frac{Q_d}{ND^3}, \tag{5}$$

where N_Q is the pumping or flow number, and D is the impeller diameter (m).

High flow numbers translate to greater pumping capacities, which improve slurry mixing (Joshi *et al*., 1982; Nienow, 1997; Tatterson, 1991). The magnitude of N_Q varies with impeller geometry and operational conditions (air holdup and fluid regime). However, for impellers operating under turbulent flow (Reynolds number (N_{Re}) > 10 000), the magnitude of N_Q is roughly constant (Gray, 1967; McCabe *et al*., 1993; Nagata, 1975). Typical values of N_Q are displayed in Table 1, where it is possible to see a significant difference between values obtained with impellers operating under gassed and non-gassed conditions. The value of N_Q = 0.04 in

Table 1 for a laboratory Denver flotation cell operating under non-gassed conditions is consistent with the value of $N_Q = 0.03$ reported by Gray (1967) for disk-type impellers operating in stirred tanks for the purpose of mixing.

Table 1: N_Q values for flotation cells in relation to fluid regime and aeration (Eimco, 1992; Lima, 2009; Weedon *et al*., 2005).

Equipment	N_Q	Conditions
Eimco cells (Eimco, 1992)	0.64	Industrial cells operating under gas holdup ~ 10% and $N_{Re} > 10^5$
Wemco Cell (Weedon *et al*., 2005)	0.62	Industrial cells operating under gas holdup ~ 10% and $N_{Re} > 10^5$
Wemco cell (Lima, 2009)	0.42	Laboratory cell operating under $J_g = 0.0095$ m/s and $N_{Re} > 10^4$
Wemco cell (Lima, 2009)	0.57	Laboratory cell operating under non-gassed conditions and $N_{Re} > 10^4$
Denver Cell (Weedon *et al*., 2005)	0.05	Industrial cells operating under gas holdup ~ 10% and $N_{Re} > 10^5$
Denver cell (Lima, 2009)	0.03	Laboratory cell operating under $J_g = 0.0015$ m/s and $N_{Re} > 10^4$
Denver cell (Lima, 2009)	0.04	Laboratory cell operating under non-gassed conditions and $N_{Re} > 10^4$

where J_g is the superficial gas velocity (m/s).

2.2.3 Turbulent fluid motion and its influence on impeller performance

TFM is promoted by pressure oscillations that are continuously created in a stirred fluid (slurry or water) by movement of the impeller blades (Schulze, 1984). This process takes advantage of the fact that dynamic pressure (p), due to fluid movement, is proportional to the square of fluid velocity ($p \propto v^2$). This means that fluctuations in fluid velocity can be detected by changes in pressure oscillations in a stirred fluid. Figure 14 illustrates the output of an experiment conducted by Lima (2009) with a laboratory Denver impeller (D = 0.07 m) immersed in water at a depth of 16.5 cm according to a pressure transducer placed 1 cm from the impeller discharge. The impeller rotated at 900 rpm (N = 15 s^{-1}) within a 6 L vessel filled with water, in

the absence of air. Based on a calibration curve expressed by Equation (6), it is possible to assess the temporal averaged pressure value ($\overline{p}$ = 1.46 kPa) and the maximum (1.94 kPa) and minimum (0.78 kPa) values of pressure created by movement of the impeller blades in the fluid (water). The difference between the maximum and minimum pressure values created by the impeller in this experimental system was Δp = 1.16 kPa.

$$p = 0.198\,V, \tag{6}$$

where p is the local pressure (kPa), V is the voltage of the signal output (V).

The ability of impellers to promote TFM in stirred tanks, as mechanical flotation cells, can be represented by a dimensionless number called the Euler number (N_{Eu}) or pressure number (Harris, 1976). N_{Eu} is closely related to the resistance posed by the slurry to the movement of the impeller blades, because it depends on the fluid regime (N_{Re}) and the power number. Impellers work in turbulent regimes, so N_{Eu} is expected to remain constant. As given by Equation (7), N_{Eu} is the ratio between pressure variation (Δp) promoted by the impeller movement in the fluid (water, slurry) and the reference product $N^2D^2\rho$.

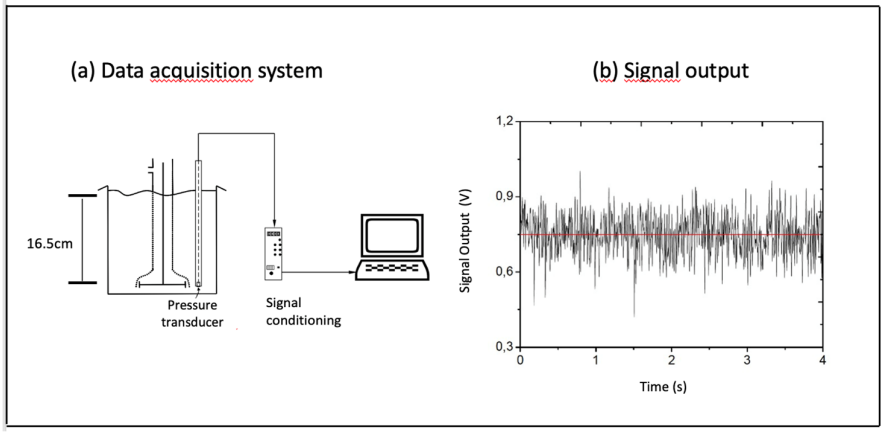

Figure 14: Pressure oscillations in water promoted by movement of a Denver impeller in a laboratory flotation cell (adapted from Lima, 2009).

$$N_{\mathrm{Eu}} = \frac{\Delta p}{N^2 D^2 \rho}, \tag{7}$$

where N_{Eu} is the pumping or flow number; Δp is the pressure difference promoted by the impeller (kPa); ρ is specific gravity of the stirred fluid (kg/m^3).

Therefore, for the experimental system depicted in Figure 14, the value of N_{Eu} is 1.05. This value lies in the typical range of $0.5 < N_{Eu} < 2$ determined by Harris (1986) for laboratory flotation cells. As depicted in Figure 15, TFM may be visualised as a set of eddies of various dimensions that superimpose the basic stationary flow (BFF) and are formed by oscillations of local pressure (and fluid velocity), thereby promoting shear between moving adjacent fluid layers (Schulze, 1984). This means that the higher the value of Δp created by movement of the impeller blades, the higher is the influence of TFM on slurry behaviour within a mechanical flotation cell.

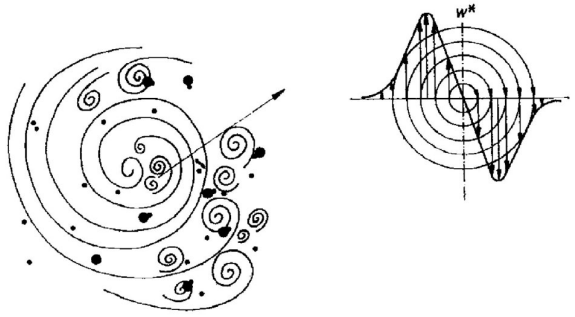

Figure 15: Illustration of turbulent flow (adapted from Schulze, 1984).

Oscillations of local pressure exert shear stresses (τ_{shear}) on gas bubbles, as expressed by Equation (8), while the capillary force (P_c) existing on the bubble surface is represented by Equation (9). The capillary force counteracts τ_{shear} and hinders deformation of the liquid–gas interface (the surface of the bubbles). As shear stress (τ_{shear}) comes to dominate over capillary pressure (P_c), the bubbles are segmented into smaller units, as depicted in Figure 16. According to Schubert and Bischofberger (1998), such a mechanism explains how a continuous air flux introduced into a mechanical flotation cell is dispersed into small bubbles. Besides bubble dispersion, shear stresses created by pressure fluctuations are responsible for turbulent particle–

bubble collisions that help to float fine particles (Schubert and Bischofberger, 1998; Schulze, 1984).

$$\tau_{\text{shear}} \approx 1.9\ \rho_l\ (\varepsilon\ d_{\text{B}})^{\frac{2}{3}}; \tag{8}$$

$$P_{\text{c}} = \frac{4\gamma_{l/g}}{d_{\text{b}}}, \tag{9}$$

where τ_{shear} is shear stress (N/m^2); ρ_l is specific gravity of the liquid through which air bubbles move (kg/m^3); ε is mean energy dissipation (W/kg); d_{b} is bubble diameter (m); P_{c} is capillary pressure (kPa); $\gamma_{l/g}$ is surface tension of the flotation solution (N/m).

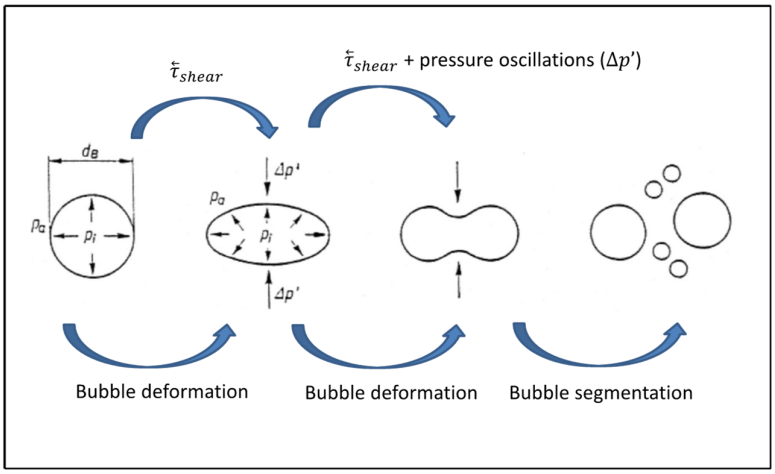

Figure 16: Deformation and segmentation of air bubbles due to pressure fluctuation in mechanical flotation cells (adapted from Schubert and Bischofberger, 1998).

Schulze (1984) found that because air dispersion in mechanical cells is accomplished by pressure fluctuations (inertial forces) that dominate over capillary pressure (surface forces), gas dispersion is influenced by the Weber number (N_{We}), which is the ratio between inertial forces and surface forces, as expressed by Equations (10) and (11). The ratio $\frac{\tau_{\text{shear}}}{P_{\text{c}}}$ represents the

Weber number of the bubble, whereas the ratio $\frac{N^2 D^3 \rho}{\gamma_{l/g}}$ accounts for the Weber number of the impeller. In both cases, the condition for bubble dispersion in the slurry is $N_{We} > 1$.

$$N_{\mathrm{We}}\ (\text{Bubble's Weber number}) = \frac{\tau_{\mathrm{shear}}}{\mathrm{P_c}}; \tag{10}$$

$$N_{\mathrm{We}}\ (\text{Impeller's Weber number}) = \frac{N^2 \mathrm{D}^3 \rho}{\gamma_{l/g}}. \tag{11}$$

Chapman *et al*. (1983) studied dispersion of gas bubbles in water that filled a tank stirred by a two-bladed flat turbine. Keeping the air flow rate to the tank constant and varying the magnitude of the impeller rotational speed, five different profiles of bubble dispersion were identified, as indicated in Figure 17(a) to (e). When the impeller operated under lower values of *N*, the amount of air introduced into the system was higher than the impeller's ability to disperse the air, as depicted in Figure 17(a) and (b). When *N* increased, the ability of the impeller to disperse air bubbles also increased until reaching full bubble dispersion throughout the vessel, as illustrated by Figure 17(e).

From Figure 17, it can be observed that *N* promotes pumping (related to BFF) and shearing (due to local pressure oscillations that characterize TFM). It is reasonable to consider the latter as responsible for bubble dispersion in stirred tanks. Therefore, making an analogy between flotation cells and stirred tanks, it is possible to infer that TFM (caused by impeller rotation in the slurry) is responsible for dispersion of gas bubbles in the system. Therefore, it is important to note that oscillations of local pressure and fluid velocity that cause TFM within mechanical flotation cells promote turbulent collisions between particles and bubbles, playing a major role in the flotation of fine particles (Saint Amand, 1999; Schubert, 1999).

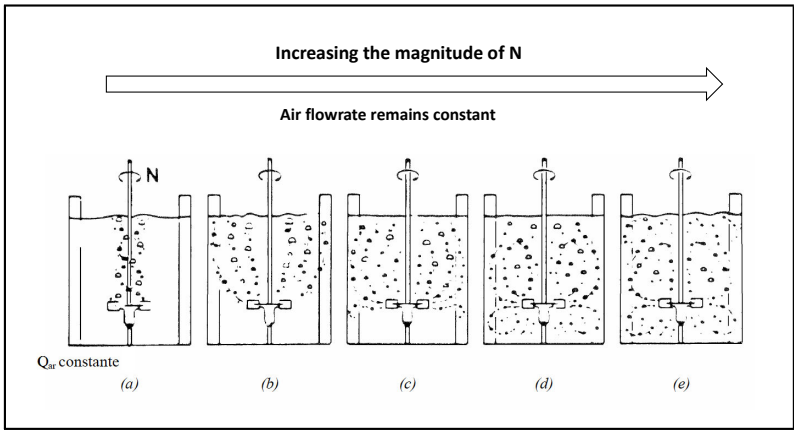

Figure 17: Profiles of bubble dispersion in a stirred tank with increasing impeller rotational speed at constant air flow rate (Chapman *et al*., 1983).

2.2.4 Power number

The net power drawn by an impeller to accomplish its two-fold duty (pumping and shearing) can be written as a dimensionless number known as the power number (N_P) (Equation 12). The power number is especially significant for comparing different impeller designs (Arbiter *et al*., 1976). Bates *et al*. (1963) noted that power consumption by an impeller depends on the system and impeller geometry, such as the dimensions, number of blades, and their assembly, among other impeller aspects. Therefore, Arbiter *et al*. (1976) proposed an additional dimensionless ratio to accommodate impeller geometry differences.

Power numbers typically range from 0.5 to 5. In general, a higher power number indicates a greater fluid displacement capability (Arbiter and Harris, 1962). This is particularly advantageous for fine particles because these generally exhibit poor collision efficiency with bubbles, as per findings by El-Rahiem (2014), Nguyen (2007), and Schubert (2008).

2.2.5 Power number as a function of flow regime (Reynolds number)

The power number (N_P) can be written as the product of the pumping number (N_Q) and Euler number (N_{Eu}), because the net power consumed by the impeller is directly proportional to its

pumping capacity (Q_d) and ability to promote pressure oscillations (Δp). This can be represented by Equation (13):

$$N_P = \frac{P}{N^3 D^5 \rho}; \tag{12}$$

$$N_P \propto \frac{Q_d}{ND^3} \, x \, \frac{\Delta p}{N^2 D^2 \rho}, \tag{13}$$

where P is net power consumed by the impeller (W).

The power number (N_P) of an impeller represents the resistance imposed by the slurry to the movement of the impeller's blades or drag coefficient (C_D). Therefore, because either C_D or N_P varies with the slurry flow regime, these values are typically plotted against the Reynolds number (N_{Re}), as shown in Figure 18 (Uhl and Grey, 1966). As observed in Figure 18, N_P steadily decreases under laminar flow, but tends to be constant under very turbulent flow conditions ($N_{Re} > 10^4$), typically found in mechanical flotation cells (Harris, 1976; Harris, 1986; Leal Filho *et al*., 2002).

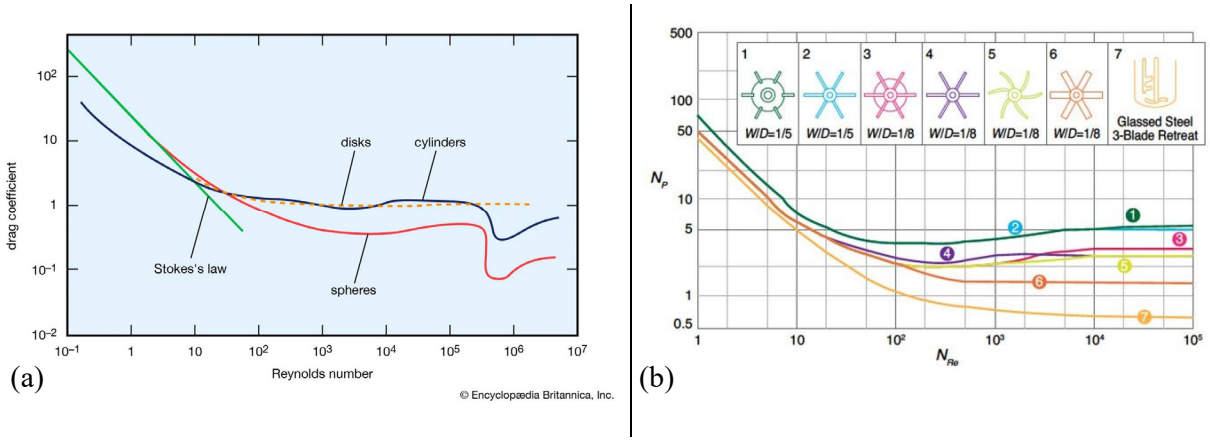

Figure 18: Drag coefficient (C_D) and power number (N_P) as a function of flow regime (N_{Re}). (a) (Encyclopaedia Britannica, accessed 5 December 2022) and (b) (Pretorius *et al*., 2015).

The impeller Reynolds number (N_{Re}) is the ratio between inertial forces and viscous forces, as expressed in Equation (14). The challenge to calculating N_{Re} is a realistic assessment of the slurry dynamic viscosity, mainly when the ore contains coarse particles: coarse particles settle during measurements conducted with conventional rheometers.

$$N_{\mathrm{Re}} = \frac{ND^2\rho}{\mu} \tag{14}$$

where μ = slurry dynamic viscosity at a given temperature (Pa s).

Dimensionless hydrodynamic numbers are useful tools to benchmark the performance of impellers and flotation cells (Rodrigues *et al*., 2001); however, careful consideration is required to avoid reaching incorrect conclusions. According to Equation (12), N_P is proportional to the product of N_Q and N_{Eu}; therefore, the magnitude of both dimensionless numbers is inversely proportional. If the impeller geometry is tailored to promote pumping (BFF), there will be a lack of shearing (TFM), and vice versa. In contrast, when benchmarking impellers of different geometries (for example, the laboratory Denver and Leeds cells) to determine the values of N_{Eu} based on easily assessed information concerning the magnitudes of N_P and N_Q, one must consider other dimensionless parameters, such as that of dimensional analysis, to relate power draw to independent variables.

The dynamic viscosity of water at various temperatures is readily available in the literature. At 27°C, it is 0.8509×10^{-3} Pa s (Ma *et al.,* 2020). To determine the dynamic viscosity of a slurry system, the Krieger–Dougherty equation (15) was employed for a monodisperse system, where φ_m is usually between 0.6 and 0.7 (or 0.63 for randomly packed spheres), and [η] is equivalent to 2.5 for spheres, as stated by Abo Dhaheer *et al.* (2015).

$$\frac{\mu}{\mu_0} = \left(1 - \frac{\varphi}{\varphi_m}\right)^{-[\eta]\varphi_m} \tag{15}$$

where μ and μ_0 are the dynamic viscosities of the slurry and water (Pa s), respectively; φ is volume fraction of the dispersed solid; φ_m is maximum packing fraction; [η] = intrinsic viscosity.

2.2.6 Dimensional analysis to relate power draw to independent variables

Considering the operation of a mechanical flotation cell represented in Figure 19, a list of variables that influence the power (P) drawn by the impeller is given in Table 2.

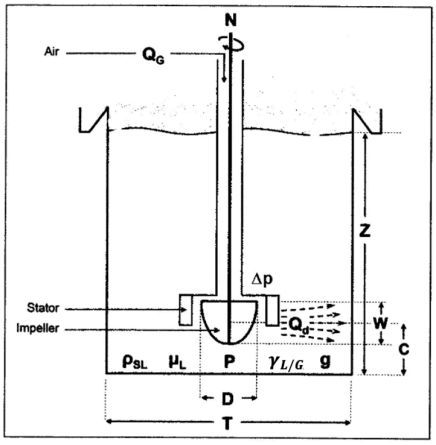

Figure 19: Schematic of a mechanical flotation cell and the variables that influence the power drawn by the impeller (from Westhuizen, 2004).

Based on the information displayed in Table 2, it is important to remark that:

(a) Three variables are related to the aerated slurry (fluid agitated by the impeller): specific gravity (ρ), dynamic viscosity (μ_l), and surface tension of flotation solution ($\gamma_{l/g}$).

(b) Six variables are related to the dynamics of the mechanical system: acceleration due to gravity (g), impeller rotational speed (N), net power drawn by the impeller (P); slurry flow rate discharged by the impeller (Q_d), gas flow rate (Q_g) that feeds the system, and pressure difference promoted by the movement of the impeller blades (Δp).

(c) Five variables are related to cell and impeller geometry: impeller diameter (D), tank diameter (T), impeller blade width (W), distance between the impeller centre and the bottom of the tank (c), and height (Z) of the slurry level in the cell.

(d) These fourteen variables bear the fundamental three dimensions: mass, length, and time, represented by the symbols [M], [L], and [T], respectively.

(e) The variables P, μ_l, $\gamma_{l/g}$, g, Q_d, Q_g, Δp, D, T, W, c, and Z can be written in terms of the repetitive variables D, N, and ρ.

The net power (P) drawn by the impeller depends on the 13 other independent variables (ρ, P, μ_l, $\gamma_{l/g}$, g, Q_d, Q_g, Δp, D, T, W, c, and Z) that comprise the system (Table 2) and can be expressed as a function of all 13 independent variables (Equation (16)).

Table 2: Variables that influence the power drawn by an impeller.

Variable	Unit (SI)	Dimension
Impeller diameter (D)	m	[L]
Tank diameter (T)		
Width of impeller blades (W)		
Distance between centre of the impeller and bottom of the tank (c)		
Level of pulp in the cell (Z)		
Slurry specific gravity (ρ)	kg/m^3	[M][L]$^{-3}$
Slurry dynamic viscosity (μ_l)	Pa s	[M][L]$^{-1}$[T]$^{-1}$
Surface tension of flotation solution ($\gamma_{l/g}$)	N/m	[M][T]$^{-2}$
Acceleration due to gravity (g_a)	m/s^2	[L][T]$^{-2}$
Impeller rotational speed (N)	s^{-1}	[T]$^{-1}$
Power drawn by impeller (P)	W	[M][L]^2[T]$^{-3}$
Slurry flow rate discharged by impeller (Q_d)	m^3/s	[L] [T]$^{-1}$
Air flow rate feeding cell (Q_g)	m^3/s	[L]^3[T]$^{-1}$
Pressure difference promoted by movement of impeller blades (Δp)	Pa	[M][L]$^{-1}$[T]$^{-2}$

However, extensive experimental work is required to find an algebraic expression that fits Equation (16), so a simpler approach based on dimensional analysis (the Buckingham–π theorem) is used to find an expression relating P to these independent variables:

$$P = f(\rho, \mu_l, \gamma_{l/g}, g, N, Q_d, Q_g, \Delta p, D, T, W, c, Z). \quad (16)$$

Demonstration of the Buckingham–π theorem was accomplished by Birkhoff (1960), but is omitted in this text because its rationale is complex and out of the scope of this dissertation. When applying the Buckingham–π theorem to the system of variables presented in Figure 11 and Table 2, it is worth noting:

(a) The n variables listed in Table 2 ($n = 14$) can be clustered in ($n - m$) dimensionless π groups according to Equation (17). The net power draw (P) is the dependent variable, so it must appear in Group π_1:

$$\pi_1 = f(\pi_2, \pi_3\ \pi_4, \dots, \pi_{n-m}). \quad (17)$$

(b) Because the 14 variables that compose the system bear three fundamental dimensions [M], [L], and [T], $m = 3$. Therefore, Group π_1 can be written as a function of eleven (14 – 3 = 11) π groups, as expressed by Equation (18):

$$\pi_1 = f(\pi_2, \pi_3\ \pi_4, \dots, \pi_{11}). \quad (18)$$

(c) The independent variables D, N, and ρ may conveniently appear in more than one π group to account for the fundamental dimensions [L], [T], and [M], respectively, resulting in repetitive named variables.

(d) The eleven π groups gather repetitive variables (D, N, and ρ) plus one non-repetitive variable (P, μ_L, $\gamma_{l/g}$, g, Q_d, Q_g, Δp, T, W, c, and Z). Any π group is the product of the repetitive variables and a single non-repetitive variable. The power of any variable that composes a π group must be solved to accomplish the equality displayed in Table 3. Because the eleven π groups are dimensionless, the power of the three fundamental dimensions must be zero, i.e., $[M]^0[L]^0[T]^0$.

(e) To solve equations (21) to (31) in Table 3, the value of the power (a, i, β, α) for any variable is found and, eventually, an equation related to the eleven dimensionless π groups is determined (Table 4), accompanied by its practical significance.

(f) Using dimensional analysis, it is possible to find an algebraic expression that relates the power dissipated by the flotation impeller to the 13 independent variables, as expressed by Equations (19) and (20). These equations allow benchmarking between the Denver and Leeds laboratory flotation cells.

$$N_P = \frac{N_G\ N_Q\ N_{Eu}}{N_{Re}\ N_{Fr}\ N_{We}}\ \frac{Z}{D}\ \frac{W}{D}\ \frac{c}{D}\ \frac{T}{D}. \quad (19)$$

$$N_P = \left(\frac{Q_g}{ND^3}\right)\left(\frac{Q_d}{ND^3}\right)\left(\frac{\Delta p}{N^2D^2\rho}\right)\left(\frac{ND^2\rho}{\mu_l}\right)\left(\frac{N^2D^3\rho}{\gamma_{l/g}}\right)\left(\frac{DN^2}{g}\right)\left(\frac{Z}{D}\right)\left(\frac{W}{D}\right)\left(\frac{c}{D}\right)\left(\frac{T}{D}\right). \quad (20)$$

Table 3: Groups of variables and respective equations to be solved I

π group	Non-repetitive variable in group	Equation to be solved	Eqn.
π_1	Power drawn by impeller (P)	$\pi_1 = P^a N^i D^\beta \rho^\alpha = [M]^0[L]^0[T]^0$	(21)
π_2	Gas flow rate fed to system (Q_g)	$\pi_2 = Q_g{}^a N^i D^\beta \rho^\alpha = [M]^0[L]^0[T]^0$	(22)
π_3	Slurry flow rate discharged by the impeller (Q_d)	$\pi_3 = Q_d{}^a N^i D^\beta \rho^\alpha = [M]^0[L]^0[T]^0$	(23)
π_4	Pressure difference created by the impeller (Δp)	$\pi_4 = \Delta p^a N^i D^\beta \rho^\alpha = [M]^0[L]^0[T]^0$	(24)
π_5	Slurry dynamic viscosity (μ_l)	$\pi_5 = \mu_L{}^a N^i D^\beta \rho^\alpha = [M]^0[L]^0[T]^0$	(25)
π_6	Surface tension of flotation solution ($\gamma_{l/g}$)	$\pi_6 = \gamma_{l/g}{}^a N^i D^\beta \rho^\alpha = [M]^0[L]^0[T]^0$	(26)
π_7	Acceleration due to gravity (g_a)	$\pi_7 = g_a{}^a N^i D^\beta \rho^\alpha = [M]^0[L]^0[T]^0$	(27)
π_8	Level of slurry in tank (Z)	$\pi_8 = Z^a N^i D^\beta \rho^\alpha = [M]^0[L]^0[T]^0$	(28)
π_9	Width of impeller blades (W)	$\pi_9 = W^a N^i D^\beta \rho^\alpha = [M]^0[L]^0[T]^0$	(29)
π_{10}	Distance between impeller centre and bottom of tank (c)	$\pi_{10} = c^a N^i D^\beta \rho^\alpha = [M]^0[L]^0[T]^0$	(30)
π_{11}	Tank diameter (T)	$\pi_{11} = T^a N^i D^\beta \rho^\alpha = [M]^0[L]^0[T]^0$	(31)

Table 4: Groups of variables and respective equations to be solved II.

π group	Name and significance of dimensionless π group	Expression found by dimensional analysis	Eqn.
π_1	Power number (N_P) is the ratio of power dissipated by the impeller to inertial force $N^3D^5\rho$	$\pi_1 = N_P = \frac{P}{N^3D^5\rho}$	(12)
π_2	Air flux number (N_G) is the ratio of gas flow rate to a reference flow rate (ND^3)	$\pi_2 = N_G = \frac{Q_g}{ND^3}$	(32)
π_3	Pumping number (N_Q) is the ratio of slurry flow rate discharged by the impeller to the reference flow rate (ND^3)	$\pi_3 = N_Q = \frac{Q_d}{ND^3}$	(5)

π_4	Euler number (N_{Eu}) is the ratio of pressure difference created by the impeller to inertial forces ($N^2D^2\rho$)	$\pi_4 = N_{Eu} = \frac{\Delta p}{N^2D^2\rho}$	(7)
π_5	Reciprocal Reynolds number (N_{Re}) is the ratio of inertial forces ($ND^2\rho$) to viscous forces (μ_l)	$\pi_5 = (N_{Re})^{-1} = \frac{ND^2\rho}{\mu_L}$	(14)
π_6	Reciprocal Weber number is the ratio of inertial forces ($N^2D^3\rho$) to surface forces ($\gamma_{l/g}$)	$\pi_6 = (N_{We})^{-1} = \frac{N^2D^3\rho}{\gamma_{\frac{L}{G}}}$	(11)
π_7	Reciprocal Froude number (N_{Fr}) is the ratio of inertial forces (DN^2) to gravity force (g_a)	$\pi_7 = (N_{Fr})^{-1} = \frac{DN^2}{g}$	(33)
π_8	Ratio of level of slurry in tank (Z) to impeller diameter (D)	$\pi_8 = \frac{Z}{D}$	(34)
π_9	Ratio of width of impeller blades (W) and impeller diameter (D)	$\pi_9 = \frac{W}{D}$	(35)
π_{10}	Ratio of distance (c) from impeller centre to bottom of the tank to impeller diameter (D)	$\pi_{10} = \frac{c}{D}$	(36)
π_{11}	Ratio of tank diameter (T) to impeller diameter (D)	$\pi_{11} = \frac{T}{D}$	(37)

2.3 Ability of impeller to suspend particles in mechanical cells

In mechanical flotation cells, the collection of particles by bubbles requires particle suspension: particles that rest on the bottom of the cell are unlikely to interact with gas bubbles and float, whereas particles that are fully suspended in the aqueous medium can collide and attach to bubbles. In this regard, flotation impellers play a major role in particle suspension. The particles that rest on the bottom of the tank are slightly lifted and transported to the upper parts of the vessel by a combination of BFF and TFM. This process creates ascending streaming lines, which is an efficient way for particles to be moved throughout a vessel, allowing for more uniform distribution. After reaching the upper part of the tank, particles start settling. During their descending path, they are able to interact with the ascending bubbles (Westhuizen, 2004).

To model particle suspension in stirred tanks, Zwietering (1958) proposed the off-bottom suspension criterion, also called the 1 s criterion, in which no particle rests at the bottom of a tank for more than 1 s. The value of N equal to or greater than a critical value N_{js} is the impeller

critical rotation to achieve off-bottom suspension. For constant D/T and C/T, the value of N_{js} can be assessed by Equation (38):

$$N_{\mathrm{js}} = S d_{\mathrm{p}}^{0.20} X^{0.13} v^{0.10} g^{0.45} \left(\frac{\rho_S - \rho_l}{\rho_l}\right)^{0.45} D^{-0.85}, \quad (38)$$

where S is a geometric factor related to impeller shape and position in the tank (dimensionless); X is the percentage mass proportion of solids to liquid, (dimensionless); v is the kinematic viscosity of the liquid (Pa s); d_p is particle diameter (m); ρ_s and ρ_L are specific gravities of the solid and suspending liquid (kg/m^3), respectively.

Based on the rationale maintained by Zwietering (1958), Westhuizen (2004) proposed a model to assess the critical impeller speed for particle suspension in a pilot Bateman mechanical flotation cell in the presence of gas bubbles. The model is represented by Equation (39). The critical rotation is represented by N_{jsg}, in which g indicates that the experiments were conducted in the presence of gas bubbles.

$$N_{\mathrm{js}g} = K_{\mathrm{sl}} (d_p)^{0.33\pm0.03} X^{0.17\pm0.03} \left(\frac{\rho_S - \rho_l}{\rho_l}\right)^{0.70\pm0.06} \left(\frac{v_l}{v_{\mathrm{w}}}\right)^{0.05\pm0.04} \left(1 + K_g J_{\mathrm{g}}\right) \quad (39)$$

where K_{sl} is a parameter related to the impeller's ability to suspend particles in the absence of air [dimensionless]; K_g is a parameter related to the impeller's ability to suspend solids under aerated conditions (s/m); v_w and v_l are kinematic viscosities of pure water and a liquid (m^2/s), respectively; J_g is the superficial gas velocity (m/s).

Lima *et al*. (2009) broadened the approach of Westhuizen (2004) by developing a model that incorporates particle suspension in the Bateman (120 L), Denver (6 L), and Wemco (6 L) cells. The model is represented by Equation (40), where the powers of the groups of variables and the magnitudes of K_{sl} and K_g are given in Table 5.

$$N_{\mathrm{js}g} = K_{\mathrm{sl}} \left(\frac{d_{\mathrm{p}}}{D}\right)^{\partial} X^{\mathrm{f}} \left(\frac{\rho_S - \rho_l}{\rho_l}\right)^{h} \left(\frac{v_l}{v_{\mathrm{w}}}\right)^{y} \left(1 + K_g J_{\mathrm{g}}\right). \quad (40)$$

Table 5: Dimensionless critical impeller speed equation parameters for Bateman, Wemco, and Denver cells (Lima *et al*., 2009).

Cell design	$N_{jsg} = K_{sl}\left(\frac{d_p}{D}\right)^{\partial} X^f \left(\frac{\rho_S - \rho_l}{\rho_l}\right)^h \left(\frac{v_l}{v_W}\right)^y (1 + K_g J_g)$					
	K_{SL}	K_G	∂	f	h	y
Denver 6 L	181.4 ± 13.3	201.7 ± 8.5	0.30 ± 0.01	0.20 ± 0.01	0.42 ± 0.01	0.08 ± 0.01
Wemco 6 L	108.1 ±16.2	23.9 ± 3.0	0.30 ± 0.02	0.15 ± 0.02	0.35 ± 0.02	0.05 ± 0.03
Bateman 125 L	73.7 ± 7.3	40.6 ± 2.0	0.31 ± 0.02	0.16 ± 0.01	0.68 ± 0.02	0.06 ± 0.02

Deglon (2005) noted that impeller speed increments tend to improve recovery. High turbulence improves particle–bubble collisions; however, particle–bubble detachment similarly increases (Deglon, 2005; Rodrigues *et al*., 2001; Tao, 2005). Therefore, the speed of the impeller must be well managed. In addition, high impeller speeds favour good gas dispersion through the cell (Ramlall, 2008). The mechanism depicted in Figure 17 corroborates this trend.

According to the rationale presented and discussed in this section, it is possible to use the parameters K_{SL} and K_G to characterize the ability of the Denver and Leeds laboratory cells to suspend particles during flotation.

2.3.1 Airflow number

The flotation process relies heavily on three independent variables: air flow rate, impeller speed, and impeller diameter. These variables form the air flow number (N_G). The air flow rate can be expressed as a dimensionless number (Q_g/ND^3), which is the ratio of the air flow rate to the impeller velocity (Deglon *et al*., 2000). Alternatively, the air flow rate of the cell can be characterised by the superficial gas velocity (J_g). The air flow number is a parameter used in

scale-up criteria (Deglon *et al*., 2000). A very high air flow number can lead to unstable froth surfaces (Nelson and Lelinski, 2000).

2.4 Froude number

The Froude number (N_{Fr}) is another significant parameter in the flotation process. It characterises suspension within the vessel (Nelson and Lelinski, 2000). As given by Equation (41), N_{Fr} is the ratio between inertial and gravitational forces. Zlokarnik (1973) recommended using the Froude number instead of the power number as a scale-up criterion.

$$N_{Fr} = \frac{N^2 D}{g} \tag{41}$$

2.5 Dimensionless numbers

The various dimensionless numbers discussed in this study, such as Reynolds number (N_{Re}), Froude number (N_{Fr}), and Power number (N_P), can be calculated by taking into account operational variables (impeller rotational speed, volumetric airflow, pulp specific gravity, and dynamic viscosity) or geometric variables (impeller diameter). These dimensionless numbers provide a useful tool for analysing flow characteristics of fluids within a cell. A comprehensive summary of these parameters is provided in Table 6, along with their respective formulas and typical ranges, which allow researchers to quickly gain insight into the fluid dynamics. When approaching the hydrodynamic characterisation of flotation cells using dimensionless numbers, one must account for the system to which a specific number refers: for instance, Equation (10) expresses the Weber number for a single bubble, whereas Equation (11) expresses the Weber number of the impeller.

Table 6: Characterisation of flotation hydrodynamics with dimensionless numbers related to impeller characteristics (from Fuerstenau *et al*., 2007).

Number	Definition	Eqn.	Range	Description
Reynolds	$N_{Re} = \frac{ND^2\rho}{\mu}$	(14)	(1–7) × 10^6	Turbulence of fluid's intensity is reflected by this parameter (Wang and Liu, 2021)
Froude	$N_{Fr} = \frac{N^2D}{g}$	(41)	0.1–5	Describes solids suspension and characterisation of mixing intensity (Nelson and Lelinski, 2000)
Power	$N_{\mathrm{P}} = \frac{P}{N^3D^5\rho}$	(12)	0.5–5	Describes dissipation and how the impeller draws power (Tabosa *et al*., 2016b)
Air flow	$N_{\mathrm{G}} = \frac{Q_g}{ND^3}$	(5)	0.01–0.2	Shows operating conditions, as it expresses variables including diameter, impeller speed, and aeration rate (Arbiter *et al*., 1976)
Weber	N_{We} (Impeller) $= \frac{N^2D^3\rho}{\gamma_{l/g}}$	(11)	–	In flotation, this parameter relates to bubble break-up and deformation, and correlates surface tension and hydrodynamic forces (Chu *et al*., 2019)
Euler	$N_{\mathrm{Eu}} = \frac{\Delta p}{N^2D^2\rho}$	(7)	0.5–2	

2.6 Gas dispersion and bubble size

Flotation performance heavily relies on proper gas dispersion, which is a function of three variables: bubble size, superficial gas velocity, and gas hold-up (Schwarz and Alexander, 2006). Bubble size and superficial gas velocity are used to calculate the bubble surface area flux (S_b), which strongly influences the kinetics of the flotation process (Section 2.10). The resultant bubble size is a function of numerous variables, including the air flow rate, frother type and concentration, impeller speed, solids' concentration, and particle size (Shabalala, 2013). Biswal *et al*. (1994) recognised improved efficiency when the bubble size corresponded to the size of particles (e.g., smaller bubbles for smaller particles). This was reinforced by Tao (2005), who

stated that large bubbles aid coarse particles in ascending to the froth zone. Tao (2005) furthermore highlighted that smaller bubbles also play a crucial role in the flotation of coarse particles because they minimise detachment efficiency and thereby improve flotation recovery.

Bubble sizes can be analysed by various measurement techniques, which generally use images and software. Typical bubble sizes range between 1 and 2 mm for an industrial flotation cell (Schwarz and Alexander, 2006). Gas dispersion can be measured in terms of superficial gas velocity to quantify the effect of aeration. In a typical conventional flotation cell, superficial gas velocities range between 0.006 and 0.015 m/s, depending on the operational parameters (Gorain *et al*., 2000). Schwarz and Alexander (2006), however, reported these values to be up to 0.025 m/s.

2.7 Solids' concentration

The solids' concentration (pulp density) can range between 8 and 55 mass% (solids by mass) for a rougher flotation operation, but typical pulps comprise 25–40 mass% (Wills and Finch, 2015). Dilute pulps favour effective bubble loading and minimise the degree of entrainment (Ramlall, 2008). Water restrictions generally favour adoption of high pulp-density operations (Bakker *et al*., 2009). High pulp densities tend to promote entrainment (Ramlall, 2008).

2.8 Scraping rate

Batch laboratory results are further influenced by the chosen scraping rate. Runge (2010) recommended 10 s scraping intervals because this rate allows for effective make-up addition and concentrate pan-changing. Amelunxen *et al*. (2014) noted that laboratory-scale operations generally employ 10 and 15 s scraping rates. These rates result in froth recovery yields between 30% and 40%; a shorter scraping interval results in higher froth recovery. Amelunxen and Amelunxen (2009) noted that 1 scrape/s is necessary to obtain maximum froth recovery. As shown in Figure 18, a high scraping rate is required to enhance froth recovery by ensuring that hydrophobic components do not have sufficient time to drop back into the pulp (Amelunxen and Amelunxen, 2009). High scraping rates reduce inaccuracies associated with the assumption that $R_f = 1$ but they also lead to high entrainment and entrapment levels.

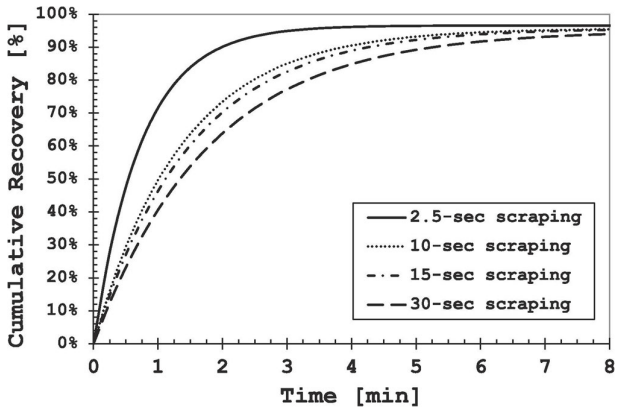

Figure 20: Effect of scraping rate on froth recovery (Amelunxen *et al.*, 2018).

2.9 Metallurgical performance

The collected wet products (concentrate) are subjected to a series of steps, including weighing, filtering, drying, and analysis (if applicable). The results can be reported in many formats. Mineral recovery is typically calculated and plotted against time, as shown in Figure 21. Such a plot can be used to derive and compare data such as k (flotation recovery rate indicator), and R_m. According to Runge (2010), mineral recovery is governed by three particle properties: particle size, liberation, and hydrophobicity. Of these, hydrophobicity is most easily manipulated because it can be modified by adding reagents to the process.

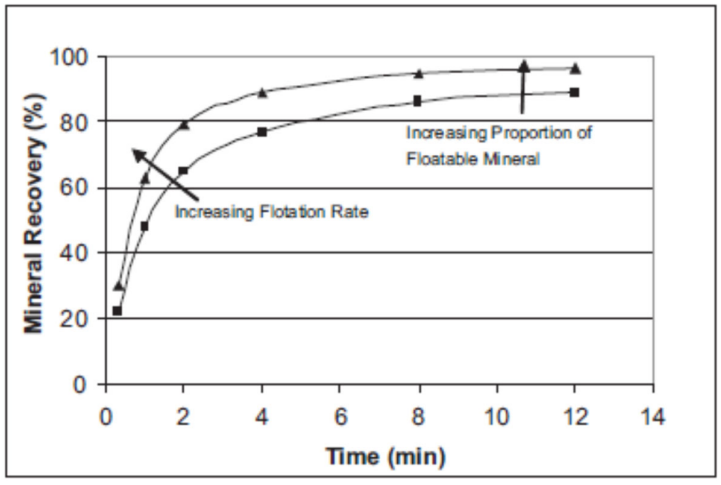

Figure 21: Typical plots of cumulative mineral recovery as a function of time (Runge, 2010).

2.10 Flotation kinetics

Flotation is a rate-controlled process that may be represented as a first-order rate equation. Numerous researchers have used the classical first-order rate equation (Equation (42)) to predict and model flotation kinetics (Bu *et al*., 2017):

$$R = R_{max}\,(1 - e^{-kt}) \tag{42}$$

where R is cumulative recovery at time t (%); R_{max} is maximum recovery, which is approximately asymptotic as $t \to \infty$ (%); k is the "overall" flotation rate constant (s^{-1}); t is flotation time (s).

Scale-up predictions and performance evaluation commonly involve fitting experimental data into Kelsall first-order equations as well as utilising scale-up factors. In general, the flotation rate constant (k) increases with particle size until it reaches an optimum value, beyond which it declines (Horst, 1952).

Grobler (2015) suggested that the single variable k is "oversimplified" because the rate can be affected by underlying conditions, such as surface oxidation. This can perhaps be overcome by separately assigning rate constants for fast- and slow-floating components. Kelsall's unmodified equation offers the solution, and in addition, this model assumes 100% recovery at infinite time (Hay and Rule, 2003).

Gorain *et al*. (1999) showed that a correlation exists between the flotation rate constant k and bubble surface area flux S_b, as expressed by Equation (43). According to Do (2003), k describes the interaction effects of three factors, where P_f stands for chemistry, S_b for equipment, and R_f for operational parameters:

$$k = P_f S_b . R_{f,} \tag{43}$$

where P_f is a parameter that represents the floatability of an ore; S_b is bubble surface area flux (m^2/m^2s); R_f is a froth recovery factor.

As maintained by Vianna (2004), the parameter P_f gives an indication of the floatability of a mineral or ore. It is governed by a particle's hydrophobicity (repellence to water), as well as hydrodynamic conditions that promote particle–bubble collision, adhesion, and transport from the pulp to the froth. High floatability is expected to occur with particles that exhibit high contact angles and high efficiency of collection (E_k), as given by Equation (44):

$$E_k = E_c E_a E_p, \tag{44}$$

where E_c is efficiency of particle–bubble collision; E_a is efficiency of adhesion; E_p efficiency of preservation of the particle–bubble aggregate.

The bubble surface area flux S_b and froth recovery factor can be further described as shown in Equations (45) and (46):

$$S_b = 6\frac{J_g}{D_b}, \tag{45}$$

where D_b is Sauter mean bubble size (m).

$$R_f = \frac{k}{k_c}, \tag{46}$$

where k_c is collection zone flotation rate constant.

S_b can be related to D_b. Typical values of S_b for laboratory and industrial columns and mechanical cells are depicted in Figure 22. Laboratory flotation cells operate under typical values of $S_b < 30\ s^{-1}$ (Vera, 2002).

Gas dispersion characterisation superficial gas velocity (J_g), which represents "how well the air entering the flotation cell is dispersed throughout the cell" (Harbort and Alexander, 2006), is given by Equation (47):

$$J_g = \frac{Q_g}{A}, \tag{47}$$

where A is the cell cross-sectional area (m^2).

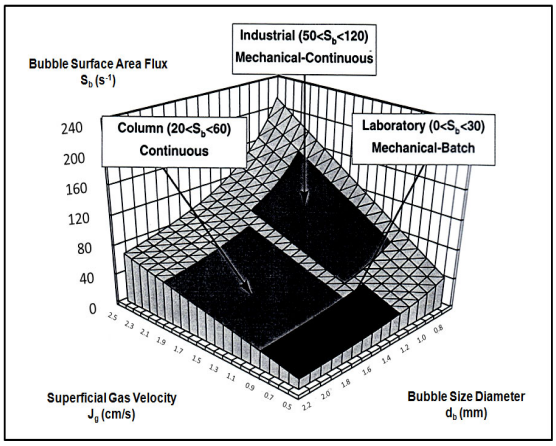

Figure 22: Influence of bubble size diameter and superficial gas velocity on bubble surface area flux (Vera, 2002).

2.11 Silicates

Silica, commonly referred to as quartz, is a combination of Si and O (SiO_2). It is also known as gravel or sand. Quartz is classified in the silicate minerals group, which accounts for 90% of the earth's crust. Quartz is the second most abundant mineral after feldspar. Quartz tends to be associated with other minerals and can be found in almost all mining industries within the host rock, ore, soil, and materials on the surface above the bedrock (Ahmed, 2013). Quartz is usually colourless but can readily take on a variety of colours due to impurities, such as iron (Dunne *et al*., 2019). There are several uses for quartz, such as glass manufacturing (39% of total applications), foundry sand (22%), and silicon metal (Larsen and Kleiv, 2015; Dunne *et al*., 2019).

Unconsolidated deposits throughout the world are sources of high-grade silica. As a result, stripping, open-pit mining, and quarrying techniques are often adequate to extract silica with minimal processing needs. SiO_2 products are produced from these high-grade deposits with a minimum of 95% purity (Dunne *et al*., 2019). Froth flotation is the most effective method for producing the highest purity quartz (Larsen and Kleiv, 2015). Indirect flotation techniques usually remove quartz as a gangue mineral (e.g., in iron plants/industries).

2.12 Reagents

Table 7: Flotation reagents and their applications.

Reagent	Function
Collector	Selectively coats target mineral surfaces to make them hydrophobic and increase the contact angle (Coulson and Richardson, 2019). Examples include xanthates (thiols), which are used for sulfide minerals, and fatty acids, amines, and quaternary compounds for non-sulfide and non-metallic minerals.
Frother	Water-soluble organics capable of producing a stable froth that can carry loaded bubbles until they are removed from the flotation vessel, such as pine oils, cresylic acid, and methyl isobutyl carbinol (Kelly and Spottiswood, 1989). They aid in the formation of small bubbles (Finch *et al*., 2008).
Modifier	Also known as regulators because their function is to either intensify or inhibit the action of the collector. Modifiers include activators, depressants, dispersants, and pH modifiers (Wills and Finch, 2015).
Depressant	Selectively coat certain mineral surfaces to make them hydrophilic. Include reagents such as cyanide, starch, and carboxylmethylcellulose (Wills and Finch, 2015).

Flotation generally requires alteration of a mineral surface. Four reagent types are available for selection: collectors, frothers, modifiers, and depressants, each of which has a specific task, as shown in Table 7. Laboratory batch flotation tests typically determine which combination of reagents is most suitable for the ore being floated (Coulson and Richardson, 2019).

2.12.1 Collector

A mineral's ability to float is based on its hydrophobicity. Most minerals are naturally hydrophilic, so collectors or surfactants are required to alter selected mineral surfaces. A collector is an organic compound that can be classified as either non-ionizing or ionizing. The ionizing compounds can further be divided into cationic and anionic species, as shown in Figure 23, which includes typical structures. Cationic collectors (amine and ether amines) are generally used in the flotation of quartz-containing minerals (Wills and Finch, 2015).

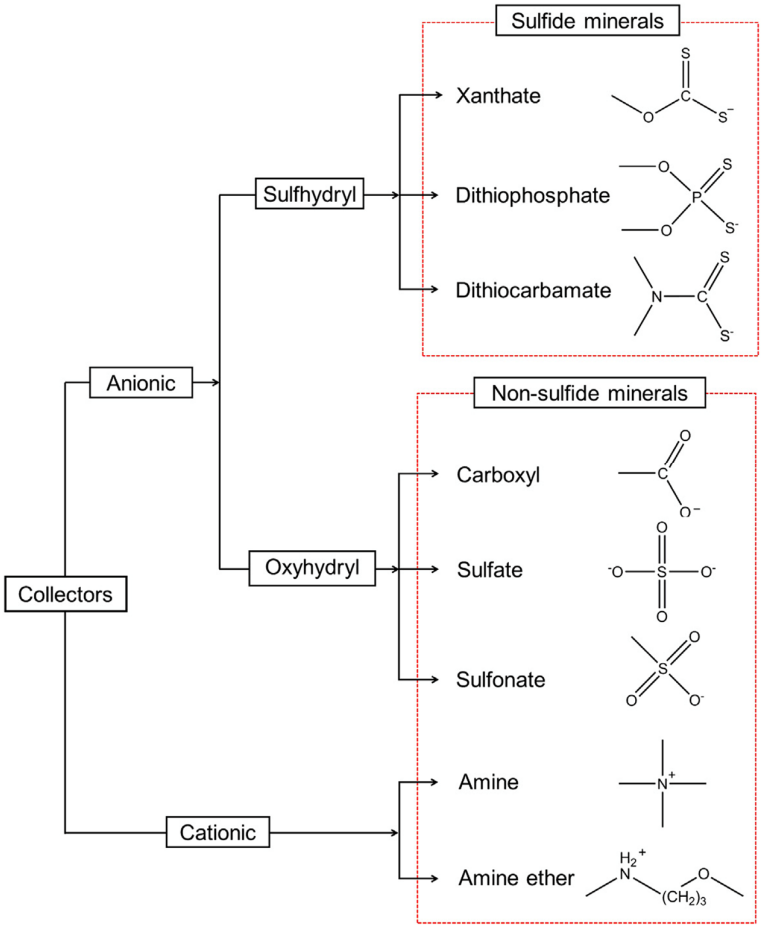

Figure 23: Categorization and applications of ionizing collectors (Wills and Finch, 2015).

Rodrigues *et al.* (2013) showed the ether amine Flotigam EDA collector to be more effective at floating quartz from iron ore than quaternary ammonium salt collectors. Flotation tests on pure quartz, reported by Liu *et al.* (2015), examined three different collectors: dodecylamine (DDA), dodecyl-propyl ether amine, and fatty amine ethoxylate (AC1201). The latter produced the highest quartz recovery, as shown in Figure 24 (Liu *et al*., 2015). Several fatty acids have frother properties (Kelly and Spottiswood, 1989). An alternative to amines for quartz flotation is diluted hydrofluoric acid (HF) solutions with frother (Larsen and Kleiv, 2015).

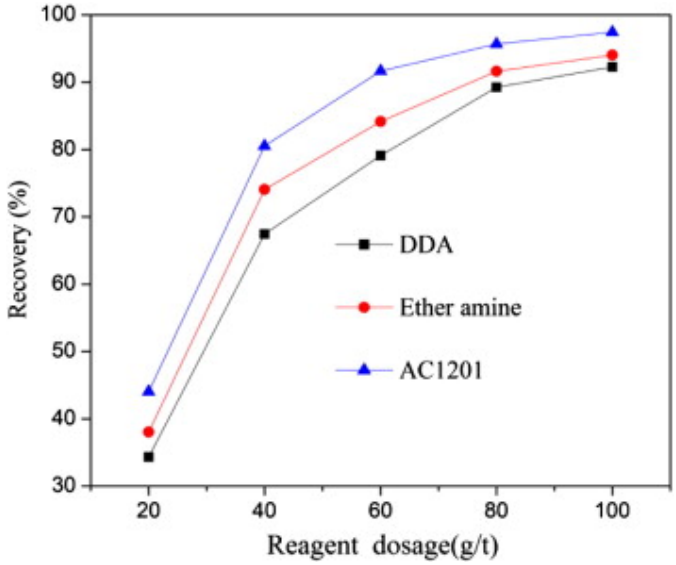

Figure 24: Comparison of DDA, ether amine, and AC1201 collectors on quartz flotation (Liu *et al*., 2015).

2.13 Summary

The flotation process is a crucial step in mineral processing, and its efficiency is highly dependent on various factors. It is important to evaluate these factors and design a system that will maximise mineral flotability, or optimal flotation performance. This is where laboratory batch flotation cells become crucial, as they are commonly used for characterising the process. This chapter provided a comprehensive analysis of the specific factors that impact flotation performance, with a particular focus on firstly the effect of particle size and the necessary conditions to achieve optimum recoveries. Secondly, the contribution of cell design, specifically the impeller, was also examined. The discussion included a range of dimensionless hydrodynamic numbers and corresponding equations. Additionally, practical tools for benchmarking different flotation cells were presented such as making use of a chemical tracer.

Therefore, it is possible to enhance flotation performance by modifying the particle size distribution. The behaviours of two laboratory batch flotation cells, the Denver and Leeds cells, will be evaluated based on particle size and hydrodynamic capabilities.

.

Chapter 3: Methodology

Test work was conducted to evaluate the performance of two flotation cells. The test work was intentionally controlled to limit complexity and avoid bias during interpretation. A non-conventional route was chosen by using a single mineral, quartz, to facilitate comparison of equipment-specific characteristics. Quartz is suitable in that its properties, such as size, liberation, density, and shape, are standardised, so results obtained would be cell dependent, rather than driven by external factors. Additionally, minimal reagents were employed, which could reduce entrainment effects.

3.1 Sample preparation

Approximately 200 kg of pure coarse quartz, sourced from Green Sand CC located in Bapsfontein South Africa, was rotary-split into 1 kg aliquots. One aliquot was pulverised for X-ray diffraction analysis. The results (Figure 25) showed that this material contained 99.9% quartz (SiO_2) and trace amounts of muscovite. Subsamples were dry milled in a stainless-steel rod mill with dimensions of 20.5 cm diameter and 25 cm length, using a mixture of 27 rods in total of 14 mm and 18 mm diameters weighing approximately 14 kg in total. A milling curve was produced to obtain the value of 80% of the material passing 75 µm. This value was confirmed by wet sieving the material on a laboratory sieve shaker to produce the particle size distribution shown in Figure 26. A sizeable amount of the 80% passing 75 µm material was produced, blended, and rotary split into 575 g subsample sizes for flotation test work.

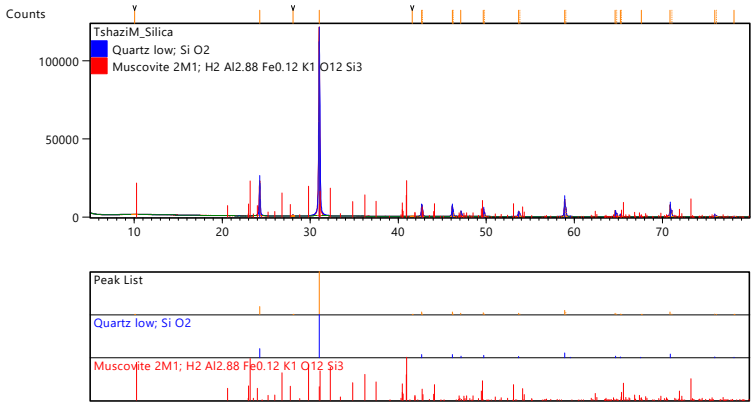

Figure 25: Quantitative X-ray diffraction results for as-received quartz.

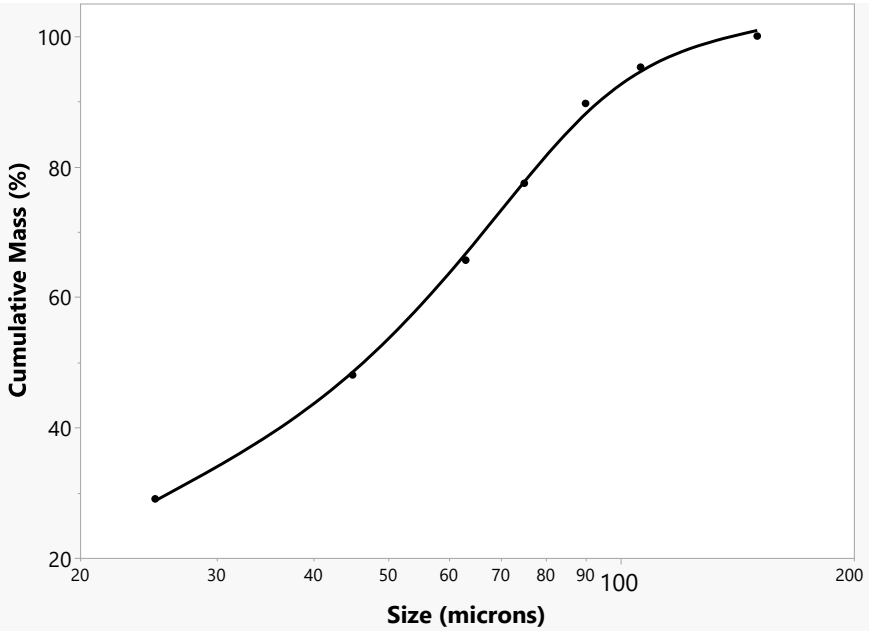

Figure 26: Particle size distribution of milled quartz.

3.2 Calibrations

3.2.1 Cell parameters

Table 8 shows the cell parameters that were used for evaluating hydrodynamic variables in Figure 19.

Table 8: Values of equipment specifications affecting hydrodynamic parameters.

Variable	Unit (SI)	Denver	Leeds
Impeller diameter (D)		0.070	0.074
Tank diameter (T)		0.161	0.158
Width of impeller blades (W)		0.0072	0.0076
Distance between centre of the impeller and bottom of the tank (c)		0.0184	0.0099
Level of pulp in cell (Z)	m	0.149	0.150

3.2.2 Impeller speed

The cells are designed with a built-in tachometer that displays the impeller speed. The cells were further calibrated with an external tachometer to confirm these readings. Tests were conducted using impeller speeds ranging from 1000 rpm to 1400 rpm.

3.3 Air flow rate

An air flow rotameter was used to adjust the rate of air flow into the cells. Dry air from a compressed cylinder was used. The superficial gas velocity (J_g), which serves as an indicator of the cell's aeration ability, was determined by using the displacement method as shown in Figure 27. The cells were filled with 3 L of water with 25 g/t collector, and a 50 mL graduated measuring cylinder with 20 mm diameter was submerged 8 mm below the surface level. The duration needed for air to ascend the graduated cylinder from 10 to 50 mL, thereby displacing 40 mL of water, was recorded with a stopwatch. The measurements were taken in triplicate at five different points around the cross-section of the tanks. The rate of water displacement was then calculated using the formula $J_g = L/T_d$.

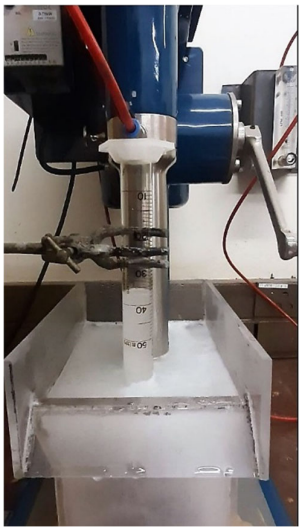

Figure 27: Illustrates the displacement method of measuring J_g.

3.4 Reagent preparation

Fresh collector solution was prepared daily by mixing 1 mL of the Flotigam EDA ether amine collector (supplied by Clariant Southern Africa (Pty) Ltd) with 100 mL of distilled water, giving a 1% (w/v) concentration.

3.5 Experimental procedure and conditions

3.5.1 Dimensionless numbers

The Denver (D-12) and Leeds cells have different impeller designs; therefore, dimensionless numbers (N_{Fr} and N_P) were used to standardise the cells. An equivalent N_{Fr} of 2.88 was set, which translated to the Denver and Leeds cells operating at 1200 and 1175 rpm, respectively. An illustration of the calculation is provided in Appendix B.

After attempting to standardise the cell hydrodynamically using dimensionless numbers, it became evident that this approach did not yield comparable results. Recognising the significant influence of specific cell designs, a manual calibration approach was adopted. This was achieved by adjusting the impeller speeds of the cells, resulting in optimised speeds of 1200 rpm (N_{Fr} of 2.88) for the Denver cell and 1400 rpm (N_{Fr} of 4.09) for the Leeds cell. At these optimised impeller speeds comparable results were achieved.

Aliquots of 575 g quartz were transferred into each of the 3.5 L laboratory flotation cells and 2.87 L tap water was added to make a slurry with a solids' content of 17 mass%. Both cells were constructed from Perspex glass for easy visualisation (Figure 5).

3.5.2 Kinetic tests

The kinetic tests followed a specific methodology. The pulp was adjusted to pH 9.5 using 1% (w/v) concentration of NaOH and the slurry was conditioned for 60 s. The quartz was chemically activated by adding 25 g/t Flotigam EDA ether amine collector before further conditioning for 2 min. This collector exhibits frothing properties, so no frother was added. A rotameter was used to control and maintain the airflow rate at 2 L/min. Concentrates were

collected every 60 s after scraping at 10 s intervals. No top-up water was used for the first concentrate; thereafter, tap water was added to maintain the pulp level throughout the experiment. In general, flotation proceeded until no further froth was recoverable. The tailings and concentrates were weighed, filtered, oven-dried, and weighed again. All experiments were conducted multiple times, with the condition that the standard deviation among the results of each experiment should not exceed 5 %.

3.5.3 Material preparation

The effect of particle size effect was evaluated under the optimised conditions. Four narrow-sized fractions were generated by milling and wet screening using a 30" Sweco screening machine with 106, 75, 45, and 25 µm sieves. The size fractions were classified as fine (−25 µm), intermediate (25–45 µm), medium (45–75 µm), and coarse (75–106 µm) fractions. Each fraction was separately blended and rotary-split to generate representative samples for flotation tests at 1200 rpm in the Denver cell and at 1400 rpm in the Leeds cell using the same condition as in section 3.5.2.

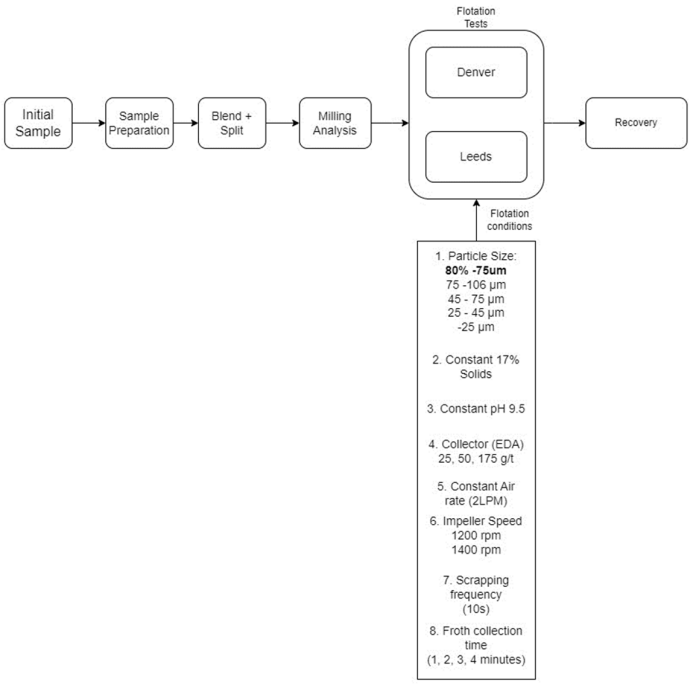

Figure 28: Summary of methodology for kinetic tests.

Further tests on the –25 µm fraction were conducted at 50 and 175 g/t dosages of Flotigam EDA ether amine collector to improve recovery of this fraction. Figure 28 summarises the methodology used.

3.6 Chemical tracer tests

Mixing ability of the cells was investigated using a chemical tracer (1% (w/v) concentration of NaOH). Each cell was filled with 3 L distilled water at pH 6.8. Calibration tests were performed to determine the volume of NaOH required to reach pH 11. A measured volume of NaOH was released at the bottom corner of the cell. A pH electrode placed at the top tracked pH changes due to mixing action under gassed and non-gassed conditions for three different impeller speeds (1000, 1200, and 1400 rpm). The experimental setup is summarised in Figure 29.

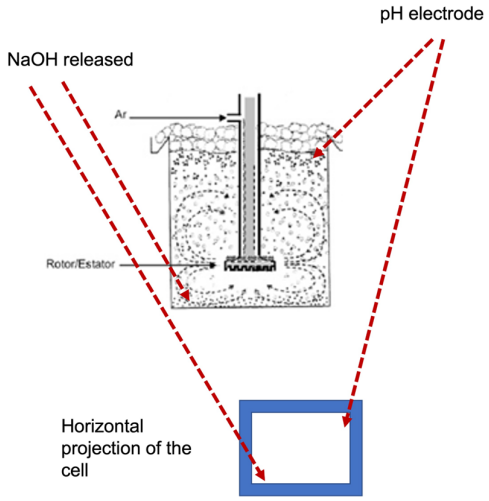

Figure 29: Experimental setup for tracer measurements.

3.7 Power draw determination

Benchmarking of the Denver and Leeds laboratory cells was conducted using the Ellies Efergy E2 Classic Wireless Energy Monitor (https://efergy.com/elite-classic/?v=06fa567b72d7) provided by Efergy Technologies SL based in Spain. This device was used to record the power consumed at impeller speeds ranging from 1000 to 1500 rpm. Tests were conducted under the following

three cell conditions: empty; filled with water (3 L) in the presence of air at 2 L/min; a slurry mixture of quartz and water (~17 mass% solids) in the presence of air at 2 L/min.

The power draw was determined by subtracting the power consumed at a loaded state (slurry or water) from a no-load state (empty).

3.8 Determination of critical impeller speed

The critical impeller speed for the 1 s criterion was determined by filling the cells with water and quartz of the 45–75 µm sized fraction. Solids concentrations of 5, 10, and 15 mass% were used. These tests were conducted in the absence and presence of air. The critical impeller speed was determined by gradually increasing the impeller speed from 100 rpm until all solids were fully lifted off the bottom of the cell. Video clips were taken throughout this process to aid visual observation of when the 1 s criterion was met and complete suspension had occurred.

Chapter 4: Results and Discussion

4.1 Introduction

The laboratory Denver and Leeds flotation cells were compared using two different and complementary approaches: flotation performance and hydrodynamic characterisation. The performance evaluation was conducted at standardised conditions using quartz particles of different sizes to identify any potential advantages or limitations that could arise from either cell type. Hydrodynamic characterisation of the cells was carried out to gain an understanding of the reasons why the cells exhibited different flotation performances.

4.2 Bubble dispersion

The initial evaluation involved testing the two cells under the same experimental conditions (3 L water, 2 L/min air flow rate, impeller speed of 1200 rpm). Figure 30 shows snapshots of the test findings. These experiments revealed that both cells had dead zone areas in the front towards the cell lips, as indicated by the red oval.; furthermore, different bubble shapes and sizes were created. The Leeds cell had a larger dead area, which could be due to its upper longer front design of 95 mm compared to the Denver cell's 65 mm. In addition, the bubble dispersion was observed through video clips, which showed that the bubbles in the Denver cell were spherical and of similar size, whereas the bubbles in the Leeds cell had irregularly sized larger and smaller bubbles. Although these cells were operated under the same conditions, they produced different outcomes, highlighting the influence the design and characteristics of each cell plays in flotation of minerals.

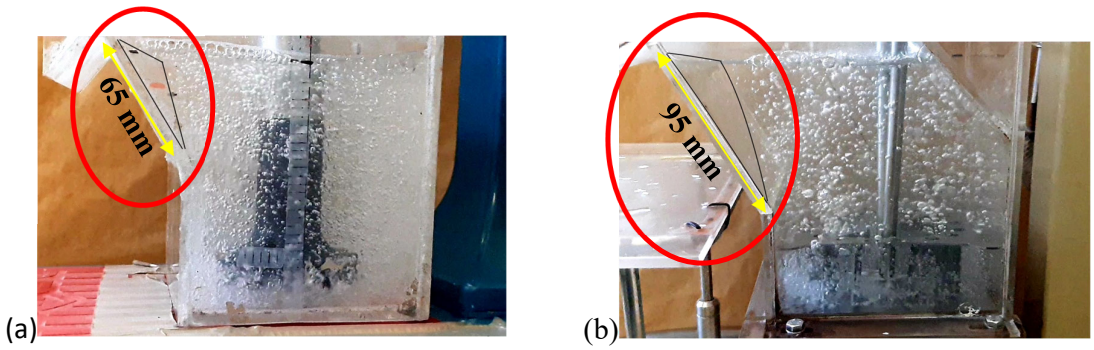

Figure 30: Bubble dispersion and dead zones areas of (a) Denver and (b) Leeds cells.

4.3 Flotation performance

The two cells were standardised by setting an equivalent Froude number of 2.88. This is mainly influenced by the impeller diameter and rotational speed. This gave impeller speeds of 1200 and 1175 rpm for the Denver and Leeds cells, respectively. These respective impeller speeds were used to float quartz under otherwise identical conditions (80% −75 µm, 175 g/t Flotigam EDA ether amine collector).

The cumulative recoveries as a function of time are shown in Figure 31; Appendix B provides the supporting data. The average empirical data yielded by the flotation tests are represented with markers with error bars, showing the deviation between the repeats. The lines represent the fit of the classical flotation first-order kinetic model (Equation (42) to the data. The Denver and Leeds cells showed dissimilar performance under the standardised operating conditions: the Denver cell yielded 92% recovery in 5 min, whereas the Leeds cell achieved this recovery after 6 min. The Leeds cell had a lower flotation rate and delayed response. These results highlight how different equipment configurations can have a significant impact on floatability.

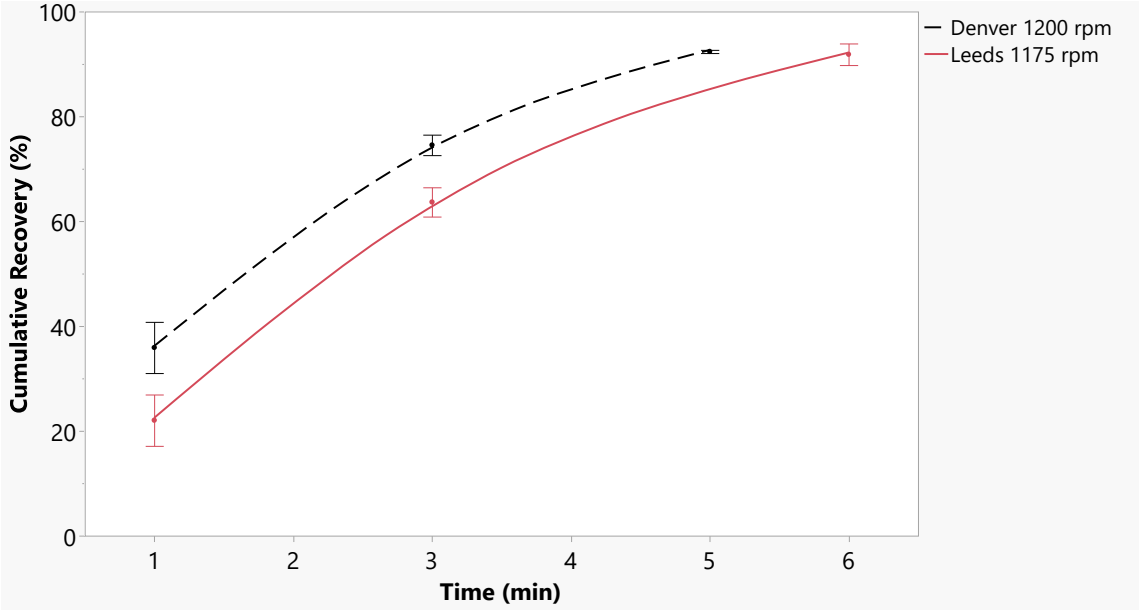

Figure 31: Cumulative recovery of quartz as a function of time for the Denver and Leeds cells at constant N_{Fr}.

The Leeds cell was optimised by adjusting the rotational speed to match the performance of the Denver cell operating at 1200 rpm. This required an impeller speed of the Leeds cell of 1400 rpm, as shown in Figure 32. The higher the impeller speed, the higher was the flotation rate.

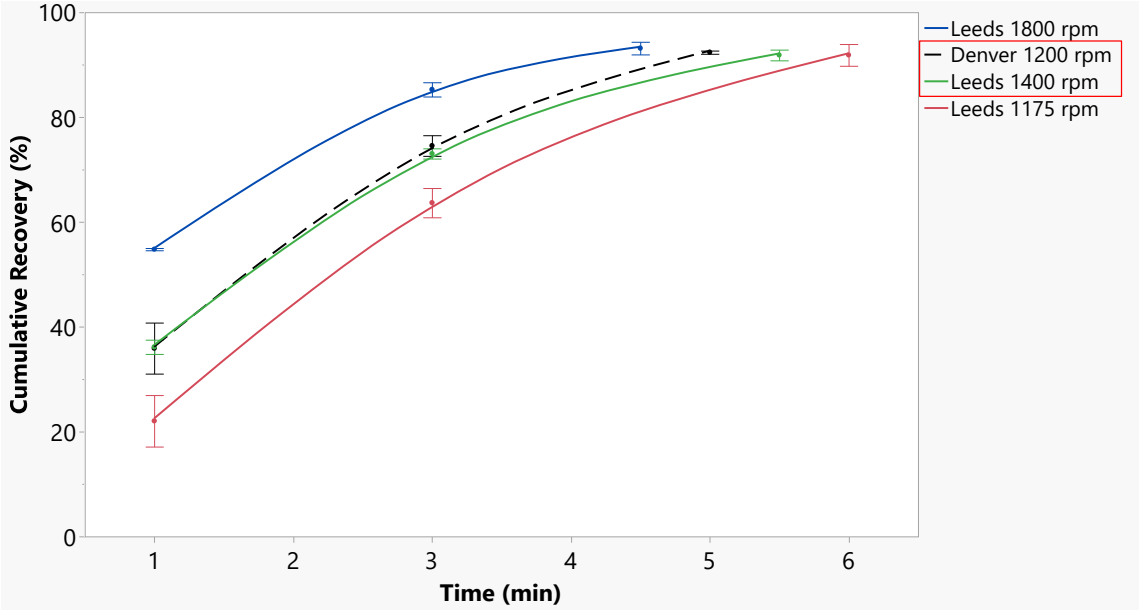

Figure 32: Effect of impeller speed of Leeds cell on cumulative recovery of quartz as a function of time.

4.4 Air flow rate

The results of superficial gas velocity (J_g) measurements of the two cells are illustrated in Figure 33. The data show that both cells reported similar J_g values of approximately 0.22 cm/s at 1200 rpm. There was a negligible increase in J_g when the impeller speed increased from 1200 rpm to 1400 rpm for the Leeds cell. Therefore, it can be concluded that increasing impeller speed did not have a considerable impact on J_g. In addition, this means that the distribution of air over the cross-section of the tank remains largely unchanged with an increase in impeller speed and turbulence. As a result, the sub-aeration systems of both cells did not significantly influence their performances, mainly because an external source of air is introduced into the flotation system at a constant flow rate.

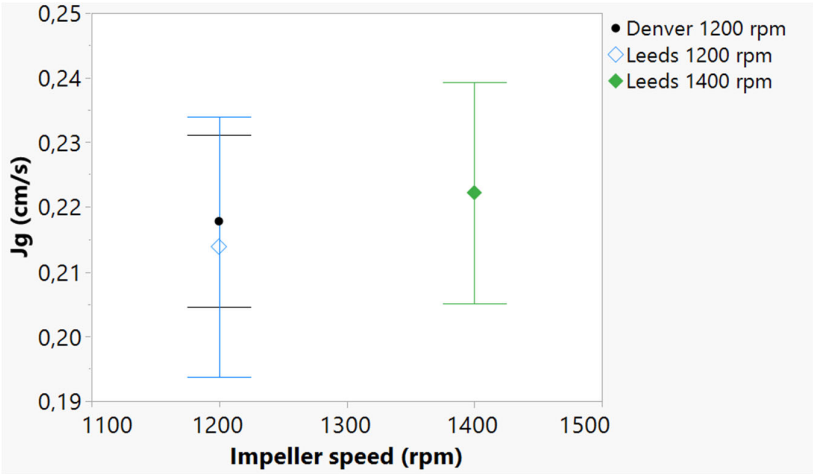

Figure 33: Measurements of J_g for the cells.

4.5 Evaluating the effect of particle size

The results from Figure 32 demonstrate that the Denver and Leeds cells have similar performance when operated at 1200 rpm and 1400 rpm, respectively. This suggests that the two cells can potentially be used interchangeably at these optimised conditions. However, further investigations were necessary to determine if the performance of these cells is dependent on the size of the particles being processed. Four size classes (−25 µm (fine), +25–45 µm (intermediate), +45–75 µm (medium), and +75–106 µm (coarse)) were prepared and floated under the optimal conditions. The complete data set is available in Appendix B.

Figure 34 depicts the results for the two larger size fractions. Recoveries of approximately 80% and 74% for the medium and coarser fractions, respectively, were recorded. Recovery of both fractions was completed in 2.5 min. The cells performed similarly for both size fractions. This was expected because these fractions fall within the optimum flotation range (+25–106 µm), as shown in Figure 7.

Highly stable and voluminous froths were observed for flotation of these size fractions, which contributed to the high recoveries. The cell performances were identical with the +45–75 µm size fraction. This can be attributed to the flotation conditions being optimal in this size range. In contrast, the Denver cell slightly outperformed the Leeds cell (by about 3%) for the +75–106

µm size fraction. There could be many possible hypotheses for this behaviour but given that it involves a change in impeller speed, it is easily attributed to turbulence. The assumption is that turbulence, which can destroy particle–bubble aggregates comprised of coarse particles, is more effectively dampened in the Denver cell than in the Leeds cell.

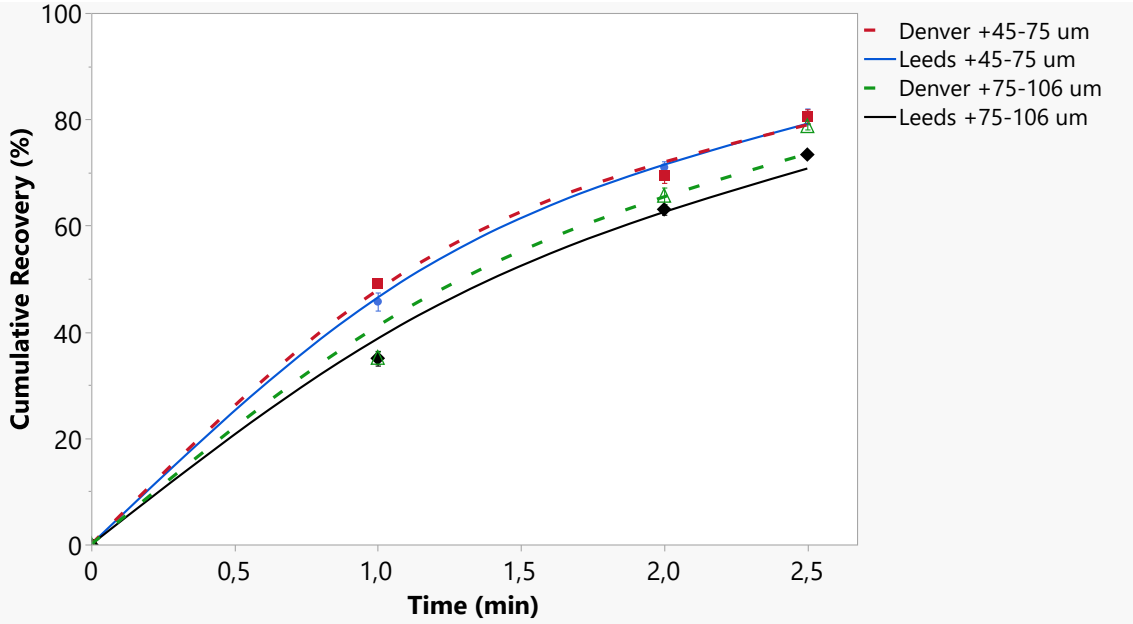

Figure 34: Comparison of Denver and Leeds cells for kinetics curves for flotation of the medium (+45−75 µm and coarse (+75−106 µm) size fractions of silica.

Results from flotation experiments carried out with the smaller fractions (fines (−25 µm) and intermediate (+25–45 µm)) are illustrated in Figure 35. Considering a froth collection time of 2.5 min:

(a) Recovery of the fine fraction (−25 µm) was low for both cells, although the Denver cell promoted slightly higher recovery. However, considering that the kinetic rate was almost double for the Denver cell (0.32 min^{-1}) compared with the Leeds cell (0.18 min^{-1}), the Denver impeller apparently promoted a higher collision efficiency (E_c).

(b) The very poor recovery of the finest particles (−25 µm) in both cells can be also correlated to the low collector dose of 25 g/t and to their larger surface area and consequent low particle–bubble collision efficiencies. Pease *et al*. (2006) demonstrated that fines can float

well provided the flotation conditions are specifically tailored to treat this fraction in a narrow size distribution.

(c) Considering the intermediate size fraction (+25–45 µm), the Denver cell yielded a pronounced higher recovery (74%) than the Leeds cell (63%), indicating that the former offered hydrodynamic conditions that favoured particle–bubble collision. This trend is corroborated by the respective flotation rates of 0.65 min^{-1} and 0.44 min^{-1}.

(d) Comparing the flotation behaviour of the intermediate size fraction +25−45 µm (Figure 35) with that of the two larger fractions (+45−75 µm and +75−106 µm) (Figure 34), the +25−45 µm size fraction took 90 s longer to reach completion. This result is consistent with the findings of Pease *et al*. (2006) that finer particles require a higher residence time than coarser particles.

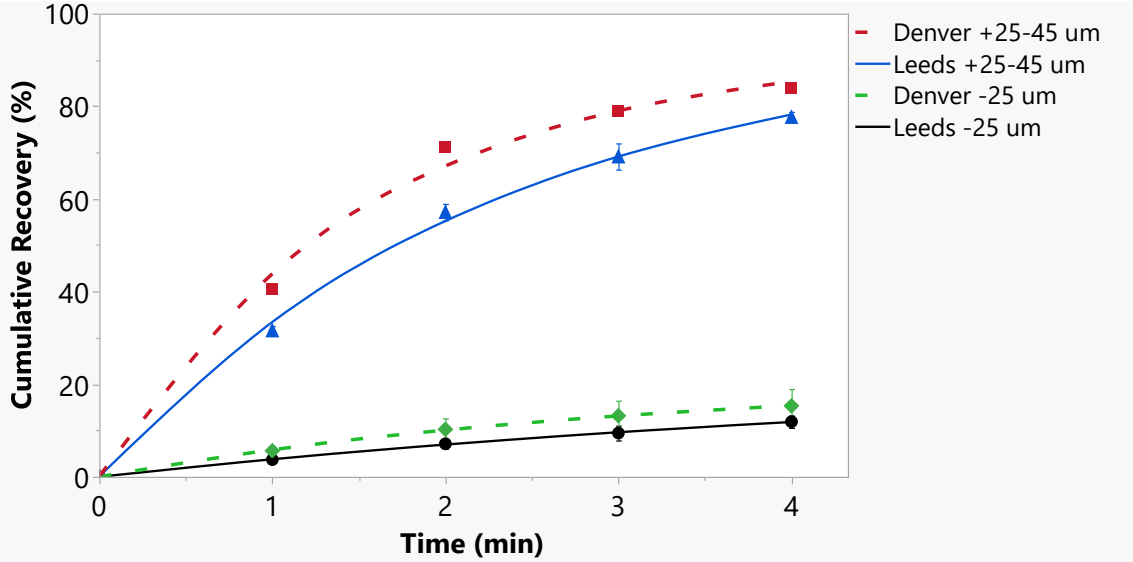

Figure 35: Comparison of Denver and Leeds cells for kinetics curves for flotation of the intermediate (+25−45 µm and fine (−25 µm) size fractions of silica.

Pease *et al*. (2006) demonstrated that finer particles require more reagents due to their large surface area. Higher reagent dosages were therefore investigated to improve fines recovery to at least 60% within 2.5 min, as recorded for the +25 µm size fractions. The collector dosage was increased from 25 g/t to 50 g/t and then further to 175 g/t. Figure 36 shows the effect of

increased collector dosage on the recovery of fines. The flotation process took up to 9 min to reach completion; however, the double dosage failed to achieve the target recovery. Despite the excessive dosage of 175 g/t Flotigam EDA, a 60% equivalent recovery was not achieved within 2.5 min; however, longer flotation times of 3 and 4 min for Denver and Leeds cells, respectively, enabled recoveries exceeding 60% to be attained. The increase in reagent dosage did enhance the overall flotation rates. Additionally, increasing the dosage may have contributed to particle stabilisation, resulting in higher fines recovery from the froth.

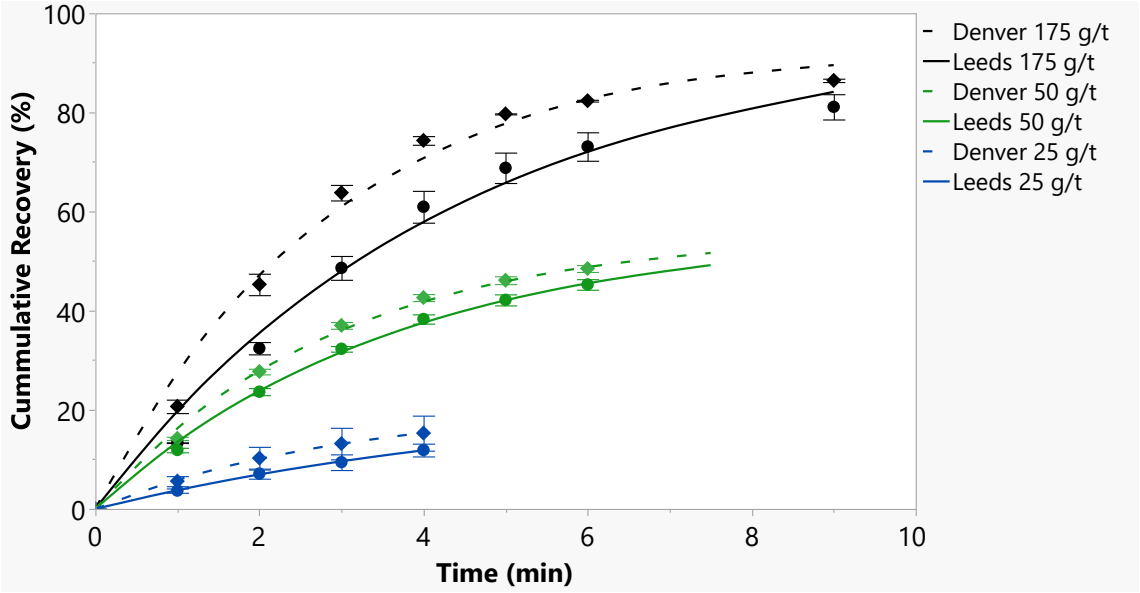

Figure 36: Comparison of Denver (solid lines) and Leeds (dotted lines) cells with respect to effect of collector dosage on flotation of the −25 µm fine fraction.

4.6 Rate constants and maximum recoveries

Modelling of the results can provide a better understanding of how variables such as the kinetic rate influence the flotation response. The empirical results were modelled using the classical flotation first-order model, illustrated by Equation (42). The Solver function available in Microsoft Excel was used to determine the two unknowns (R_{max} and k), as shown in Table 9. These results indicate that both cells exhibited similar characteristics:

(a) The three upper fractions (+25−45 µm, +45−75 µm, and +75−106 µm) showed higher values of R_m (> 90%), whereas the finest fraction (−25 µm) presented the lowest values

of R_m (< 25%). As stated by many authors, fine particles usually show poor flotation performance, mostly due to the lack of particle-bubble collisions.

(b) The kinetic rate (k) was very low for the fine fraction (−25 µm) and increased with particle size. A maximum value of k was reached for +45−75 µm the fraction, but decayed for the coarsest size fraction (+75−106 µm). Such behaviour is due to the efficiency of particle–bubble collection (E_k), which is the product of the collision efficiency (E_c), adhesion efficiency (E_a), and efficiency of preservation of the particle–bubble aggregate (E_p). Fine particles exhibit low values of E_k due to low values of E_c (lack of particle–bubble collision), whereas very coarse particles exhibit low values of E_k because turbulence within the flotation cells can destroy particle–bubble aggregates.

Taking into account the differences exhibited by the Denver and Leeds cells, it is important to note the following:

(a) Considering the finest size fraction (−25 µm), the kinetic rate obtained for the Denver cell (k = 0.32 min^{-1}) was almost double that of the Leeds cell (k = 0.18 min^{-1}). These results indicate that the Leeds impeller had a lower ability to promote particle–bubble collisions than the Denver impeller because all other variables were kept constant. The rate obtained for the +25−45 µm size fraction exhibited the same trend.

(b) The kinetic constants were approximately the same for both cells for flotation of the intermediate (+45−75 µm) and coarse (+75−106 µm) size fractions, although the values for the Denver cell were slightly higher.

Table 9: Comparison of kinetic parameters determined from the classical first-order model.

Size fraction (µm)		−25	+25−45	+45−75	+75−106
Denver	k (min^{-1})	0.32	0.65	0.70	0.53
	R_m	21.24	92.17	95.67	100
Leeds	k (min^{-1})	0.18	0.44	0.63	0.49
	R_m	23.32	94.67	100	100

4.7 Bubble size

An attempt to measure bubble size from each floated fraction was only successful for the fines (−25 µm size fraction). The bubble sizes were determined using ImageJ software. Figure 37

shows a top view of selected bubbles that were observed from the Leeds and Denver cells. The average bubble sizes varied with flotation time: those in the Leeds cell averaged 3.5 mm with a standard deviation of 0.48 mm, while those of the Denver cell had an average diameter of 2.5 mm with a standard deviation of 0.56 mm (Figure 38).

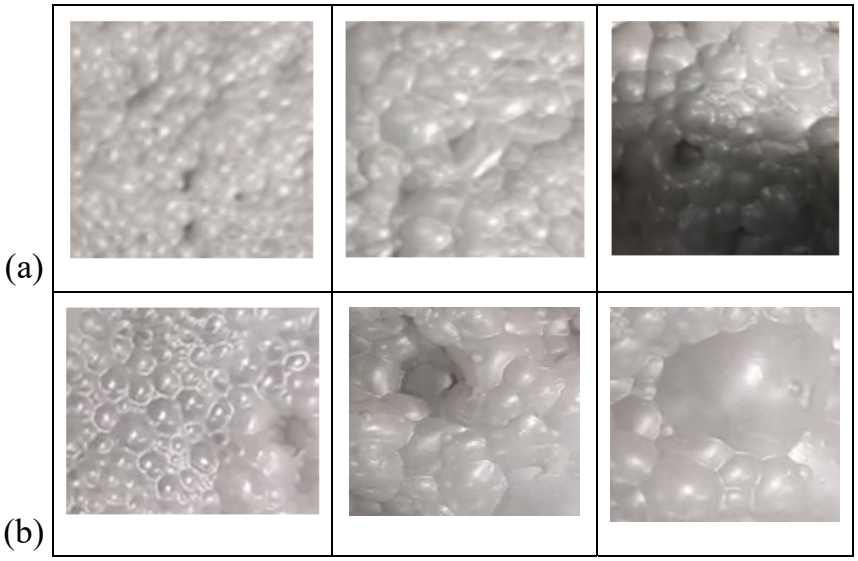

Figure 37: The top view of the froth layer bubbles of the −25 µm size fraction (a) Denver and (b) Leeds cells.

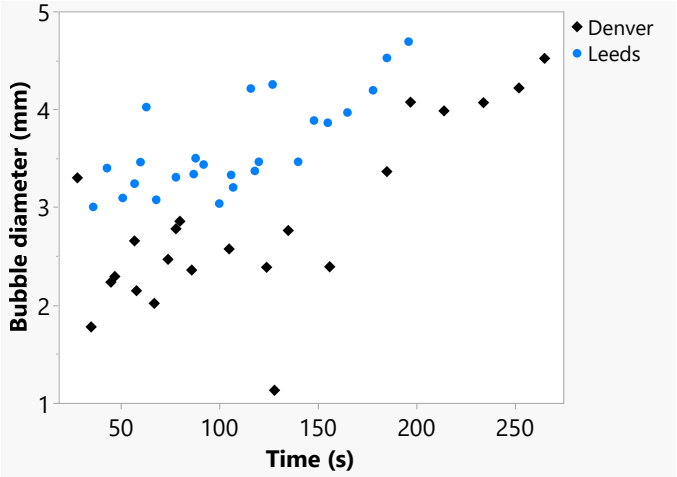

Figure 38: Comparison of bubble diameters during flotation of the fine fraction (−25 µm) as a function of time.

These results suggest that the Denver cell exhibited superior aeration by providing smaller bubbles that can collide more efficiently with particles and a higher bubble surface area available for mineral attachment. This led to better recoveries compared with those achieved with slightly larger bubbles produced by the Leeds cell. This conclusion is supported by the power consumption and power number results presented in Section 4.8.

4.8 Hydrodynamics

4.8.1 Power numbers and Reynolds numbers

The experiments to determine the dimensionless numbers for the two cells were first conducted in a water-only system and then using a slurry. As a consequence of the low viscosities (0.85×10^{-3} and 1.02×10^{-3} Pa.s for water and slurry, respectively), the Reynolds numbers exceeded 100 000 under both conditions. These Reynolds numbers were well within the typical ranges presented in Table 6. The values of the Power and Froude numbers also fell within typical ranges. The full data set is presented in Appendix C. In general, both cells were operating in the transitional region between laminar and turbulent flow, as indicated by the oscillations in the Power numbers in the water-only system and the slurry system.

Figure 39 shows the results for the water-only system. There is a general trend of decreasing power number with an increase in Reynolds number. This supports research of Westhuizen (2004) that the presence of air causes a decrease in the power number because it reduces the effect of density around the impeller. The Leeds cell exhibited slightly higher turbulence intensities and power inputs than the Denver cell, except when the latter operated at 1000 rpm. Higher turbulence intensity and power input are beneficial for increasing collisions between particles and bubbles up to a certain limit, particularly for finer particles, which results in a more efficient flotation process. This result suggests that the Leeds cell is better suited for applications requiring increased turbulence intensity.

The performance of the impellers in a slurry (~17 % solids concentration) is shown in Figure 40. The Leeds cell generated results similar to those obtained for the water-only system; however, the Denver cell showed power numbers averaging 0.77 across the 1000–1500 rpm

range. This indicated minimal changes as the impeller speed increased, which facilitated the fully turbulent regime. The Denver cell is therefore the preferred cell for flotation because it draws lower power while generating sufficient turbulence for successful flotation execution.

Comparing the Reynolds and power numbers for the Denver and Leeds impellers in the absence of solids (Figure 39), both impellers did not achieve a fully turbulent regime, indicating the presence of large eddy vortices, because the power number did not stabilise.

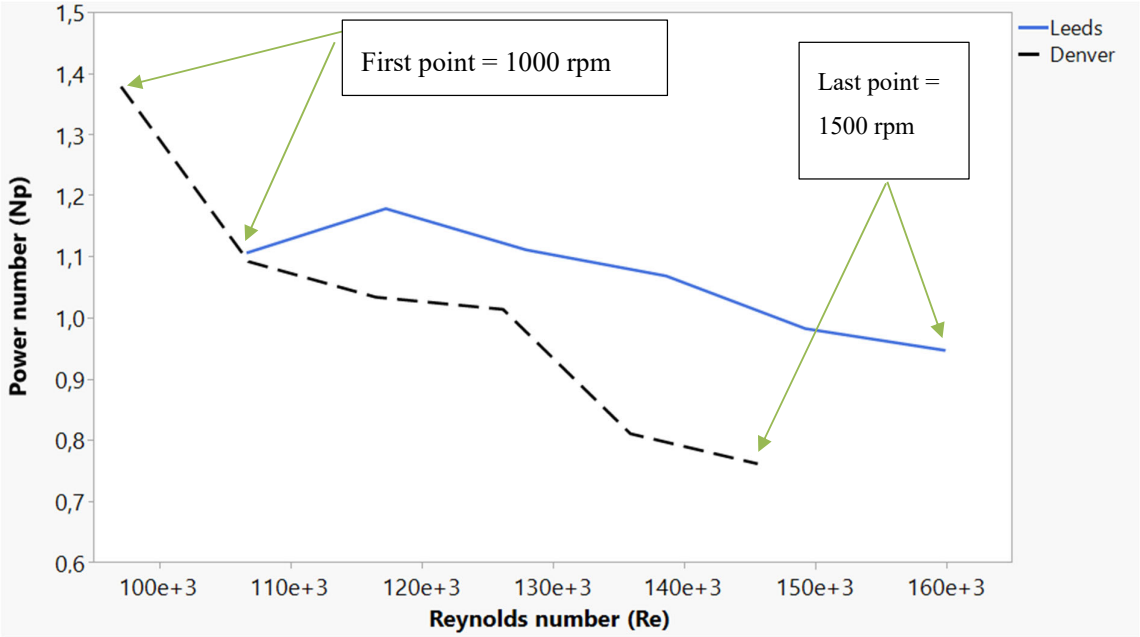

Figure 39: Power number as a function of Reynolds number for mixing of water in the presence of air in Denver and Leeds flotation cells.

The Denver impeller demonstrated a notable ability to overcome the resistance imposed by the presence of solid particles to its movement. This is shown by its power number rapidly approaching the fully turbulent regime, as illustrated in Figure 40. In contrast, the Leeds impeller does not exhibit this same characteristic under the experimental conditions. These results suggest that the Denver cell produced consistent fluid fields while consuming power more efficiently.

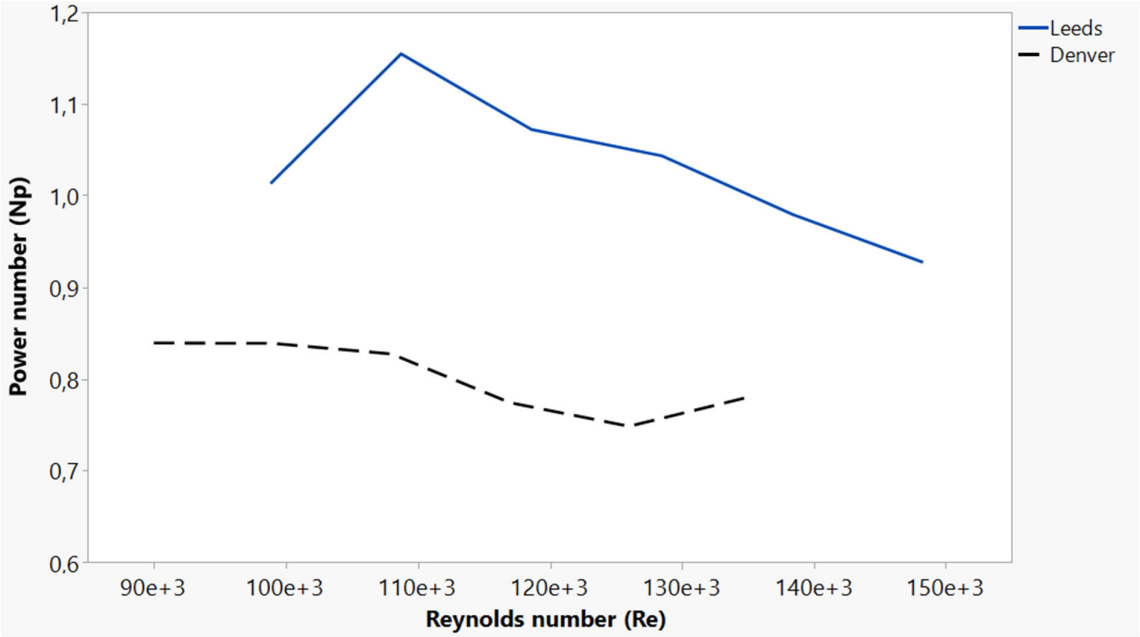

Figure 40: Power number as a function of Reynolds number for mixing water with quartz in the presence of air for Denver and Leeds flotation cells.

4.8.2 Chemical tracer

Testing of the cells using NaOH as a chemical tracer enabled evaluation of the impellers' ability to circulate substances. Table 10 and

Table **11** provide the mixing results for impeller speeds between 1000 and 1400 rpm in the absence and presence of air, respectively. Table 10 indicates that working at 1200 rpm in the absence of air, the Denver and Leeds cells reached pH 11 in 15.61 and 12.96 s, respectively: the Leeds cell promoted slightly faster mixing. There was little effect of rotation speed for the Denver cell, with all tested conditions showing a similar time (15.7 s) to reach pH 11. The Leeds cell required approximately 12.7 s for 1000 and 1200 rpm and 14.4 s at 1400 rpm.

Both cells experienced minor oscillations with increasing impeller speed, except when the Denver cell was operated without air. This cell showed a gentle decline in mixing time with increasing impeller speed. When operating under gassed conditions both cells showed improved mixing ability, with complete mixing achieved within 12 s for all speeds tested. The Denver cell benefitted more from operating under gassed conditions by approximately 3 s

compared with ungassed operation. This demonstrated that the presence of air can improve process efficiency.

Gassed conditions are particularly important because froth flotation takes place under gassed conditions and both cells required approximately the same time to thoroughly mix. However, as depicted in Figure 38, the Denver impeller produced smaller air bubbles than the Leeds impeller. This provides experimental evidence of superior aeration ability shown by the Denver impeller. Bubbles of smaller size are more likely to collide and adhere to hydrophobic particles, so are likely to improve flotation performance.

Table 10: Time required to complete mixing in the absence of air.

	Denver				Leeds		
Speed (rpm)	1000	1200	1400		1000	1200	1400
Average (s)	16.18	15.61	15.48		12.59	12.96	14.36
Std deviation	1.75	1.93	1.60		1.70	1.05	1.33

Table 11: Time required to complete mixing in the presence of air.

	Denver				Leeds		
Speed (rpm)	1000	1200	1400		1000	1200	1400
Average (s)	11.52	12.88	11.80		11.66	12.28	11.63
Std	1.58	1.60	1.71		1.29	0.71	0.60

These findings demonstrate the potential of air to improve process efficiency in applications that require agitation. The study provides insights to how these two impeller types respond differently under varying conditions, such as their ability to mix substances effectively over a given period, depending on their rotation speed. This knowledge allows for a better understanding of cell performance capabilities and limitations associated with each design.

4.8.3 Flow rate and pumping number

The fluid flow rate discharged by the impeller at different speeds was used to determine the impeller's effectiveness in pumping or circulating fluid within a cell. The data from the chemical tracer tests was utilized to determine the discharge flow rate (Q_d). The results, as shown in Table 12, indicate that both the impellers, in the presence and absence of air, discharge fluid at a constant rate. In the presence of air, the flow rate discharged by both cells averaged around 0.25 x 10-3 m3/s. It is noteworthy that the Leeds cell exhibited equal or slightly higher flow rate compared to the Denver cell, however, this did not necessarily translate into effective flotation of minerals as confirmed by the kinetic test in section 4.3.The study by Lima et al. (2009), shown in Figure 10, showed higher flowrates were generated with higher impeller speed, the rates were rather constant with the Denver and Leeds cells. In general, operating with a higher impeller speed did not provide any significant advantage in the pumping or circulating fluid. Therefore, the ability for these cells to pump or circulate fluid was similar.

Table 12: Comparison of flow rate discharge by the impeller of the Denver and Leeds cells as a function of the impeller speed in the absence and presence of air.

Q (m3/s) (x 10^-3)	Denver				Leeds		
Speed	16.7 (1000)	20 (1200)	23.3 (1400)		16.7 (1000)	20 (1200)	23.3 (1400)
No Air	0.19	0.19	0.19		0.238	0.232	0.209
2 L/Min	0.26	0.23	0.25		0.257	0.244	0.258

Figure 41 depicts the pumping number in relation to impeller speed in the presence of air. Both devices had a pumping number between 0.03 and 0.04, except for the Denver at 1000 rpm, which reached 0.045. As impeller speed increased, the pumping numbers decreased. This is consistent with previous studies by Lima *et al*. (2009) and Gray (1967), who found that the pumping number should be approximately 0.03. Gray also concluded that the pumping number generally remains constant for Reynolds numbers greater than 10 000. In the present study, the Reynolds numbers were an order of magnitude higher.

That the Denver and Leeds impellers exhibited similar pumping numbers is an indication that both impellers can promote mixing in the slurry with similar efficiency. However, the Leeds cell had a higher power number, so more power is consumed to overcome resistance of the slurry to create flow: the power dissipated by the Denver impeller is better used to disperse air bubbles and more efficiently promote particle–bubble collisions.

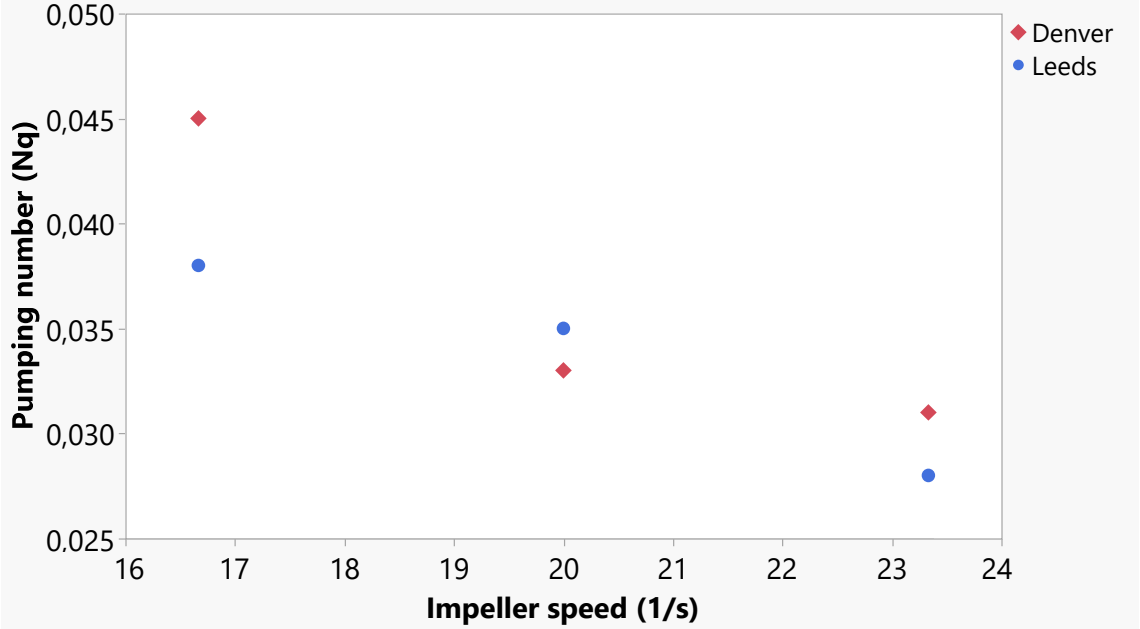

Figure 41: Comparison of pumping numbers of the Denver and Leeds cells as a function of the impeller speed in the presence of air.

4.8.4 Critical impeller speed

The 45–75 µm size fraction was used to determine the critical impeller speed. As the impeller speed was gradually increased, an increasing proportion of solids became suspended in both cells: materials at and near corners of the cells were slowest to become suspended. The critical impeller speeds of both cells under gassed and ungassed conditions are notably different, as shown in Table 13. At these values, the particles do not rest on the bottom of the cell for more than 1 s.

The critical impeller speed for the Denver cell under ungassed conditions was found to be constant at 500 rpm. Gassed conditions at 5 and 10 mass% solids required 600 rpm, while the

15 mass% slurry required 550 rpm. The Leeds cell required higher rotational speeds in both gassed and ungassed conditions: 750 rpm for 5 mass% solids and 800 rpm for 10 and 15 mass% solids. It is evident that the presence of air negatively affected suspension of the solids in both cells, but more so in the Leeds cell (46% difference between gassed compared with ungassed conditions) than the Denver cell (16%). These results clearly show the Denver cell is less affected by increasing solids' content. The Leeds cell required significantly more energy to suspend the same mass of solids. Therefore, a Denver cell would be a better choice for applications requiring higher solids' content due to its superior efficiency and lower energy consumption.

Table 13: Comparison of critical impeller speed (N_{js}) with solids concentration.

	Denver (rpm)		Leeds (rpm)	
Solids (%)	No air	Air	No air	Air
5	500	600	750	1000
10	500	600	800	1200
15	500	550	800	1250

Chapter 5: Conclusions

A study of the flotation efficiency and hydrodynamic characteristics of laboratory-scale Denver and Leeds flotation cells, which were both 3.5 L, was undertaken. It was advantageous to use a single mineral system, quartz, because it allowed the mineralogy, and hence hydrophobicity of the mineral surface, to remain constant throughout the experiments. An amine collector was employed.

It is considered that the batch test will remain essential to process development testwork in the metallurgical industry.

Comparative tests between the two cells revealed dissimilar performance under standardised operating conditions, as follows:

(a) Different bubble flow patterns with varying degrees of dead zone were observed: the Leeds cell exhibited slightly larger bubbles and dead zones than the Denver cell. Optimal operating conditions were therefore identified under which similar performance could be achieved in both cells.

(b) In both the presence and absence of particles, the Leeds impeller gave higher power numbers than the Denver impeller. This implies that the slurry imposed more resistance to the movement of the Leeds impeller, which can be attributed to its unique design. The Leeds impeller must therefore dissipate more power than the Denver impeller to accomplish its tasks, such as promoting particle and bubble dispersion and particle–bubble collisions.

The results of the experiments demonstrated that the Denver and Leeds cells must be operated at different rotational speeds (1200 rpm and 1400 rpm, respectively) to obtain similar performance. This difference is supported by the higher values of power number required by the Leeds impeller. The Leeds impeller dissipated a considerably greater amount of power just to create flow, whereas the Denver impeller, because it operates under fully turbulent conditions, converts torque into flow in a more efficient way (bubble dispersion, particle dispersion, and particle–bubble interactions).

The test work also showed that particle size has a significant influence on mineral recovery: finer particles require more reagents and longer flotation times for optimal recoveries; thus,

process efficiency can be improved by understanding how best to optimize particle size distribution. The Denver cell performed better than the Leeds cell for this particular application because the latter required a higher impeller speed to yield similar recoveries.

The laboratory Denver cell appeared to effectively handle all size fractions.

The chemical tracer tests revealed that the mixing ability of the Leeds cell was marginally faster than that of the Denver cell; however, when operating under gassed conditions, there was a decrease in mixing time for the Denver cell by approximately 3 s. No significant difference in performance between gassed and non-gassed conditions was observed with respect to the Leeds cells. This indicates that different types of impellers respond differently to varying operational conditions.

The dimensionless numbers of both cells fell within typical ranges, indicating that their operation conformed to expected performance levels. The turbulent regime was identified as being the operational zone of both cells. The Denver cell proved more efficient than the Leeds cell due to its ability to draw less power while operating under comparable conditions. This was attributed to factors such as its design and air input mechanism.

The critical impeller speed tests yielded valuable insights into the effect of air on solid suspension in both cells. The results suggest that the Leeds cell is more adversely affected by air, requiring higher rotational speeds to achieve complete suspension, even under non-gassed conditions. The Denver cell achieved complete suspension at lower rotational speeds. These findings are important for optimising process parameters and maximising efficiency in industrial applications involving solid–liquid suspensions.

Considering the overall performance metrics evaluated in this study, the Denver cell demonstrated superior performance This makes it an ideal choice for benchmarking laboratory tests. Its long-term wide usage throughout the world demonstrates that this cell has proven effective in many different applications. It is clear, with the abovementioned advantages, why so many laboratories rely on Denver cells for their testing needs.

Finally, it should be noted that the operator, whose role currently plays an integral part in reliable data collection using traditional laboratory equipment, will continue to be phased out

as new technology, which offers a higher level of reproducibility and accurately correlates data to industrial scale, continues to emerge.

Chapter 6: Recommendations

The following recommendations are made for further investigation that could confirm and enhance the results presented in this dissertation.

It would be valuable to identify which laboratory cell corresponds best to industrial-scale operation. This would require scaling-up of the Denver and Leeds test conditions and running pilot-plant tests to expand the test settings. Identification of the optimal choice between different types and models of commercially available cells requires careful deliberation and evaluation of the associated advantages and disadvantages.

Other laboratory-scale flotation devices, such as a bottom-driven cell, could be included in the comparative analysis.

Chapter 7: References

Abo Dhaheer, M. S., Al-Rubaye, M. M., Alyhya, W. S., Karihaloo, B. L. and Kulasegaram, S. (2016). Proportioning of self-compacting concrete mixes based on target plastic viscosity and compressive strength: part i - mix design procedure. *Journal of Sustainable Cement-Based Materials*,*5*(4), 199–216. https://doi.org/10.1080/21650373.2015.1039625.

Ahmed, A. (2013). Geological Overview of White silica Sands.

Amelunxen, P., LaDouceur, R., Amelunxen, R. and Young, C. (2018). A phenomenological model of entrainment and froth recovery for interpreting laboratory flotation kinetics tests. *Minerals Engineering*, *125*, 60–65. https://doi.org/10.1016/j.mineng.2018.05.003.

Amelunxen, P., Sandoval, G., Barriga, D. and Amelunxen, R. (2014). The implications of the froth recovery at the laboratory scale. Minerals Engineering, 66–68, 54–61. https://doi.org/10.1016/j.mineng.2014.04.022.

Amelunxen, R. and Amelunxen, P. (2009). Methodology for executing, interpreting, and applying kinetic flotation tests in scale-up, Part 1. Gecamin, Santiago, Chile.

Arbiter, N. and Harris, C.C. (1962). Flotation machines. In: D.W. Fuerstenau (Editor), Froth Flotation 50th Anniversary Volume, Pap. 14, Am. Inst. Min., Metall. Petrol. Eng., New York.

Arbiter, N., Harris, C. and Yap, R. (1976). The air flow number in flotation machine scale-up. International Journal of Mineral Processing 3, 257-280.

Bakker, C. W., Meyer, C. J., Deglon, D. A. and Special issue: Computational Modelling. (2009). Numerical modelling of non-newtonian slurry in a mechanical flotation cell. Minerals Engineering, 22(11), 944–950. https://doi.org/10.1016/j.mineng.2009.03.016.

Bates, R. L., Fondy, P. L. and Corpstein, R. R. (1963). Examination of some geometric parameters of impeller power. Industrial and Engineering Chemistry Process Design and Development, 2(4), 310–314. https://doi.org/10.1021/i260008a011.

Bertrand, J., Couderc, J. P. and Angelino, H. (1980). Power consumption, pumping capacity and turbulence intensity in baffled stirred tanks: comparison between several turbines. Chemical Engineering Science, 35(10), 2157–2163. https://doi.org/10.1016/0009-2509(80)85040-8.

Birkhoff, G. (1960). Hydrodynamics – A study in logic, fact and similitude. Princeton University Press.

Biswal, S. K., Reddy, P. S. R. and Bhaumik, S. K. (1994). Bubble size distribution in a flotation column. *The Canadian Journal of Chemical Engineering*, *72*(1), 148–152. https://doi.org/10.1002/cjce.5450720123.

Bu, X., Xie, G., Peng, Y. and Chen, Y. (2016). Kinetic modeling and optimization of flotation process in a cyclonic microbubble flotation column using composite central design methodology. *International Journal of Mineral Processing*, *157*, 175–183. https://doi.org/10.1016/j.minpro.2016.11.006.

Bu, X., Xie, G., Peng, Y., Ge, L. and Ni, C. (2017). Kinetics of flotation. order of process, rate constant distribution and ultimate recovery. *Physicochemical Problems of Mineral Processing*, *53*(1). https://doi.org/10.5277/ppmp170128.

Bulatovic, S. M., Wyslouzil, D. M. and Kant, C. (1998). Operating practices in the beneficiation of major porphyry copper/molybdenum plants from Chile: innovated technology and opportunities, a review. *Minerals Engineering*, *11*(4), 313–331. https://doi.org/10.1016/S0892-6875(98)00011-9.

Chander, S. (1978). Recent Developments in Floatability of Very Fine Particles–Review, Trans. Indian Institute of Metals. Vol. 31, p.21.

Chapman, C.M., Nienow, A.W., Cooke, M. and Middleton, J.C. (1983). Particle-gas-liquid mixing in stirred vessels – Part 2. Chemical engineering research and design, vol. 61, p. 82-95.

Chen, X. and Peng, Y. (2015). The effect of regrind mills on the separation of chalcopyrite from pyrite in cleaner flotation. *Minerals Engineering*, *83*, 33–43. https://doi.org/10.1016/j.mineng.2015.08.008.

Cheng, D., Cheng, J., Li, X., Wang, X., Yang, C. and Mao, Z.-S. (2012). Experimental study on gas-liquid-liquid macro-mixing in a stirred tank. *Chemical Engineering Science*, *75*, 256–266. https://doi.org/10.1016/j.ces.2012.03.035.

Chu, P., Finch, J., Bournival, G., Ata, S., Hamlett, C. and Pugh, R. J. (2019). A review of bubble break-up. *Advances in Colloid and Interface Science*, *270*, 108–122. https://doi.org/10.1016/j.cis.2019.05.010.

Coulson, J. M. and Richardson, J. F. (2019). Coulson and Richardson's chemical engineering (B. Gurappa & R. P. Chhabra, Eds., Sixth, Vol. Volume 2a, particulate systems and particle technology). Butterworth-Heinemann.

Deglon, D. A. (2005). The effect of agitation on the flotation of platinum ores. *Minerals Engineering*, *18*(8), 839–844. https://doi.org/10.1016/j.mineng.2005.01.024.

Deglon, D. A., Egya-mensah, D. and Franzidis, J. P. (2000). Review of hydrodynamics and gas dispersion in flotation cells on south african platinum concentrators. *Minerals Engineering*, *13*(3), 235–244. https://doi.org/10.1016/S0892-6875(00)00003-0.

Finch, J. A. (advisor), Gomez, C. O. (advisor) and Do, S.-S., 1970-. (2003). *Hydrodynamic characterization of a Denver laboratory flotation cell* (dissertation). McGill University.

Drzymala, J. and Lekki, J. (1989). Flotometry—another way of characterizing flotation. *Journal of Colloid and Interface Science*, *130*(1), 205–210. https://doi.org/10.1016/0021-9797(89)90092-1.

Drzymała, J. and Swatek, A. (2007). *Mineral processing: foundations of theory and practice of minerallurgy*. Wrocław. Available at: http://dlib.bg.pwr.wroc.pl/Content/2070 (Accessed: January 15, 2023).

Dunne, R.C., Kawatra, S. K. and Young, C. (eds) (2019) Sme mineral processing and extractive metallurgy handbook. Englewood, Colorado: Society for Mining, Metallurgy and Exploration (SME), p. 2077

Edwards, M. F. and Baker, M. (1992). Mixing of liquids in stirred tanks. In: Mixing in the process industries. Editors: N. Harnby, M. F. Edwards and A. W. Nienow, Butterworth Heinemann, Oxford, p. 137-157.

Eimco Process Equipment Company (1992). Wemco 1+1 mechanical machines. Salt Lake City (WF5-092/BAK 3157).

El-Rahiem, F.H.A. (2014). Recent trends in flotation of fine particles. Journal of Mining World Express, 3, 63–79. doi:10.14355/mwe.2014.03.009.

Encyclopaedia Britannica, https://www.britannica.com/science/fluid-mechanics/Drag, accessed 5 December 2022.

Finch, J.A., Nesset, J.E. and Acuna C. (2008). "Role of frother on bubble production and behavior in flotation," Minerals Engineering, 21, 949-957.

Fogler, H. S. (1999). Elements of chemical reaction engineering. Third edn. Prentice Hall, New York, p. 967.

Fuerstenau, M. C., Jameson, G. J. and Yoon, R. H. (2007). *Froth flotation: a century of innovation*. Littleton, Colo.: Society for Mining, Metallurgy, and Exploration.

Gorain, B. K., Napier-Munn, T. J., Franzidis, J.-P. and Manlapig, E. V. (1998). Studies on impeller type, impeller speed and air flow rate in an industrial scale flotation cell. part 5: validation of k-s b relationship and effect of froth depth. *Minerals Engineering*, *11*(7), 615–626. https://doi.org/10.1016/S0892-6875(98)00046-6.

Gorain, B. K., Franzidis, J.-P. and Manlapig, E. V. (1999). The empirical prediction of bubble surface area flux in mechanical flotation cells from cell design and operating data. *Minerals Engineering*, *12*(3), 309–322. https://doi.org/10.1016/S0892-6875(99)00008-4.

Gorain, B. K., Franzidis, J. P. and Manlapig, E. V. (2000). 'Flotation Cell Design: Application of Fundamental Principles', *Encyclopedia of Separation Science*, 1502–1512. doi: 10.1016/b0-12-226770-2/05781-1.

Gray, J.B. (1967). Flow patterns, fluid velocities and mixing in agitated vessels. In: Uhl, V.W. and Gray, J.B. Mixing, theory and practice. Academic Press, New York, vol.1, p. 179-278.

Greet, C. J. editor (2010). Flotation plant optimisation. First edn. Carlton, Victoria: Australasian Institute of Mining and Metallurgy (Spectrum series, 16).

Gupta, A. and Yan, D. S. (2016). *Mineral processing design and operations: an introduction*. Second edn. Amsterdam: Elsevier.

Harbort, G. and Alexander, D. (2006). 'Gas Dispersion Measurements in Coal Flotation Cells', 254–264.

Harris, C.C. (1976). Flotation machines. In: Fuerstenau, M.C. Flotation: A.M. Gaudin Memorial Volume. AIME, New York, vol. 2, p. 788.

Harris, C.C. (1986). Flotation machines design, scale up and performance: data base. In: Somasundaran, P. (ed), Advances in mineral processing. Symposium honoring Nathaniel Arbiter on his 75th birthday, New Orleans. Littleton, p. 618-635.

Hassanzadeh, A., Safari, M. and Hoang, D. H. (2021). 'Fine, coarse and fine-coarse particle flotation in mineral processing with a particular focus on the technological assessments', p. 9383. doi: 10.3390/iecms2021-09383.

Hay, M. P. and Rule, C. M. (2003). Supasim: a flotation plant design and analysis methodology. *Minerals Engineering*, *16*(11), 1103–1109. https://doi.org/10.1016/j.mineng.2003.06.009.

Holmes, D. B., Voncken, R. M. and Dekker, J. A. (1964). Fluid flow in turbine-stirred, baffled tanks—i: circulation time. *Chemical Engineering Science*, *19*(3), 201–208. https://doi.org/10.1016/0009-2509(64)85030-2.

Horst, W.E. (1952). The effect of impeller speed and air-volume on the flotation rate with respect to particle size.

Joshi, J. B., Pandit, A. B. and Sharma, M. M. (1982). Mechanically agitated gas-liquid reactors. *Chemical Engineering Science*, *37*(6), 813–844. https://doi.org/10.1016/0009-2509(82)80171-1.

Jowett, A. (1980). Formation and disruption of particle–bubble aggregates in flotation. In Fine Particles Processing, Vol. 1. Edited by P. Somasundaran. New York: AIME. 720–754.

Kawatra, S. K. and Young, C. (Eds.). (2019). *Sme mineral processing & extractive metallurgy handbook*. Society for Mining, Metallurgy & Exploration (SME).

Kawatra, S. (2011). Fundamental principles of froth flotation. SME mining engineering handbook. 1517-1532.

Kelly, E. G. and Spottiswood, D. J. (1982). *Introduction to mineral processing*. New York: John Wiley & Sons.

Klimpel, R.R. (1984). Use of chemical reagents in flotation. Chemical Engineering, 91 (18), 75–79.

Larsen, E. and Kleiv, R. A. (2015). 'Towards a New Process for the Flotation of Quartz', *Minerals Engineering*, 83, 13–18. doi: 10.1016/j.mineng.2015.08.004.

Leal Filho, L.S., Rodrigues, W.J. and Ralston, J. (2002). Importance of hydrodynamics in coarse particle flotation. In: Ralston, J., Miller, J., Rubio, J. (eds). Flotation and flocculation: from fundamentals to applications. Snap Printing, Medindie (Australia), p. 203-212.

Liddel, K.S., and Dunne, R C. (1983). An evaluation of the Leeds laboratory-scale flotation cell. Council for Mineral Technology (Mintek) Report No, Randburg, South Africa.

Lima, N. P., Peres, A. E. C. and Gonçalves, T. A. R. (2018). 'Comparative evaluation between mechanical and pneumatic cells for quartz flotation in the Iron ore industry', Revista Escola de Minas, 71(3), 437–442. doi: 10.1590/0370-44672016710179.

Lima, O.A. (2009). Suspension of coarse particles in mechanical flotation cells. Doctoral thesis, University of São Paulo, Polytechnic School, São Paulo-Brazil, p. 230 (text in Portuguese).

Lima, O. A., Deglon, D. A. and Leal Filho, L. S. (2009). 'A Comparison of the Critical Impeller Speed for Solids Suspension in a Bench-Scale and a Pilot-Scale Mechanical Flotation Cell', *Minerals Engineering*, 22(13), 1147–1153. doi: 10.1016/j.mineng.2009.05.002.

Lima, O. A., Marques, C. V. P. and Leal Filho, L. S. (2009). 'Suspension of Apatite Particles in a Self-Aerated Denver Laboratory Flotation Cell', *Mining, Metallurgy & Exploration: An Official International Peer-reviewed Journal of the Society*, 26(2), 74–78. doi: 10.1007/BF03403421.

Liu, A., Fan, J. and Fan, M. (2015). 'Quantum Chemical Calculations and Molecular Dynamics Simulations of Amine Collector Adsorption on Quartz (0 0 1) Surface in the Aqueous Solution', *International Journal of Mineral Processing*, 134, 1–10. doi: 10.1016/j.minpro.2014.11.001.

Ma, Y., Li, S., Zhang, L., Li, H. and Liu, Z. (2020). Numerical simulation on heat extraction performance of enhanced geothermal system under the different well layout. *Energy Exploration & Exploitation*, *38*(1), 274–297. https://doi.org/10.1177/0144598719880350.

Matos, V. E., Nogueira, S. D. C. S., Peres, A. E. C. and Pereira, C. A. (2019). Analysis of quartz floatability using design of experiments. *Rem - International Engineering Journal*, *72*(3), 501–506. https://doi.org/10.1590/0370-44672018720080.

McCabe, W.L., Smith, J.C. and Harriot, P. (1976). *Unit operations of chemical engineering*. 5th edn. New York: McGraw-Hill (McGraw-Hill chemical engineering series), 1130.

Miettinen, T., Ralston, J. and Fornasiero, D. (2010). 'The Limits of Fine Particle Flotation', *Minerals Engineering*, Elsevier Ltd, 23(5), 420–437. doi: 10.1016/j.mineng.2009.12.006.

Nagata, S. (1975). Mixing principles and applications. John Wiley and Sons, New York, 249-295.

Nelson, M. G. and Lelinski, D. (2000). 'Hydrodynamic Design of Self-Aerating Flotation Machines', *Minerals Engineering*, 13(10), 991–998. doi: 10.1016/S0892-6875(00)00085-6. Newcombe, B., Bradshaw, D. and Wightman, E. (2012) 'Development of a Laboratory Method to Predict Plant Flash Flotation Performance', *Minerals Engineering*, 39, 228–238. doi: 10.1016/j.mineng.2012.07.008.

Nguyen, A.V. (2007). Flotation, Encyclopedia of Separation Science, 1–27. https://doi.org/10.1016/B0-12-226770-2/00071-5.

Nienow, A. W. (1997). 'On Impeller Circulation and Mixing Effectiveness in the Turbulent Flow Regime', *Chemical Engineering Science*, 52(15), 2557–2565. doi: 10.1016/S0009-2509(97)00072-9.

Norori-McCormac, A., Brito-Parada, P. R., Hadler, K., Cole, K. and Cilliers, J. J. (2017). The effect of particle size distribution on froth stability in flotation. *Separation and Purification Technology*, *184*, 240–247. https://doi.org/10.1016/j.seppur.2017.04.022.

Nuraje, N., Khan, W. S., Lei, Y., Ceylan, M. and Asmatulu, R. (2013). Superhydrophobic electrospun nanofibers. *Journal of Materials Chemistry A*, *1*(6), 1929–1946. https://doi.org/10.1039/c2ta00189f.

Oldshue, J.Y., Herbst, N.R. and Post, T.A. (1995). *A guide to fluid mixing*, Lightnin, New York.

Pease, J. D., Curry, D. C. and Young, M. F. (2006). 'Designing Flotation Circuits for High Fines Recovery', *Minerals Engineering*, 19(6), 831–840. doi: 10.1016/j.mineng.2005.09.056.

Pease, J. D., Young, M. F., Curry, D. and Johnson, N. W. (2010). Improving fines recovery by grinding finer. *Mineral Processing and Extractive Metallurgy*, *119*(4), 216–222. https://doi.org/10.1179/037195510X12816242170852.

Pretorius, C., Wicklein, E. and Rauch-Williams, T. (2015). 'How Oversized Mixers Became an Industry Standard How Oversized Mixers Became an Industry Standard', (January). doi: 10.2175/193864715819541747.

Rahman, R. M., Ata, S. and Jameson, G. J. (2012). The effect of flotation variables on the recovery of different particle size fractions in the froth and the pulp. *International Journal of Mineral Processing*, *106–109*, 70–77. https://doi.org/10.1016/j.minpro.2012.03.001.

Ramlall, N. V. (2008) Development and modelling of a semi-batch. dissertation.

Rodrigues, O. M. S., Peres, A. E. C., Martins, A. H. and Pereira, C. A. (2013). Kaolinite and hematite flotation separation using etheramine and ammonium quaternary salts. *Minerals Engineering*, *40*, 12–15. https://doi.org/10.1016/j.mineng.2012.09.019.

Rodrigues, W. J., Leal Filho, L. S. and Masini, E. A. (2001). 'Hydrodynamic Dimensionless Parameters and Their Influence on Flotation Performance of Coarse Particles', *Minerals Engineering*, 14(9), 1047–1054. doi: 10.1016/S0892-6875(01)00110-8.

V. Ross (2019). 'Key Aspects of Bench Flotation As a Geometallurgical Characterization Tool', *Journal of the Southern African Institute of Mining and Metallurgy*, 119(4), 361–367. doi: 10.17159/2411-9717/605/2019.

Runge, K. (2010). Laboratory flotation testing - An essential tool for ore characterisation. Flotation Plant Optimisation: A Metallurgical Guide to Identifying and Solving Problems in Flotation Plants. 16. 155-173.

Safari, M., Harris, M., Deglon, D., Filho, L. L. and Testa, F. (2016). The effect of energy input on flotation kinetics. *International Journal of Mineral Processing*, *156*, 108–115. https://doi.org/10.1016/j.minpro.2016.05.008.

Julien Saint Amand, F. (1999). 'Hydrodynamics of Deinking Flotation', *International Journal of Mineral Processing*, 56(1), 277–316. doi: 10.1016/S0301-7516(98)00050-7.

Schubert, H. (1999). 'On the Turbulence-Controlled Microprocesses in Flotation Machines', *International Journal of Mineral Processing*, 56(1), 257–276. doi: 10.1016/S0301-7516(98)00048-9.

Schubert, H. and Bischofberger, C. (1998). 'On the microprocesses air dispersion and particle-bubble attachment in flotation machines as well as consequences for the scale-up of macroprocesses', *International Journal of Mineral Processing*, 52(4), 245–259. doi: 10.1016/S0301-7516(97)00070-7.

Schulze H. J. (1984). *Physico-chemical elementary processes in flotation: an analysis from the point of view of colloid science including process engineering considerations*. Elsevier.

Schwarz, S. and Alexander, D. (2006). 'Gas Dispersion Measurements in Industrial Flotation Cells', *Minerals Engineering*, 19(6), 554–560. doi: 10.1016/j.mineng.2005.09.022.

Shabalala, N. Z. P., Deglon, D. A., Harris, M. and University of Cape Town Centre for Minerals Research. (2013). *Rheological effects on gas dispersion in a pilot scale mechanical flotation cell* (dissertation).

Shabalala, N. Z. P., Harris, M., Leal Filho, L. S. and Deglon, D. A. (2011). Effect of slurry rheology on gas dispersion in a pilot-scale mechanical flotation cell. *Minerals Engineering*, *24*(13), 1448–1453. https://doi.org/10.1016/j.mineng.2011.07.004.

Shergold, H.L. (1984). Flotation in mineral processing. In: Ives, K.J. (eds) The Scientific Basis of Flotation. NATO ASI Series, vol 75. Springer, Dordrecht. https://doi.org/10.1007/978-94-009-6926-1_7.

Souza Pinto, T. C., Braga, A. S., Leal Filho, L. S. and Deglon, D. A. (2018). Analysis of key mixing parameters in industrial wemco mechanical flotation cells. *Minerals Engineering*, *123*, 167–172. https://doi.org/10.1016/j.mineng.2018.03.046.

Tabosa, E., Runge, K., Holtham, P. and Duffy, K. (2016). Improving flotation energy efficiency by optimizing cell hydrodynamics. *Minerals Engineering*, *96–97*, 194–202. https://doi.org/10.1016/j.mineng.2016.05.002.

Tao, D. (2005). 'Role of bubble size in flotation of coarse and fine particles—a review', *Separation Science and Technology*, 39(4), 741–760. doi: 10.1081/SS-120028444.

Tatterson, G. B. (1991). *Fluid mixing and gas dispersion in agitated tanks*. New York: McGraw-Hill.

Trahar, W. J. (1981). 'A rational interpretation of the role of particle size in flotation', *International Journal of Mineral Processing*, 8(4), 289–327. doi: https://doi.org/10.1016/0301-7516(81)90019-3.

Trahar, W. J. and Warren, L. J. (1976). 'The flotability of very fine particles — a review', *International Journal of Mineral Processing*, 3(2), 103–131. doi: 10.1016/0301-7516(76)90029-6.

Uhl, V. W. and Gray, J. B. (1966). *Mixing: theory and practice – vol 1*. New York: Academic Press.

Vera, M. A. (2002). *A touch of froth: how bubble-particle aggregates take the strain; an investigation into aspects of froth zone recovery in mineral flotation*. dissertation.

Vianna, S. M. (2004). the influence of particle size and collector coverage on the floatability of galena particles in a natural ore. dissertation.

Vianna, S. M., Franzidis, J., Manlapig, E., Silvester, E. and Ping-Hao, F. (2003). 'The influence of Particle Size and Collector Coverage on the Floatability of Galena Particles in a Natural Ore', XXII International Mineral Processing Congress, (October), 816–826. doi: 10.13140/RG.2.2.33486.31044.

Wang, D. and Liu, Q. (2021). 'Hydrodynamics of Froth Flotation and Its Effects on Fine and Ultrafine Mineral Particle Flotation: A Literature Review', *Minerals Engineering*, 173. doi: 10.1016/j.mineng.2021.107220.

Wang, L. (2016). Entrainment of fine particles in froth flotation, Thesis: Doctor of Philosophy, University of Queensland, Australia.

Wang, L., Peng, Y., Runge, K. and Bradshaw, D. (2015). A review of entrainment: mechanisms, contributing factors and modelling in flotation. *Minerals Engineering*, *70*, 77–91. https://doi.org/10.1016/j.mineng.2014.09.003

Weedon, D. (2005). Report on site study at CVRD's flotation plant of Taquari-Vassouras. Amira Project P260D, Ian Wark Insitute, Adelaide.

Westhuizen, A. P. P. (2004). The evaluation of solids suspension in a pilot scale mechanical flotation cell. Master dissertation. University of Cape Town, Cape Town, page 25.

Wills, B. A. and Finch, J. A. (2015). *Wills' mineral processing technology: an introduction to the practical aspects of ore treatment and mineral recovery*. Eighth edn. Oxford: Butterworth-Heinemann is an imprint of Elsevier.

Yahorava, V., Kotze, M. and Scheepers, J. (2009). *Comparison of various anion exchange resins for the recovery of uranium by means of rip*. Randburg: Mintek.

Yianatos, J. B., Larenas, J. M., Moys, M. H. and Diaz, F. J. (2008). Short time mixing response in a big flotation cell. *International Journal of Mineral Processing*, *89*(1), 1–8. https://doi.org/10.1016/j.minpro.2008.07.002.

Zheng, X., Johnson, N. W. and Franzidis, J.-P. (2006). 'Modelling of Entrainment in Industrial Flotation Cells: Water Recovery and Degree of Entrainment', *Minerals Engineering*, 19(11), 1191–1203. doi: 10.1016/j.mineng.2005.11.005.

Zlokarnik, M. (1973). Criteria of the Dynamic-Similarity Theory Applied to Dimensioning of Flotation Cells. 26. 107-113.

Zwietering, Th. N. (1958). 'Suspending of Solid Particles in Liquid by Agitators', *Chemical Engineering Science*, 8(3), 244–253. doi: 10.1016/0009-2509(58)85031-9.

Chapter 8: Appendices

Appendix A: Table 14: Flotometric data

(reference for section 1.7)

Strongly hydrophobic*		hydrophobic		weakly hydrophobic		hydrophilic** $\theta = 0$
Material	θ	Material	θ	Material	θ	Material
Paraffin C_nH_{2n+2}	90+	sulfides	44–0	fluorite, CaF_2	10–13	gypsum $CaSO_4 \cdot 2H_2O$
Teflon, C_2F_4	90+	silicon carbide SiC	27.6	arsenic, As_2O_3	9.3	ferrosilicon
Sulfur, S	63.2	coal	26–0	perovskite, $CaTiO_3$	9	dolomite $CaMg(CO_3)_2$
Mercury, Hg	45.6	indium, In	25	scheelite, $CaWO_4$	9	magnetite Fe_3O_4
Germanium, Ge	39.7	iodargyrite, AgI	23.5	diamond, C	7.9	halite, NaCl
Silicon, Si	35.4	cassiterite, SnO_2	22–	tin, Sn	7.5	brawn coal
Talc	35.2	silver, Ag	14	boric acid, H_3BO_3	64	kaolinite
		ilmenite, Fe	14	graphite, C	6.2+	hematite, Fe_2O_3
		molybdenite, MoS_2	5.9+	PbJ_2	6	quartz, SiO_2
				gold, Au	5	calcite, $CaCO_3$
				barite, $BaSO_4$	5	anhydrite, $CaSO_4$
				corundum, Al_2O_3	4	bones
				HgO	3,3	tourmaline
				HgJ_2	3	vegetables
				copper, Cu	3	iron, Fe
						amber
						ice, D_2O

* Flotometric method is able to measure contact angles smaller than 90°.
** Other hydrophilic materials: chromite, malachite, smithsonite, azurite, rutile, zircon, mica.

Appendix B: Empirical data

Equivalent Froude number calculation – Section 3.5.1

$$N_{Fr}(Denver) = \frac{N^2 D}{g}$$

$$N = \sqrt{\frac{N_{Fr} * g_a}{D}}$$

$$N = \sqrt{\frac{2.88 * 9.81}{70.4x10^{-3}}} = 20\ s^{-1} = 1200\ rpm$$

Kinetic Tests results - Calibration Tests

Table 15: Denver 1200 rpm data to support **Figure 31 & 32**

Time	Stream ID	Mass	Mass dist.	Cum. Rec Test 1	Test 2 Cum Rec	Average Rec	STDev
min		g	%	%	%	%	
1	Con 1	186.8	32.5	32.5	39.3	**35.9**	4.85
3	Con 2	234.3	40.7	73.2	75.9	**74.6**	1.90
5	Con 3	109.4	19.0	92.3	92.6	**92.4**	0.23
	Tail	41.2					
	Feed	575.0					

Table 16: Leeds 1175 rpm data to support **Figure 31 & 32**

Time	Stream ID	Mass	Mass dist.	Cum. Rec Test 1	Test 2 Cum Rec	Average Rec	STDev
min		g	%	%	%	%	
1	Con 1	106.8	18.6	18.6	25.5	**22.0**	4.90
3	Con 2	248.1	43.1	61.7	65.6	**63.7**	2.77
6	Con 3	181.8	31.6	93.3	90.4	**91.9**	2.09
	Tail	33.6					
	Feed	575.0					

Table 17: Leeds 1400 rpm data to support **Figure 32**

Time	Stream ID	Mass	Mass dist.	Cum. Rec Test 1	Test 2 Cum Rec	Average Rec	STDev
min		G	%	%	%	%	
1	Con 1	213.4	37.1	37.1	35.2	**36.2**	1.36
3	Con 2	210.5	36.6	73.7	72.3	**73.0**	0.97
5.5	Con 3	108.3	18.8	92.6	91.1	**91.8**	1.02
	Tail	39.7					
	Feed	575.0					

Table 18: Leeds 1800 rpm data to support **Figure 32**

Time	Stream ID	Mass	Mass dist.	Cum. Rec Test 1	Test 2 Cum Rec	Average Rec	STDev
min		g	%	%	%	%	
1	Con 1	314.1	54.6	54.6	54.9	**54.8**	0.23
3	Con 2	170.6	29.7	84.3	86.2	**85.3**	1.36
4.2	Con 3	55.8	9.7	94.0	92.3	**93.1**	1.21
	Tail	30.1					
	Feed	575.0					

Air flow rate – Section 4.4 to support **Figure 33**

Table 19: Displacement J_g data

RPM	Denver 1200	Leeds 1200	Leeds 1400
	0.14	0.14	0.21
	0.15	0.13	0.21
	0.24	0.17	0.20
	0.25	0.21	0.20
	0.25	0.21	0.26
	0.25	0.32	0.26
	0.26	0.32	0.15
	0.24	0.28	0.15
	0.24	0.29	0.30
	0.19	0.17	0.30
	0.18	0.17	
Average J_g	**0.22**	**0.21**	**0.22**
STDev	0.04	0.07	0.05

Particle size effect Section 4.5

Table 20: Kinetic data -Denver - Fines_ 0 – 25 µm to support **Figure 35 and Table 9**

Time	Stream ID	Mass	Mass dist.	Cum. Rec Test 1	Test 2 Cum Rec	Average Rec	STDev	Rmax	21.24
								k	0.32
min		g	%	%	%	%		Rc (%)	
1	Con 1	26.5	4.6	4.6	6.6	5.6	1.42	5.84	
2	Con 2	19.4	3.4	8.0	12.5	10.2	3.21	10.07	
3	Con 3	11.8	2.1	10.0	16.3	13.2	4.46	13.14	
4	Con 4	10.1	1.8	11.8	18.8	15.3	4.97	15.36	
	Tail	508.5							
	Feed.	575.2							

Table 21: Kinetic data -Leeds - Fines_ 0 – 25 µm to support **Figure 35 and Table 9**

Time	Stream ID	Mass	Mass dist.	Cum. Rec Test 1	Test 2 Cum Rec	Average Rec	STDev	Rmax	23.32
								k	0.18
min		g	%	%	%	%		Rc (%)	
1	Con 1	18.9	3.3	3.3	4.1	3.7	0.60	3.78	
2	Con 2	16.3	2.8	6.1	8.1	7.1	1.44	6.95	
3	Con 3	10.2	1.8	7.9	11.0	9.4	2.21	9.61	
4	Con 4	15.7	2.7	10.6	13.2	11.9	1.82	11.83	
	Tail	509.8							
	Feed	575.8							

Table 22: Kinetic data -Denver - Intermediate_ +25 – 45 µm to support **Figure 35 and Table 9**

Time	Stream ID	Mass	Mass dist.	Cum. Rec Test 1	Test 2 Cum Rec	Average Rec	STDev	Rmax	92.17
								k	0.65
min		g	%	%	%	%		Rc (%)	
1	Con 1	233.4	40.6	40.6	40.5	40.6	0.05	44.03	
2	Con 2	174.6	30.4	71.0	71.4	71.2	0.31	67.03	
3	Con 3	49.0	8.5	79.5	78.4	79.0	0.76	79.04	
4	Con 4	25.1	4.4	83.9	84.0	83.9	0.10	85.31	
	Tail	89.6							
	Feed.	575.0							

Table 23: Kinetic data -Leeds - Intermediate_ +25 – 45 µm to support **Figure 35**

Time	Stream ID	Mass	Mass dist.	Cum. Rec Test 1	Test 2 Cum Rec	Average Rec	STDev	Rmax	94.67
								k	0.44
min		g	%	%	%	%		Rc (%)	
1	Con 1	187.2	32.5	32.5	30.7	31.6	1.29	33.53	
2	Con 2	151.7	26.4	58.9	55.4	57.1	2.43	55.19	
3	Con 3	75.0	13.0	71.9	66.4	69.2	3.88	69.17	
4	Con 4	39.5	6.9	78.8	76.6	77.7	1.55	78.20	
	Tail	117.1							
	Feed.	575.8							

Table 24: Kinetic data -Denver - Medium_ +45 – 75 µm to support **Figure 34 and Table 9**

Time	Stream ID	Mass	Mass dist.	Cum. Rec Test 1	Test 2 Cum Rec	Average	STDev	Rmax	95.67
								k	0.70
min		g	%	%	%	%			
1	Con 1	284.8	49.5	49.5	48.6	49.1	0.63	48.03	
2	Con 2	106.9	18.6	68.1	70.9	69.5	2.00	71.94	
2.5	Con 3	64.0	11.1	79.2	81.9	80.5	1.87	78.93	
	Tail	116.9							
	Feed	575.29							

Table 25: Kinetic data -Leeds - Medium_ +45 – 75 µm to support **Figure 34**

Time	Stream ID	Mass	Mass dist.	Cum. Rec Test 1	Test 2 Cum Rec	Average Rec	STDev	Rmax	100.00
								k	0.63
min		g	%	%	%	%		Rc (%)	
1	Con 1	272.6	47.4	47.4	44.1	45.7	2.34	46.57	
2	Con 2	142.1	24.7	72.1	69.9	71.0	1.55	71.46	
2.5	Con 3	57.2	9.9	82.0	79.1	80.6	2.04	79.14	
	Tail	100							
	Feed	575.38							

Table 26: Kinetic data -Denver - Coarse_ +75 – 106 µm to support **Figure 34 and Table 9**

Time	Stream ID	Mass	Mass dist.	Cum. Rec Test 1	Test 2 Cum Rec	Average Rec	STDev	Rmax	100.00
								k	0.53
min		g	%	%	%	%		Rc (%)	
1	Con 1	195.3	34.0	34.0	36.3	35.1	1.64	41.19	
2	Con 2	190.7	33.2	67.1	64.1	65.6	2.14	65.42	
2.5	Con 3	63.3	11.0	78.1	79.3	78.7	0.83	73.48	
	Tail	123.9							
	Feed	575.29							

Table 27: Kinetic data -Leeds - Coarse_ +75 – 106 µm to support **Figure 34**

Time	Stream ID	Mass	Mass dist.	Cum. Rec Test 1	Test 2 Cum Rec	Average Rec	STDev	Rmax	100.00
								k	0.49
min		g	%	%	%	%		Rc (%)	
1	Con 1	193.8	33.7	33.7	36.4	35.0	1.91	38.81	
2	Con 2	163.4	28.4	62.1	64.0	63.1	1.37	62.56	
2.5	Con 3	64.9	11.3	73.4	73.4	73.4	0.02	70.71	
	Tail	149.4							
	Feed	575.38							

Table 28: Kinetic data -Denver -25 µm (50 g/t dosage) to support **Figure 36**

Time	Stream ID	Mass	Mass dist.	Cum. Rec Test 1	Test 2 Cum Rec	Average Rec	STDev	Rmax	55.82
								k	0.35
min		g	%	%	%	%		Rc (%)	
1	Con 1	80.0	13.9	13.9	14.6	14.2	0.45	16.30	
2	Con 2	76.2	13.3	27.2	28.3	27.7	0.79	27.84	
3	Con 3	52.9	9.2	36.4	37.7	37.0	0.94	36.01	
4	Con 4	32.0	5.6	41.9	43.4	42.6	1.00	41.80	
5	Con 5	19.7	3.4	45.4	46.9	46.1	1.11	45.89	
6	Con 6	14.1	2.5	47.8	49.2	48.5	0.97	48.79	
7.5	Con 7	14.4	2.5	50.3	51.7	51.0	0.99	51.63	
	Tail	280.0							
	Feed	574.9							

Table 29: Kinetic data -Leeds -25 µm (50 g/t dosage) to support **Figure 36**

Time	Stream ID	Mass	Mass dist.	Cum. Rec Test 1	Test 2 Cum Rec	Average Rec	STDev	Rmax	56.37
								k	0.27
min		g	%	%	%	%		Rc (%)	
1	Con 1	71.1	12.3	12.3	11.4	11.9	0.64	13.53	
2	Con 2	69.2	12.0	24.4	23.0	23.7	1.00	23.81	
3	Con 3	49.0	8.5	32.9	31.7	32.3	0.81	31.62	
4	Con 4	36.8	6.4	39.3	37.4	38.3	1.33	37.56	
5	Con 5	23.2	4.0	43.3	41.1	42.2	1.57	42.08	
6	Con 6	17.7	3.1	46.4	44.2	45.3	1.50	45.51	
7.5	Con 7	21.0	3.6	50.0	47.6	48.8	1.70	49.17	
	Tail	281.2							
	Feed	575.8							

Table 30: Kinetic data -Denver -25 µm (175 g/t dosage) to support **Figure 36**

Time	Stream ID	Mass	Mass dist.	Cum. Rec Test 1	Test 2 Cum Rec	Average Rec	STDev	Rmax	94.58
								k	0.34
min		g	%	%	%	%		Rc (%)	
1	Con 1	126.8	22.0	22.0	19.3	20.7	1.90	27.59	
2	Con 2	146.1	25.4	47.4	43.2	45.3	3.03	47.13	
3	Con 3	103.0	17.9	65.3	62.2	63.8	2.20	60.97	
4	Con 4	56.7	9.9	75.2	73.5	74.3	1.21	70.78	
5	Con 5	26.5	4.6	79.8	79.6	79.7	0.13	77.72	
6	Con 6	13.7	2.4	82.2	82.5	82.4	0.26	82.64	
8.5	Con 7	22.6	3.9	86.1	86.8	86.4	0.47	89.54	
	Tail	75.0							
	Feed	575.2							

Table 31: Kinetic data -Leeds -25 µm (175 g/t dosage) to support **Figure 36**

Time	Stream ID	Mass	Mass dist.	Cum. Rec Test 1	Test 2 Cum Rec	Average Rec	STDev	Rmax	96.30
								k	0.23
min		g	%	%	%	%		Rc (%)	
1	Con 1	76.5	13.3	13.3	13.4	13.4	0.09	19.77	
2	Con 2	117.1	20.4	33.7	31.2	32.4	1.74	35.47	
3	Con 3	99.8	17.3	51.0	46.3	48.6	3.36	47.96	
4	Con 4	75.5	13.1	64.1	57.8	61.0	4.49	57.88	
5	Con 5	44.4	7.7	71.9	65.8	68.8	4.31	65.77	
6	Con 6	23.6	4.1	76.0	70.3	73.1	4.02	72.03	
9	Con 7	44.3	7.7	83.6	78.6	81.1	3.58	84.12	
	Tail	88.7							
	Feed	575.1							

Appendix C: Hydrodynamics

Power and Reynolds numbers - Section 4.8.1

Table 32: Dimensionless numbers tested in the Denver with water and slurry- to support **Figure 39 and 40**

Water only test

Hertz	16.7	18.3	20.0	21.7	23.3	25.0
RPM	1000	1100	1200	1300	1400	1500
Consumed	11.0	12.0	15.0	17.0	19.0	23.0
Np	**1.37**	**1.13**	**1.08**	**0.97**	**0.86**	**0.85**
Re	**97077**	**106785**	**116492**	**126200**	**135908**	**145615**
Fr	1.99	2.41	2.87	3.37	3.91	4.49

With solids Dynamic viscosity. η (Pa.s) = 0.00102

Hertz	16.7	18.3	20.0	21.7	23.3	25.0
RPM	1000	1100	1200	1300	1400	1500
Consumed	7.0	9.0	12.0	15.0	19.0	23.0
Np	**0.78**	**0.76**	**0.78**	**0.76**	**0.78**	**0.76**
Re	**89992**	**98992**	**107991**	**116990**	**125989**	**134989**
Fr	1.99	2.41	2.87	3.37	3.91	4.49

Table 33: Dimensionless numbers tested in the Leeds with water and slurry to support **Figure 39 and 40**

Water only test

Hertz	16.67	18.33	20	21.67	23.33	25
RPM	1000	1100	1200	1300	1400	1500
Consumed	11.0	17.0	20.0	25.0	27.0	32.0
Np	**1.09**	**1.26**	**1.14**	**1.12**	**0.97**	**0.94**
Re	**106643**	**117263**	**127947**	**138630**	**149250**	**159933**
Fr	2.09	2.53	3.01	3.53	4.09	4.70

With solids Dynamic viscosity. η (Pa.s) = 0.00102

Hertz	16.7	18.3	20.0	21.7	23.3	25.0
RPM	1000	1100	1200	1300	1400	1500
Consumed	11.0	18.0	21.0	26.0	30.0	35.0
Np	**0.97**	**1.20**	**1.08**	**1.05**	**0.97**	**0.92**
Re	**98841**	**108725**	**118609**	**128493**	**138378**	**148262**
Fr	2.09	2.53	3.01	3.53	4.09	4.70

Section 4.8.2

Table 34: Chemical tracer data in ungassed system –to support **Table 10 and 11**

No Air	Denver				Leeds		
Speed (rpm)	1000	1200	1400		1000	1200	1400
time (s) to reach pH 11	13.69	18.16	17.79		14.27	12.1	14.13
	17.97	14.89	15.57		14.28	11.57	15.23
	16.03	16.39	12.47		12.58	13.87	12.57
	18.09	13.24	15.49		10.59	13.47	15.5
	17.09	14.27	16.44		11.23	13.78	
	16.31	14.36	15.44				
Average	**16.18**	**15.61**	**15.48**		**12.59**	**12.96**	**14.36**
Std	1.75	1.93	1.60		1.70	1.05	1.33

Table 35: Chemical tracer data in agassed system –to support **Table 10 and 11**

2 L/MIN	Denver				Leeds		
Speed (rpm)	1000	1200	1400		1000	1200	1400
time (s) to reach pH 11	13.37	12.17	9.04		10.32	12.43	10.79
	13.29	10.23	11.59		10.52	12.59	11.07
	9.27	14.57	11.33		10.97	12.97	11.79
	10.99	12.97	12.3		13.53	12.59	11.96
	10.79	14.45	14.33		12.79	12.15	11.72
	11.38	12.87	12.19		11.81	10.93	12.43
Average	**11.52**	**12.88**	**11.80**		**11.66**	**12.28**	**11.63**
Std	1.58	1.60	1.71		1.29	0.71	0.60

Table 36: Cell volume and impeller dimensions

Volume (fluid)m3	0.003	
	Denver	Leeds
Diameter (m)	0.0704	0.0738

Table 37: Flow rate discharged by the impeller to support **Table 12** using data from Table 31 and 32

Calculation: Flow rate = $\frac{0.003}{11.52} = 0.0156$

Q (m3/s) (x 10^-3)	Denver				Leeds		
Speed	16.7	20	23.3		16.7	20	23.3
No Air	0.19	0.19	0.19		0.238	0.232	0.209
2 L/Min	0.26	0.23	0.25		0.257	0.244	0.258

Table 38: Pumping number to support **Figure 41** using data from Tables 31 and 32

Calculation: Nq = (0.00026)/(0.0704^3*16.7) = 0.045

Nq	Denver				Leeds		
Speed	1000 rpm (16.7)	1200 rpm (20)	1400 rpm (23.3)		1000 rpm (16.7)	1200 rpm (20)	1400 rpm (23.3)
No Air	0.032	0.028	0.024		0.036	0.029	0.022
2 L/Min	**0.045**	**0.033**	**0.031**		**0.038**	**0.035**	**0.028**